Mariell Breivik

Simulating pure odd-frequency Josephson Junctions with conventional superconductors

Master's thesis in Physics
Supervisor: Sol H. Jacobsen
Co-supervisor: Jacob Linder

April 2022

Master's thesis

NTNU
Norwegian University of
Science and Technology

Mariell Breivik

Simulating pure odd-frequency Josephson Junctions with conventional superconductors

Master's thesis in Physics
Supervisor: Sol H. Jacobsen
Co-supervisor: Jacob Linder
April 2022

Norwegian University of Science and Technology
Faculty of Natural Sciences
Department of Physics

NTNU
Norwegian University of
Science and Technology

ABSTRACT

We consider the proximity effect in superconducting heterostructures with intrinsic Rashba SO-coupling in equilibrium. We first consider the one-dimensional S/F/S-Josephson junction with SO-coupling investigated by Jacobsen and Linder [1], before connecting two such systems with a nanowire forming an H-geometry. This allows us to simulate an effective odd-frequency Josephson junction, just by the use of s-wave superconductors. The goal of this thesis is to theoretically and numerically investigate how the proximity effect manifests in the density of states in such a geometry. In particular, we explore how the giant triplet effect seen in the two parallel S/F/S-Josephson junctions presents itself in the nanowire.

The analytical equations describing our systems are obtained from the quasiclassical theory of superconductivity, with the spin-orbit field incorporated as an SU(2) gauge field. We parameterize these equations in the so-called Riccati-parameterization, well suited for numerical simulations. We present an analytical discussion of the weak proximity limit and a numerical investigation of the full proximity regime for our systems. Our results show that the effective Josephson junction behaves qualitatively different from the one-dimensional Josephson junction. We show that this counter intuitive result is due to the relationships between the initial symmetries at the midpoints of the parallel junctions, and that this characteristic behaviour is therefore only marginally affected by an exchange field or spin-orbit coupling in the central wire. Remarkably, our results also show that the zero-energy peak in the density of states now can persist throughout the junction for several superconducting coherence lengths.

SAMMENDRAG

Vi undersøker proksimitetseffekten i superledende hybridsystemer med iboende Rashba spinn-bane-kobling i likevekt. Motivert av Josephson-effekten i en 1-dimensional S/F/S-struktur med spinn-bane-kobling, først undersøkt av av Jacobsen and Linder [1], kobler vi sammen to slike systemer med en perpendikulær nanotråd. Systemet vårt danner nå en H-geometri. Vi kan med dette simulere et effekitvt odd-frekvens hybrid system kun ved hjelp av koventionelle superledere. I denne avhandlingen gransker vi teoretisk og numerisk tilstandstettheten for et slikt system, med et spesielt fokus på hvordan Josephson-effekten sett i de to parallele S/F/S-systemene utspiller seg i den sentrale nanotråden.

Det tas utgangspunkt i kvasiklassisk teori for superledning, med spinn-bane-feltet inkludert som et SU(2)-gaugefelt. For numeriske beregninger introduserer vi Riccati-parameteriseringen. Vi presenterer en analytisk diskusjon av grensetilfellet hvor materialene i hybridsystemet påvirker hverandre svakt, samt en numerisk gransking av det fulle regimet. Resulatene viser at det effektive hybridsystemet ikke oppfører seg kvalitativt likt som den 1-dimensionale S/F/S-strukturen med spinn-bane-kobling. Vi viser at dette kontraintuitive resultatet er en følge av symmetrirelasjoner mellom de komponentene opprinnelig tilstede, og at denne karaktersitske oppførselen kun marginalt blir påvirket av et utvekslingsfelt eller spin-bane-felt. Resultatene viser også at tilstandstettheten ved energi lik null kan vedvare gjennom den sentrale ledningen for flere superledende koherenslengder.

PREFACE

This thesis was submitted as the conclusion of a two-year Master's degree program in physics at Norwegian University of Science and Technology (NTNU). The thesis amounts for 60 ECTS-credits, with Dr. Sol H.Jacobsen as supervisor and Prof. Jacob Linder as co-supervisor at the Center for Quantum Spintronics (QuSpin).

First I would like to thank my supervisor Dr. Sol H.Jacobsen for her support and presence throughout my degree. Our weekly meetings filled with helpful discussions have been of great importance to me. I will also thank my co-supervisor Prof Jacob Linder for helpful discussions over the past years. In addition, I will also thank the members of QuSpin for creating an including environment for the Master students as well. Finally, I want to thank the people closest to me for their support during my degree.

Throughout this thesis, we will denote scalars and complex numbers by the font face a. We also use the standard notation $z = a + i \cdot b$, where z and b are scalars and i is the imaginary unit. The complex conjugate of z is denoted by z^*.

Furthermore, vectors in three-dimensional space will be denoted as $\mathbf{v}$. The Cartesian unit vector will be denoted as $\mathbf{e}_x, \mathbf{e}_y$ and $\mathbf{e}_z$, without the conventional hat. With the short-hand notation, the nabla operator therefore becomes $\nabla = \partial_x \mathbf{e}_x + \partial_y \mathbf{e}_y + \partial_z \mathbf{e}_z$.

We write the transpose of a matrix as A^T and the Hermittian conjugate as $\mathrm{A}^\dagger$. Next, we denote the commutator by $[\mathrm{A}, \mathrm{B}]_- = \mathrm{AB} - \mathrm{BA}$ and the anti-commutator by $[\mathrm{A}, \mathrm{B}]_+ = \mathrm{AB} + \mathrm{BA}$. When dealing with 2×2 complex matrices in Nambu-space, we will use the notation $\hat{\mathrm{A}}$. For similar matrices in spin space, we use the notation $\underline{\mathrm{A}}$. We use the standard Pauli matrices $\underline{\sigma}^0$, $\underline{\sigma}^1$, $\underline{\sigma}^2$ and $\underline{\sigma}^3$ as the basis vector for spin space

$$\underline{\sigma}^0 = \begin{pmatrix} 1 & 0 \\ 0 & 1 \end{pmatrix}, \qquad \underline{\sigma}^1 = \begin{pmatrix} 0 & 1 \\ 1 & 0 \end{pmatrix}, \qquad \underline{\sigma}^2 = \begin{pmatrix} 0 & -i \\ i & 0 \end{pmatrix}, \qquad \underline{\sigma}^3 = \begin{pmatrix} 1 & 0 \\ 0 & -1 \end{pmatrix}. \tag{1}$$

Thereby defining the Pauli vector as $\sigma = \underline{\sigma}^1 \mathbf{e}_x + \underline{\sigma}^2 \mathbf{e}_y + \underline{\sigma}^3 \mathbf{e}_z$. The basis matrices in Nambu-space are defined in the same manner as the Pauli matrices in spin space, though denoted by τ's instead of $\underline{\sigma}$'s.

Furthermore, the following 4×4-matrices will also be convenient

$$\hat{\rho}^1 = \begin{pmatrix} 0 & 0 & 0 & 1 \\ 0 & 0 & 1 & 0 \\ 0 & 1 & 0 & 0 \\ 1 & 0 & 0 & 0 \end{pmatrix}, \qquad \hat{\rho}^2 = \begin{pmatrix} 0 & 0 & 0 & -i \\ 0 & 0 & -i & 0 \\ 0 & i & 0 & 0 \\ i & 0 & 0 & 0 \end{pmatrix}, \qquad \hat{\rho}^3 = \begin{pmatrix} 1 & 0 & 0 & 0 \\ 0 & 1 & 0 & 0 \\ 0 & 0 & -1 & 0 \\ 0 & 0 & 0 & -1 \end{pmatrix}. \tag{2}$$

Finally, we denote the Heaviside step-function as $\theta(t)$, while $\delta(t)$ denotes the Kronecker delta. The Kronecker product $\otimes$ will also be useful. For instance $\hat{\rho}^3$ can be expressed by the Kronecker product $\hat{\rho}^3 = \tau^3 \otimes \sigma^0$. Additionally, if not specified otherwise, $\mathbf{p}$ always denotes the momentum, m always denotes the mass of an electron and e always denotes the charge of an electron.

In this thesis, we will also use the rationalized natural units convention, that is we normalize the Planck's constant $\hbar$, the Boltzamnn's constant k and the gravitational constant G to unity

$$\hbar = k = 4 = c = 1, \tag{3}$$

where ϵ_0 and μ_0 denote the vacuum permittivity and permeability respectively. Furthermore, since $c = 1/\sqrt{\epsilon_0 \mu_0}$, these constants can also be set to unity $\epsilon_0 = \mu_0 = 1$.

CONTENTS

INTRODUCTION

1.1 BACKGROUND AND MOTIVATION

In 1911, Onnes and his staff discovered that mercury lost electrical resistivity below a critical temperature T_c just a few degrees over zero Kelvin [2, 3]. At the time, the fundamental theory to describe this was not known, so little did he know that he had witnessed the birth of superconductivity. In the years to come, many experiments were done trying to describe and explore this exotic new phenomenon. One such experiment was conducted by Meissner in 1933 [4]. In this experiment, Meissner cooled down superconducting materials while applying an external magnetic field. When the temperature was below the critical temperature, he discovered that the magnetic field inside the sample was (nearly totally) cancelled. This exclusion of the magnetic field inside a superconducting material below the critical temperature is referred to as the Meissner effect and is the second property defining a superconductor. The Meissner effect divides superconductors into two types, conventional low-temperature superconductors and unconventional high-temperature superconductors. In this thesis, we will focus on the conventional low-temperature superconductors [1].

Resistance in conductors can originate from several sources, mainly electron-phonon scattering, electron-impurity scattering and electron-electron scattering. In the case of a conventional superconductor at low temperature, the electron-phonon scattering contributes the most to the resistance. As stated, one of the properties of superconductors are the loss of resistance below a critical temperature, so how does this relate to electron-phonon scattering? The answer lies within the theoretical description of conventional superconductors, namely the BCS-theory [8], which we will now give a brief introduction to. Imagine a system consisting of positively charged ions in a lattice structure below the critical temperature. If an electron now moves through, it will attract the positively charged ion cores. However, since the mass of the ion cores are much larger than the electron, the position of the ion cores will remain shifted for some time after the electron has moved away. Hence, the presence of an electron causes a slight shift in the local charge distribution, as sketched in figure 1. If now a second electron comes by, it will experience a positive charge as a result of this shift in the local charge distribution. Therefore, the second electron, sketched as the leftmost electron in figure 1, now experiences an attractive Coulomb force. Since this shift of the local charge distribution is caused by another electron, we say that the two electrons now have an attractive interaction, forming what we call a Cooper-pair. Consisting of two electrons, this Cooper-pair effectively has an integer value of spin. Therefore, the Cooper-pair behaves like bosons [2], making it possible to get Bose-Einstein-condensation. In other words, what actually happens is that electrons below this critical temperature start to pair up in Cooper-pairs, and since Cooper-pairs behave like bosons, the Pauli exclusion principle does not prevent several Cooper-pairs to be in the ground state. One can also show that the formation of Cooper-pairs actually protects the electrons from scattering, due to the

---

[1] Typically conventional superconductors have low critical temperatures. In recent years though, one has managed to drastically increase the critical temperature for conventional superconductors, at the cost of very high pressures [5, 6, 7].

[2] Cooper-pairs are not actually bosons, but since the commutation-relations to leading order are bosonic, Cooper-pairs qualitatively behave as bosons.

creation of an energy gap in the energy band structure. Hence, below a critical temperature, this electron-phonon scattering just vanishes. This was indeed the phenomenon Onnes first discovered back in 1911.
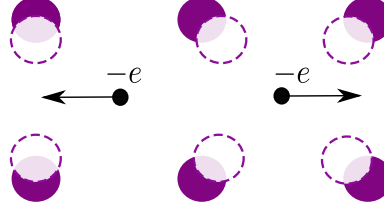

Figure 1: A illustration of the effective attractive interaction between electrons due to lattice distortions. The rightmost electron travels through the lattice, leaving behind a distorted lattice. The leftmost electron is then attracted by the distorted lattice.

However, according to the BCS-theory, the critical temperature may seem a bit mysterious. What makes the system suddenly behave so drastically different at this critical temperature? It turns out that this critical temperature has quite a simple physical interpretation. A crucial point in the explanation above is that the second electron comes by when the local charge distribution is still shifted. Hence, there is a maximum amount of time the second electron can wait before coming, to still experience an attractive force. If it waits too long or the lattice vibrates too fast, the positively charged ion will relax to the initial position, meaning that we no longer have a shifted local charge distribution. At the same time, the second electron cannot come too fast either, since the repulsive Coulomb force between the electrons then would win over the attractive force from the shifted charge distribution. The loss of resistivity is therefore a delicate balance between competing forces, and the critical temperature corresponds to the highest temperature in which the outcome of this competition is an attractive force. If we are above the critical temperature, the lattice vibration will destroy the attractive interaction.

We now move on to the second property of superconductors, the Meissner effect. Mathematically, the Meissner effect is described by the London equation, derived by H.London and F.London [9]. The London equation is motivated by assuming that in a superconducting material the current density is proportional to the vector field $\mathbf{A}$ of a local magnetic field, i.e. $\mathbf{j} = C\mathbf{A}$ where C is a constant. This assumption is quite different from what we will have in a normal conductor, where the current density is described by Omh's law, i.e. $\mathbf{j} = \sigma\mathbf{E}$. What the London brothers did was to show that a superconductor could be well described by choosing $C = -1/\mu_0\lambda_L^2$, where μ_0 is the vacuum permeability and λ_L is a constant with dimension length [9]. Combining this with the Maxwell equations we get the so-called London equation

$$\nabla^2\mathbf{B} = \mathbf{B}/\lambda_L^2. \tag{4}$$

Suppose that we have a semi-infinite superconductor in the superconducting state. Solving the London equation it is straightforward to show that the external magnetic field $\mathbf{B}$ decays exponentially over the characteristic length scale λ_L, as shown in figure 2a. This characteristic length scale is called the London penetration depth and its value is typically in the range of tens of nanometers [10, 11]. In other words, the magnetic field can only survive in a thin layer

close to the surface, whereas it completely vanishes for most of the sample. This is exactly the effect Meissner measured.

However, the exclusion of a magnetic field does cost energy, so it is reasonable to think that at some point a strong magnetic field can destroy the superconductivity. This is indeed the case, and the strongest magnetic field one can apply before breaking the superconductivity at zero temperature is called the critical magnetic field H_0. At increasing temperatures, it is reasonable to expect the value of H_0 to decrease, since increasing the temperature makes the Cooper-pairs easier to destroy. Following the work of the London brothers, Landau and Ginzburg showed that this indeed holds [11, 12]. They found that the critical magnetic field H_c is proportional to $H_0(1 - (T/Tc)^2)$, where T_c is the critical temperature as shown in figure 2b [11, 12]. The region in which the temperature is below the critical temperature and the field is below the critical field is referred to as the superconducting phase, while the region in which the superconductivity is destroyed is referred to as the normal phase.
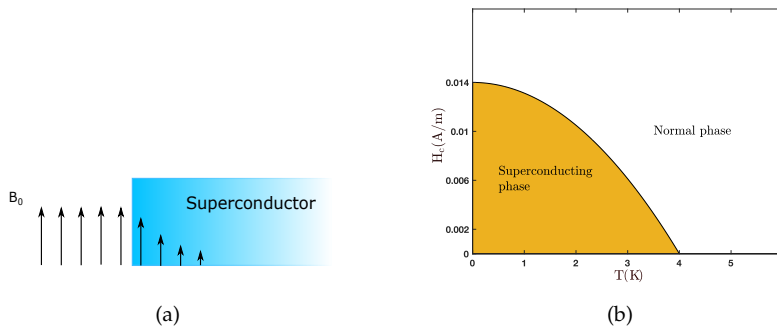

Figure 2: Properties of type I superconductors. The magnetic field as a function of position is illustrated in (a), while the temperature dependence of the critical magnetic field with $H_0 = 0.014$ A/m and $T_c = 4$ K is plotted in (b).

At first sight, the Meissner effect may seem to violate Ampere's law. After all, a moving charge surely should give rise to a magnetic field, but in the superconductor we have no magnetic field while still having a current. The explanation lies in the London penetration depth. Recall that the London equation does not predict that the external magnetic field drops to zero immediately after entering the superconductor, it rather falls exponentially. Of course, the magnetic field will not survive long, but we still have a thin layer in which the magnetic field is nonzero. If the current flows in this thin layer, Ampere's law still holds and this is indeed what happens. The superconducting current only flows in a thin layer close to the surface, and hence the Meissner effect does not violate Ampere's law.

We now move on to the field of spintronics. In short, spintronics is the utilization of the spin of the electron in addition to its charge [13]. For example, if spin up is represented as 1 and spin down as 0, we can use the qubits for a wide variety of applications, such as quantum communication, computing and sensors as well as quantum dots [14]. Another example is spin-transfer torque, in which a spin-polarized current is used to change the orientation of the magnetization in a magnetic material [15]. However, we do not necessarily need to have an electric current to transport spin. Magnetic insulators are good examples of this, where a continuous change in the orientation of the electronic spin gives rise to a spin wave [16]. Thus, the spin is transported as a wave rather than by moving electrons. Finally, topological insulators

also have received a lot of research due to their interesting properties [17]. These materials have a gap in the bulk band structure like ordinary insulators, yet the spin-orbit coupling combined with time-reversal symmetry creates gapless surface or edge states, allowing for ultra-low dissipation transport of charge and spin at the surface or edge.

The field of superconducting spintronics is the merging of superconductivity and spintronics [18]. As the name implies, superconducting spintronics inherits both the properties of superconductivity and the properties of spintronics, leading to intriguing new phenomena. One of these phenomena is the generation of triplet states. Imagine that we have a convectional superconductor in contact with a magnetic metal, let us say a ferromagnet. Near the interface, the properties of the superconductor will leak into the ferromagnet and vice versa, known as the proximity effect. In a conventional bulk superconductor the Cooper-pair prefers the zero center of mass momentum singlet state $(\uparrow\downarrow - \downarrow\uparrow)$. However, when the Cooper-pairs enter the ferromagnet, the situation becomes different. As we soon will discuss in more detail, the energy bands for spin-up and spin-down get shifted in the presence of an exchange field. This shifting of the energy bands causes the momentum at the Fermi-energy to shift slightly, resulting in a Cooper-pair with a nonzero center of mass momentum $\pm\mathbf{Q}$. The singlet state therefore transforms according to $(\uparrow\downarrow - \downarrow\uparrow) \rightarrow (\uparrow\downarrow\, e^{i\mathbf{Q}\cdot\mathbf{R}} - \downarrow\uparrow\, e^{-i\mathbf{Q}\cdot\mathbf{R}}) = (\uparrow\downarrow - \downarrow\uparrow)\cos(\mathbf{Q}\cdot\mathbf{R}) + i(\uparrow\downarrow + \downarrow\uparrow)\sin(\mathbf{Q}\cdot\mathbf{R})$, where $\mathbf{R}$ is the center-off-mass position [19]. In other words, the Cooper-pairs change from being in a singlet state to a mixture of the singlet and triplet state $(\uparrow\downarrow + \downarrow\uparrow)$, when entering the ferromagnetic region. This effect is known as singlet-triplet mixing, and the resulting state is often referred to as the FFLO-state. However, as the Cooper-pairs move further into the ferromagnetic region, the exchange field $\mathbf{h}$ will try to flip spins pointing in the anti-parallel direction while leaving the others unchanged. Therefore, the exchange field will cause a phase difference between the electrons forming the Cooper-pair, eventually leaving the two electrons out of coherence and destroying the Cooper-pair. The length scale at which such unequal-spin states can survive is of order $\sqrt{D}/h$ where D is the diffusion constant and h is the magnitude of the exchange field [20].

However, we know that the state $(\uparrow\downarrow + \downarrow\uparrow)$ is not the only possible triplet state, we also have two triplet states with equal spins ($\uparrow\uparrow$ and $\downarrow\downarrow$). Unlike the singlet state, the triplet states are not rotationally invariant. The triplet states transform into each other when rotating the state in spin-space. Therefore, if we somehow could find a way of rotating the triplet state in the FFLO-state into one of these states with parallel spins, the exchange field would no longer lead to incoherence and hence we would expect the Cooper-pairs to survive longer. It is worth mentioning that such an equal spin triplet state is not only interesting because of their longer coherence length. They are also interesting from a fundamental point of view, as they can give rise to interesting effects in a ferromagnetic material such as domain wall motion, spin-transfer torques and magnetization switching [18].

Mainly, there are two ways of achieving such long-ranged Cooper-pairs in equilibrium. The first way of achieving this is by having an inhomogeneity in the exchange field (magnetic inhomogeneities). These magnetic inhomogeneities can originate from having a layered structure with several ferromagnets, each with a noncolinear alignment of the magnetizations [21, 22, 23], or from having a single ferromagnet with a local inhomogeneity in the magnetization [24, 25, 26, 27]. The second way of achieving such long-ranged Cooper-pairs is by having spin-orbit coupling present, as shown by Bergeret and Tokatly [28]. What Bergeret and Tokatly showed was that having a homogeneous exchange field but finite spin-orbit coupling (SO-coupling), gives rise to the exact same transport equations as while having a Bloch-domain wall with an inhomogeneous exchange field. This demonstrates that the singlet-triplet conversion caused by

SO-coupling can mathematically be described by a Bloch-domain wall with an inhomogeneous exchange field. Hence, SO-coupling is nothing but another way to mathematically describe a particular type of magnetic inhomogeneities. We could either have a inhomogeneous exchange field and zero SO-coupling in the ferromagnet, or we could have a homogeneous exchange field and a finite SO-coupling (corresponding to a Bloch-domain wall with zero SO-coupling). In both cases, the long-ranged triplet components are generated. As Bergeret and Tokatly showed, these long-ranged triplet states can now survive for a much longer length scale of order $\sqrt{D/2\pi T}$, where T is the temperature. Furthermore, it has been demonstrated that this coherence length for the long-ranged triplet component is of the same order as in a normal metal [24, 19]. Hence, SO-coupling provides a promising way to generate long-ranged triplet components, and different ways to achieve this intrinsic SO-coupling have received a lot of research recently[29, 30, 31, 32, 33].

However, in recent years it has also been shown that in an S/F/S-Josephson junction with SO-coupling, the phase difference ϕ between the superconductors can be used to generate and isolate these long-ranged triplet components [1]. Jacobsen and Linder found that having a phase difference of $\phi = \pi$ resulted in a giant peak in the local density of states, the very fingerprint of triplet states. They also showed that this giant triplet proximity effect can be predicted solely based on symmetry arguments, making it independent of the specific parameters. Furthermore, from these symmetry arguments, they could also argue that the observed peak in the density of states was entirely due to the long-ranged triplet components. What Jacobsen and Linder found is in stark contrast to the behaviour of an S/F/S-Josephson junction without SO-coupling and a phase difference of π, in which the proximity effect is suppressed. Hence, the S/F/S-Josephson junction with SO-coupling offers a promising way to create, control and isolate (equal spin) triplet Cooper-pairs. In this thesis, we will explore this phenomenon further by connecting two such systems by a feorrmagnetic nanowire, as suggested by Ouassou [34]. By doing so, we effectively create a Josephson junction with odd-frequency triplet states as the initial source of the Cooper-pairs by just using s-wave superconducotors.

1.2   SCOPE AND STRUCTURE

Before we can begin discussing particular systems, we will need some basic theory and tools. The goal of Chapter 2 - Chapter 4 is to establish the tools needed to describe and determine the Cooper-pairs in superconducting systems. In Chapter 2 we will introduce some fundamental concepts crucial to build up a physical intuition of what is going on in superconducting systems. In short, in sections 2.1 and 2.2 we discuss how the SO-coupling and the presence of interfaces affect the Cooper-pairs, respectively. We will also discuss the pairing symmetries for Cooper-pairs in section 2.3. Having a basic understanding of how Cooper-pairs conceptually behaves, we will in section 2.4 introduce the mathematical framework needed to describe Cooper-pairs, namely the Green's functions. Next, we will discuss the quasiclassical approximation, and how this alters the Green's functions in section 2.5. In Chapter 3, we extend our theoretical understanding by including a brief discussion of the BCS-theory. In Chapter 4 we focus on deriving the equations describing the Green functions in a general material. In the first part of Chapter 4, section 4.1, we use our established mathematical framework to derive the Usadel equation from the exact transport equation. Along with appropriate boundary conditions discussed in section 4.2, the Usadel equation determines the Green's functions in a general material. In section 4.3 we have included a brief discussion of the bulk solution in the case of a

conventional superconductor. In the second part of Chapter 4, section 4.4, we will introduce a common parameterization for numerical purposes, namely the Riccati-parameterization. Connecting everything we have learned so far, Chapter 5 focuses on expressing common physical observables in the established mathematical framework. We first introduce the d-vector formalism in section 5.1, before considering the density of states, current and the superconduitng gap in sections 5.2, 5.3 and 5.4 respectively.

While Chapter 2 - Chapter 4 focus on establishing the fundamental theory and equations determining the Green's functions for a general heterostructure, Chapter 6 focuses on preparing these equations for qualitative discussion of a specific type of system. The specific type of system of our choice is a one-dimensional S/F/S-Josephson junction with SO-coupling, the basic building block of the system we ultimately want to investigate. To prepare our equations for qualitative discussion, we first linearize the Usadel equation in section 6.1, followed by invoking the d-vector formalism in section 6.2 to easier distinguish the short-range and long-range triplet components. Finally, in section 6.3 we will also insert the relevant SO-coupling and exchange field. We have also included a short discussion of the dimensionless analogue of the equations in section 6.4. The resulting equations will become crucial when discussing specific systems in Chapter 7 and Chapter 8.

In Chapter 7, we reproduce the results for the one-dimensional S/F/S-Josephson junction with SO-coupling, first presented by Jacobsen and Linder [1]. The goal of this chapter is to develop a physical intuition of whats going on in the simpler system before dealing with our more complicated H-geometry. Having developed an understanding of the basic building block, we finally explore the H-geometry in Chapter 8, which is the main goal of this thesis. Before presenting the results, we will briefly discuss the experimental set-up and numerical method in section 8.1 and 8.2 respectively. Thereafter, we present the linearized equations in section 8.3 for a general exchange field. Finally, we discuss the results for the cases in which the central nanowire is a normal metal and a ferromagnet without and with SO-coupling in section 8.4, 8.5 and 8.6 respectively. To conclude this thesis, we give a summary and outlook in Chapter 9. Additional calculations, as well as the matlab code used to simulate the one-dimensional S/F/S-Josephson junction with SO-coupling, are included in Appendix A, B and C respectively.

FUNDAMENTAL CONCEPTS

The goal of this chapter is to introduce some fundamental concepts and theory, as well as to establish the mathematical framework needed to describe superconductivity. With these tools at hand, we will be better suited to deal with the equations revealing the precise behaviour of superconducting systems.

2.1 SPIN-ORBIT COUPLING

Spin-orbit (SO) coupling refers to the phenomena in which the spin of each quasiparticle couples to its momentum. In general, this is described by a linearized[1] single-particle Hamiltonian [28, 35]

$$H = -\mathbf{p} \cdot \underline{\mathcal{A}}/m, \tag{5}$$

where $\mathbf{p}$ is the momentum of the particle, m is the mass and $\underline{\mathcal{A}}$ is the SO-field. The SO-field $\underline{\mathcal{A}}$ is a 2×2 SU(2) vector field. It is an object with both vector structure in real space, and has a 2×2 matrix structure in spin-space [2].

There are two types of SO-coupling in solids: symmetry dependent and symmetry independent. Symmetry independent SO-coupling exists in all crystals as a result of SO-coupling in atomic orbitals. This type of SO-coupling is therefore solely material-dependent. On the other hand, symmetry dependent SO-coupling only exists in materials without inversion symmetry, meaning standing at an arbitrary point in the material, the system will not look the same if you invert your view. Mainly, there are two ways of breaking this inversion symmetry in a material, either by surface-induced asymmetry (Rashba) [36, 37, 38] or bulk-induced asymmetry (Dresselhaus) [39, 37].

Let us start by discussing surface-induced asymmetry, commonly referred to as Rashba SO-coupling. Imagine that a quasiparticle hits an interface and enters a new material with a electric field $\mathbf{E}$. As the electric and magnetic fields are related by a Lorentz-transformation changing the reference frame, the quasiparticle moving in an electric field will in its own reference frame experience a magnetic field. This effective magnetic field is proportional to $\mathbf{B}_{eff} \simeq \mathbf{E} \times \mathbf{p}/mc^2$, and gives rise to a Zeeman-energy term $H_{SO} = \mu_B \sigma \cdot \mathbf{B}_{eff}$ where μ_B is the Bohr-magneton. Defining the Rashba-constant α and writing the electric field as $\mathbf{E} = E\mathbf{e}_n$, the Hamiltonian describing Rashba SO-coupling becomes

$$H_R = -\frac{\alpha}{m}(\mathbf{e}_n \times \mathbf{p}) \cdot \sigma. \tag{6}$$

---

[1] Note that we here assume that SO-coupling is linear in momentum. This need not be the case, however, it is sufficient to describe the basic physics.

[2] The vector structure in real space and 2×2 matrix structure in spin-space can be more easily seen writing out the definition $\underline{\mathcal{A}}(\mathbf{r}, t) \equiv e\mathbf{A}(\mathbf{r}, t) + \mathbf{w}(\mathbf{r}, t)\sigma$. Here, $\mathbf{w}(\mathbf{r}, t)$ is some 3×3 matrix that parameterizes the linearized interaction.

Note that the normal-vector $\mathbf{e}_n$ is the direction of the electric field, or generally speaking the direction in which we have broken inversion symmetry. The broken inversion symmetry in Rashba SO-coupling therefore is a direct result of the presence of the interface, and its specific form depends on the geometry of the interface.

As a concrete example, let us consider a nanowire set-up, with the wire lying along the z-direction surrounded by vacuum. By symmetry arguments the electric field in the nanowire has to point radially outward in the xy-plane (or inwards, the sign does not matter in the end). Therefore, when the quasiparticle hits the interface, what it sees is a electric field $\mathbf{E} = \frac{1}{\sqrt{2}}E(\mathbf{e}_x + \mathbf{e}_y)$ where E is the strength of the electric field. Consequently, the normal vector $\mathbf{e}_n$ in eq.6 will in this case be $\mathbf{e}_n = (\mathbf{e}_x + \mathbf{e}_y)/\sqrt{2}$. Furthermore, having a nanowire along the z-direction, we can ignore momentum along the x- and y-direction. This can be justified by the restrictions the surrounding vacuum puts on the Green's functions. As will become clear later on, both the Green's functions and its derivative must be zero at the boundary of the nanowire (for details, see eq.79). Therefore, we can neglect p_x and p_y, giving momentum only in the z-direction $\mathbf{p} = p_z\mathbf{e}_z$. Thus, inserting the derived form of $\mathbf{e}_n$ in eq.6 results in a Hamiltonian $H_R = -\frac{\alpha}{m\sqrt{2}}(p_z\underline{\sigma}^1 - p_z\underline{\sigma}^2)$. Using eq.5 and redefining $\alpha/\sqrt{2} \to \alpha$, we find that the SO-field describing Rashba SO-coupling $\underline{A}_R$ in a nanowire set-up is given by $\underline{A}_R = (0, 0, \alpha(\underline{\sigma}^1 - \underline{\sigma}^2))$.

We now focus on the other origin of broken inversion symmetry, namely bulk-induced asymmetry. This type of SO-coupling is commonly referred to as Dresselhaus SO-coupling. As the name implies, Dresselhaus SO-coupling originates from a non-centrosymmetric lattice structure in the bulk of the material. In the original derivation the non-centrosymmetric lattice structure breaks the twofold degeneracy in the Brillouin zone, giving rise to an SO-coupling [39]. However, since Dresselhaus derived the SO-coupling from a two-dimensional electron gas (2DEG), the physical interpretation of Dresselhaus SO-coupling is not easily translated for the case of thin-film and nanowire structures. However, experiments show that the 2DEG-model describes well the underlying physics in materials like GaAs, a material commonly used in semiconductors [40, 41, 42] . It is also worth noticing that the term "bulk" in bulk-induced asymmetry may be misleading, especially when dealing with nanowire systems. Although the Dresselhaus contribution to SO-coupling in most cases can be neglected for nanowire systems, this need not always be the case [43]. This demonstrates the somewhat misleading term "bulk" for thin-film and nanowire systems. The term "bulk" does not actually refer to having a bulk region in our system, it refers to the material itself having Dresselhaus SO-coupling if we were in a bulk region. The Dresselhaus SO-coupling is therefore solely material-dependent, and the specific mathematical form depends on which crystal direction the quasiparticle propagates. For example, for (001)-oriented zinc-blende thin-films (corresponding to the z-direction) H_D becomes [39, 37]

$$H_D = \beta(\underline{\sigma}^2 p_y - \underline{\sigma}^1 p_x). \tag{7}$$

Now that we have an understanding of what SO-coupling is and where it comes from, it remains to invoke the SO-coupling in our mathematical description of the system. It turns out that (a linearized) SO-coupling is accounted for by simply replacing all derivatives with the covariant derivative defined by [28, 35]

$$\nabla \cdot \mapsto \tilde{\nabla} \equiv \nabla \cdot - [\check{A}, \cdot]_- \quad \text{with} \quad \check{A} = \begin{pmatrix} \underline{A} & 0 \\ 0 & -\underline{A}^* \end{pmatrix}. \tag{8}$$

2.2   PROXIMITY EFFECT, ANDREEV-REFLECTION AND JOSEPSHON JUNCTIONS

Imagine that we have two materials, one s-wave superconducting material and one non-superconducting material. If these two materials are kept apart, each of them is characterized by their own properties. But what happens near the interface when these two materials are brought together? As we have discussed earlier the Cooper-pairs will penetrate into the non-superconducting material, affecting the characteristic properties of the non-superconducting material in the vicinity of the interface. In other words, the characteristic properties of the superconductor have leaked into the non-superconducting material in the vicinity of the interface. This effect is known as the proximity effect. The leakage of the superconducting properties can be either weak (referred to as the weak proximity effect), strong (referred to as the strong proximity effect), or somewhere in between. For analytical calculations, it is useful to evaluate physical properties in the weak proximity limit, as it allows us to more easily see the qualitative behavior of our systems. That said, solving our system numerically, we need to account for the full proximity regime. It is worth mentioning that this also goes the other way around, the presence of the non-superconducting material will also affect the properties of the superconducting material at the vicinity of the interface. This is often referred to as the inverse proximity effect.

Let us discuss the proximity effect (and inverse) in more detail for the case when the non-superconducting material is a normal metal, that is we will consider a N/S-bilayer. At the interface, the proximity effect can be explained by Andreev reflection [44, 34, 45]. Let us discuss this mechanism in more detail. Suppose we have an incoming electron with spin up and momenta $\mathbf{k}$ hitting the N/S-interface from the right, with energy $\epsilon < \Delta$. Having an energy below the superconducting gap, the incoming electron itself cannot enter the superconductor, since there are no states available there. Therefore, the electron either has to be reflected as an electron or Andreev reflected as a hole. In the latter case, what actually happens is that the incoming electron teams up with an electron with spin down, momenta $-\mathbf{k}$ and energy $-\epsilon$ at the interface[3]. The two electrons now form a Cooper-pair which can enter the superconductor. At the same time, the missing electron at the interface leaves behind a hole travelling in the opposite direction. Thus, the net effect of this process, as illustrated in figure 3a, is to transfer two electrons with $|\epsilon| < \Delta$ from the normal metal into the superconductor, at the cost of reflecting a hole back into the normal metal. So how does this manifests in the density of states in the normal metal? Having the normal metal in contact with a superconductor we effectively take out two sub-gap electrons from the normal metal, resulting in a minigap in the density of states $D(\epsilon)$ around $\epsilon/\Delta_0 = 0$ where Δ_0 is the superconducting gap at absolute zero, as illustrated in figure 4a. The term minigap refers to the fact that the gap occurs for energies much smaller than the superconducting gap Δ_0.

---

[3] From the condition of the momenta being $-\mathbf{k}$ it follows directly that the energy need to be -ϵ.
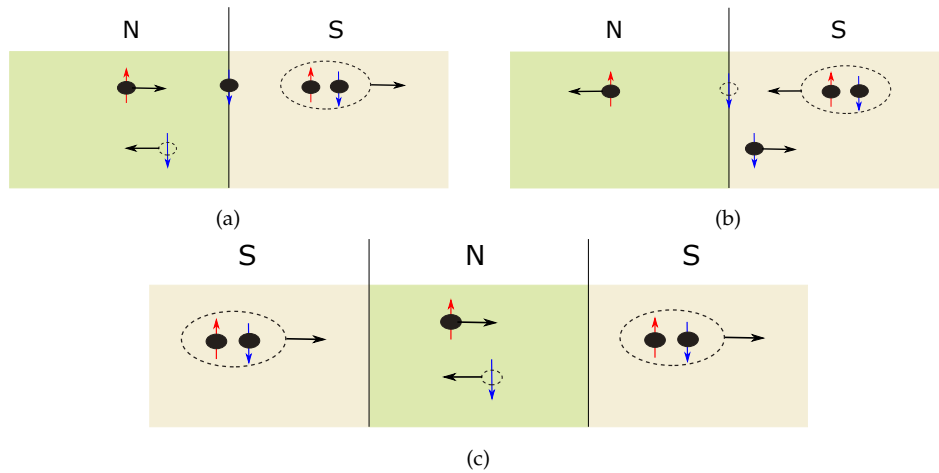
Figure 3: Illustration of Andreev reflection of a hole (a) and electron (b). The supercurrent in a S/N/S Josephson junction due to Andreev reflection of electrons and holes is also illustrated (c).

In the above, we discussed how an electron in a normal metal can be transmitted into a superconductor as a Cooper-pair. However, the process also works the other way around. Suppose we now instead have an incoming Cooper-pair from the right hitting the N/S-interface. When the Cooper-pair hits the interface, one of the electrons can combine with a corresponding hole at the interface, resulting in a reflected electron. The other electron can now be transmitted to the normal metal, assuming that there are available states there. Hence, one Cooper-pair is being destroyed due to the Andreev reflected electron, as illustrated in figure 3b. Having the superconductor in contact with a normal metal, we effectively destroy one Cooper-pair at the cost of creating an electron, now with energy $\epsilon < \Delta$. In terms of the density of states in the superconductor, we therefore get induced states within the gap characterizing the bulk of the superconductor, as shown in figure 4b.
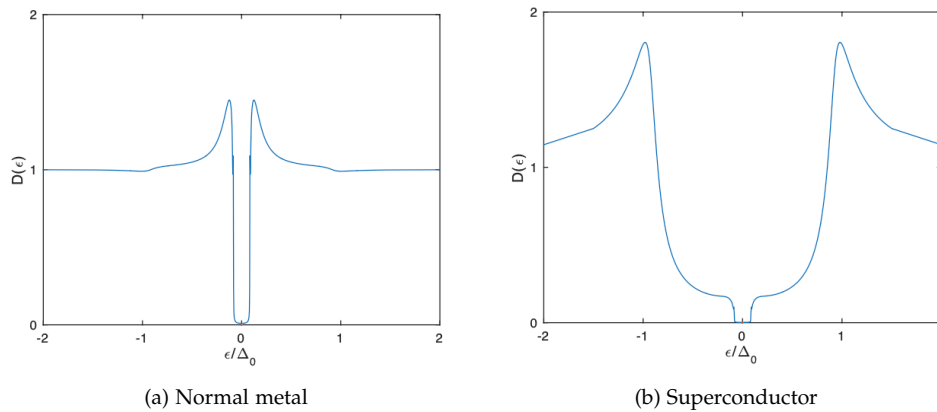

Figure 4: Density of states $D(\epsilon)$ in a normal metal (a) and a superconductor (b) for a S/N-bilayer, when taking into account both the effect S has on N and vice versa. Figures are taken from [46].

Now that we have seen how the proximity effect in a normal metal N and superconductor S can be explained by Andreev reflection of holes and electrons respectively, we can immediately explain how a supercurrent can appear in an S/N/S-Josephson junction. Let us say that we have an electron with spin up traveling to the right in N as shown in figure 3c. When the electron hits the interface to the right, a Cooper-pair is transmitted into S while a hole with spin down is created in N. The hole, which travels to the left in N, will eventually hit the left interface where it destroys one Cooper-pair in the left superconductor. Hence, we effectively have transmitted one Cooper-pair from the left superconductor to the right superconductor via Andreev-reflection.

For nonmagnetic interfaces and materials, the supercurrent going through the junction is determined by the phase difference ϕ between the two superconductors[4] [47, 48]

$$I = I_c \sin(\phi). \tag{9}$$

where I_c is the critical current reached at $\phi = \pm\pi/2$.

Integrating over the phase difference, we obtain an expression for the free energy of the system [5] [48]

$$E \simeq I_c(1 - \cos(\phi)). \tag{10}$$

When there are no magnetic elements present, the current is always positive. Looking at the expression for the free energy, we see that a positive current results in a ground state at $\phi = 0$, commonly referred to as 0-junctions. However, having magnetic elements present we can get a negative current, resulting in a ground state at $\phi = \pm\pi$. These types of Josephson junctions are commonly referred to as π-junctions [49]. In addition to the 0 and π-junctions, it is also possible to construct junctions where the ground state occurs for an arbrirary state $\phi \in [0, \pi]$, the so-called ϕ_0-junctions [50].

2.3 PARING SYMMETRIES AND SPIN-STATE TRANSFORMATIONS

As discussed in the introduction, Cooper-pairs can be in a singlet or triplet state. The singlet state is defined as the state with total spin angular momentum $s = 0$. The only state that satisfies this is the state $(\uparrow\downarrow - \downarrow\uparrow)$. On the other hand, triplet states are defined as states having total spin angular momentum $s = 1$. Having $s = 1$, there are three different allowed quantum numbers $m = -1, 0, 1$. This gives rise to the triplet states $(\downarrow\downarrow)$, $(\uparrow\downarrow + \downarrow\uparrow)$ and $(\uparrow\uparrow)$ respectively. In addition to the spin-symmetry property, Cooper-pairs also exhibits orbital and time symmetry properties, with the requirement of an antisymmetric total wavefunction.

The combination of the different symmetries for singlet and triplet states are shown in figure 5. In this figure, even symmetry is represented by purple, while odd symmetry is represented by green. Starting with the singlet state, we immediately notice that the singlet state is antisymmetric under the exchange of spins. Therefore the singlet state has a odd spin symmetry. Moving on to the orbital symmetry, there are mainly three options: s-orbital, d-orbital and p-orbital. Suppose that the singlet Cooper-pair has a s- or d-orbital. Since both s- and d-orbitals are even, the time symmetry has to be even to fulfill the antisymmetry of

---

[4] The expression was originally derived for a non-magnetic S/I/S-junction, where I is a insulator. Despite the more complex underlying physics present in junctions with magnetic elements, like S/F/S, the relation still manage to describe well the qualitative behaviour in these systems.

[5] To not be confused with the electric field.

the total wavefunction. Superconductors in which the Cooper-pairs have a singlet spin-state and an s-orbital are called s-wave superconductors, or conventional low-T superconductors. In the same manner, superconductors in which the Cooper-pairs have a singlet spin state and a d-orbital are called d-wave superconductors, or unconventional high-T superconductors. However, there is still one option for the orbital symmetry left, the singlet state can also have a p-orbital. Due to the fact that a p-orbital has an odd symmetry, the time symmetry now has to be odd. Moving on to the triplet states, we notice that the spin symmetry now becomes even. Again, the orbital symmetry can either be even, which is the case for s- and d-orbitals, or odd which is the case for p-orbitals. An even orbital symmetry results in an odd time symmetry, while an odd orbital symmetry results in an even time symmetry.

Although it is possible to construct Cooper-pairs in all configurations shown in figure 5, there are some configurations more common than others. In particular, Cooper-pairs with a orbital symmetry of p-wave are far less common than Cooper-pairs with a s- or d-wave orbital symmetry [51]. In addition, Cooper-pairs with a orbital symmetry of d-wave is less common than the Cooper-pairs with a orbital symmetry of s-wave. The reason why, is that both Cooper-pairs with a d- and p-wave symmetry are very sensitive to disorder compared to those with a s-wave symmetry, as they easily get destroyed by impurity scattering [52, 53, 54, 55]. In general, the effect of the scattering process is to modify the **k**-vector of the electron. When an electron moves through a material with a lot of disorder, the **k**-vector of the electron also gets more modified due to the larger number of scattering events compared to a material with less disorder. Looking at the orbital symmetry for the d- and p-wave in figure 5, we immediately see that the **k**-vector is more easily scattered out of these symmetries compared to the s-wave orbital symmetry. The d- and p-wave symmetry is simply less robust in terms of scattering. Hence, Cooper-pairs with a d- or p-wave symmetry will be more easily destroyed by disorder compared to a Cooper-pair with s-wave symmetry.
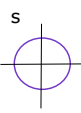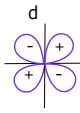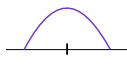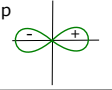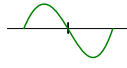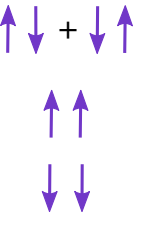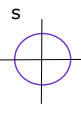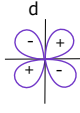

Figure 5: A overview of the different symmetry combinations for singlet and triplet states. Odd symmetry is represented by green, while the purple represents even symmetry.

In the above, we discussed the symmetry properties for both singlet and triplet spin states. Suppose we now have a (singlet) s-wave superconductor in contact with, for example a ferromagnetic material. In this case, we know that triplet states are generated in the ferromagnet due to singlet-triplet mixing. Let us now take a closer look at how this happens. For a ferromagnet with no exchange field, the energy dispersion relation for the spin-up electrons and spin-down electrons are equal and parabolic. However, when the field is nonzero things become different. Let us say that the **h**-field points up, then the Zeeman energy term causes a shift that lowers the parabola for spin-up represented by red in figure 6. On the contrary, the parabola gets lifted for spin-down represented by blue. Furthermore, from the BCS-theory we know that a Cooper-pair (in the singlet state) consist of one electron with spin up ↑ and wave-number **k** and one electron with spin down ↓ and wave-number −**k**. Therefore, only positive **k**'s are relevant for spin-up, while only negative **k**'s are relevant for spin-down. Hence, a Cooper-pair in a finite **h**-field is described by the energy dispersion relation shown in figure 6, where we have denoted the positive **k**'s as $\mathbf{k}_\uparrow$ and the negative **k**'s 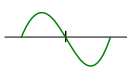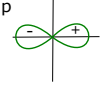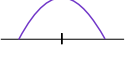as $\mathbf{k}_\downarrow$. If we now project this energy band onto the k-space, we clearly see that the Fermi-energy wavenumber k_F becomes shifted to new positions $\mathbf{k}_\uparrow + Q/2$ and $\mathbf{k}_\downarrow - Q/2$. As stated in the introduction this finite center-of-mass momentum $\pm Q$ causes the singlet state to transform according to $(\uparrow\downarrow - \downarrow\uparrow) \to (\uparrow\downarrow\, e^{i\mathbf{Q}\cdot\mathbf{R}} - \downarrow\uparrow\, e^{-i\mathbf{Q}\cdot\mathbf{R}}) = (\uparrow\downarrow - \downarrow\uparrow)\cos(\mathbf{Q}\cdot\mathbf{R}) + i(\uparrow\downarrow + \downarrow\uparrow)\sin(\mathbf{Q}\cdot\mathbf{R})$. In other words, the presence of an exchange field **h** results in a singlet-triplet mixing.
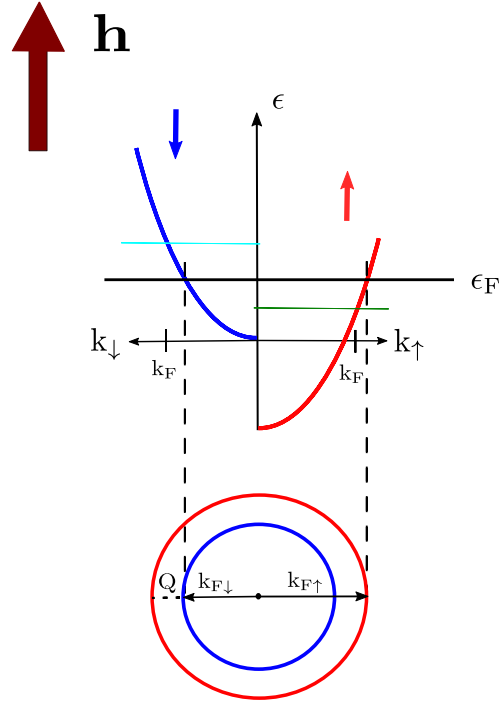

Figure 6: Illustration of how the presence of a finite exchange field **h** results in a finite center-of-mass momenta **Q**

Now that we understand how the singlet-triplet mixing happens, let us consider how the different states transforms under rotation in spin space. Suppose we want to express the basis vectors quantized along the direction θ, φ in terms of the basis vectors quantized along the z-axis, where θ, φ are the polar angle and azimuthal angle respectively. The transformation relating these two bases reads [56]

$$
\begin{aligned}
\uparrow_{\theta,\varphi} &= cos(\frac{\theta}{2})e^{-i\varphi/2}\uparrow_z + sin(\frac{\theta}{2})e^{i\varphi/2}\downarrow_z, \\
\downarrow_{\theta,\varphi} &= -sin(\frac{\theta}{2})e^{-i\varphi/2}\uparrow_z + cos(\frac{\theta}{2})e^{i\varphi/2}\downarrow_z.
\end{aligned}
\tag{11}
$$

From eq.11 it follows that the singlet-state and triplet state quantized along a general direction θ, φ becomes

$$
(\uparrow\downarrow - \downarrow\uparrow)_{\theta,\varphi} = (\uparrow\downarrow - \downarrow\uparrow)_z,
\tag{12}
$$

$$
(\uparrow\downarrow + \downarrow\uparrow)_{\theta,\varphi} = -\sin(\theta)[e^{-i\varphi}(\uparrow\uparrow)_z - e^{i\varphi}(\downarrow\downarrow)_z] + \cos(\theta)(\uparrow\downarrow + \downarrow\uparrow)_z.
\tag{13}
$$

Looking at eq.12 and eq.13 we clearly see that the singlet state is rotationally invariant in spin-space while the triplet state is not. This is an essential result because it demonstrates how the triplet state $(\uparrow\downarrow + \downarrow\uparrow)$ can be transformed into $\uparrow\uparrow$ or $\downarrow\downarrow$. For example, if we were to relate the basis vectors quantized along the y-axis to the z-axis, we notice that the y-axis corresponds to $\theta = \pi/2, \varphi = \pi/2$. Inserting these angles into eq.13 we find $(\uparrow\downarrow + \downarrow\uparrow)_{\theta=\pi/2,\varphi=\pi/2} = (\uparrow\downarrow + \downarrow\uparrow)_y = i(\uparrow\uparrow + \downarrow\downarrow)_z$.

The above discussion clearly demonstrates how we can transform the short-ranged singlet spin state into the long-ranged triplet spin state. Suppose we start with a s-wave superconductor, meaning that our Cooper-pair is in a singlet spin state and has s-orbital symmetry. Being subject to an exchange field, this Cooper-pair transforms into one singlet part and one triplet part according to the singlet-triplet mixing. Although both sates are still being short-ranged due to the unequal spins. Then, if we have a SO-field $\underline{A}$ present, the triplet part can be further rotated in spin-space, giving long-ranged Cooper-pairs with an equal-spin-state. If the SO-field has a nonzero component along the propagation direction of the system, the criterion for generating such long-ranged triplet components is a nonzero commutator $[\underline{A}, \mathbf{h} \cdot \sigma]_-$ [28, 35]. In contrast, if the component of the SO-field along the propagation direction of the system is zero, a commutator $[\underline{A}, [\underline{A}, \mathbf{h} \cdot \sigma]_-]_-$ not parallel to the exchange field $\mathbf{h} \cdot \sigma$ generates such long-ranged triplet components [28, 35].

2.4   GREEN'S FUNCTIONS

Green's functions are powerful tools in the context of many-body systems. Not only do they describe the transport properties of the electrons and holes in the system, common physical quantities like current and density of states can also be expressed by the Green's functions. Having found the Green's function of the system, we therefore have all information we need for determining common physical quantities. There are several ways of defining the Green's functions, for example the Matsubara imaginary-time formalism [57], and the Keldysh real-time formalism [58]. In this thesis we will use the latter.

In the Keldysh formalism we define a set of three Green's functions describing the transport of electrons and holes. These quantum field correlation functions are called the retarded,

advanced and Keldysh Green's functions. The Green's functions describe the correlation between an electron with spin σ and position $\mathbf{r_1}$ at a time t_1, and another electron with spin σ' and position $\mathbf{r_2}$ at a time t_2 [59]

$$G^{\mathrm{R}}_{\sigma\sigma'}(\mathbf{r_1}, t_1; \mathbf{r_2}, t_2) = -i\langle[\Psi_\sigma(\mathbf{r_1}, t_1), \Psi^\dagger_{\sigma'}(\mathbf{r_2}, t_2)]_+\rangle\theta(t_1 - t_2), \tag{14}$$

$$G^{\mathrm{A}}_{\sigma\sigma'}(\mathbf{r_1}, t_1; \mathbf{r_2}, t_2) = i\langle[\Psi_\sigma(\mathbf{r_1}, t_1,), \Psi^\dagger_{\sigma'}(\mathbf{r_2}, t_2)]_+\rangle\theta(t_2 - t_1,), \tag{15}$$

$$G^{\mathrm{K}}_{\sigma\sigma'}(\mathbf{r_1}, t_1; \mathbf{r_2}, t_2) = -i\langle[\Psi_\sigma(\mathbf{r_1}, t_1), \Psi^\dagger_{\sigma'}(\mathbf{r_2}, t_2)]_-\rangle. \tag{16}$$

Their anomalous counterparts, which are only present in superconducting systems, are defined by

$$F^{\mathrm{R}}_{\sigma\sigma'}(\mathbf{r_1}, t_1; \mathbf{r_2}, t_2) = -i\langle[\Psi_\sigma(\mathbf{r_1}, t_1), \Psi_{\sigma'}(\mathbf{r_2}, t_2)]_+\rangle\theta(t_1 - t_2), \tag{17}$$

$$F^{\mathrm{A}}_{\sigma\sigma'}(\mathbf{r_1}, t_1; \mathbf{r_2}, t_2) = i\langle[\Psi_\sigma(\mathbf{r_1}, t_1), \Psi_{\sigma'}(\mathbf{r_2}, t_2)]_+\rangle\theta(t_2 - t_1), \tag{18}$$

$$F^{\mathrm{K}}_{\sigma\sigma'}(\mathbf{r_1}, t_1; \mathbf{r_2}, t_2) = -i\langle[\Psi_\sigma(\mathbf{r_1}, t_1), \Psi_{\sigma'}(\mathbf{r_2}, t_2)]_-\rangle. \tag{19}$$

First, let us focus on the set of Green's functions defined in eq.14 - eq.16. From eq.14 we see that the retarded Green's function G^{R} only becomes nonzero for $t_1 > t_2$. The retarded Green's function therefore corresponds to the creation of an electron at $(\mathbf{r_2}, t_2)$, and then at a later time the destruction of an electron at $(\mathbf{r_1}, t_1)$. Since the Fermi-sphere is filled at low temperatures, the only empty state for the electron to be created at is outside the Fermi-sphere. Hence we have a particle-like excitation. Furthermore, from eq.15 we see that the advanced Green's function G^{A} only is nonzero for $t_2 > t_1$. The advanced Green's function therefore corresponds to the destruction of an electron at $(\mathbf{r_1}, t_1)$ and then at a later time the creation of an electron at $(\mathbf{r_2}, t_2)$. Again, having filled the Fermi-sphere, the destroyed electron will be inside the Fermi-sphere, creating a hole. Hence, we have a hole-like like excitation. In conclusion, the retarded Green's function describes electrons moving forward in time, while the advanced Green's function describes electrons moving backward in time, which is equivalent to holes moving forward in time.

Finally, we notice from eq.16 that the Keldysh Green's function G^{K} is the only function defined without a Heaviside step-function. In addition it is worth noticing that the Keldysh Green's function is the only one defined with the commutator, while the two others are defined with the anti-commutator. Unlike the retarded and advanced components, the Keldysh component contains information about the nonequilibrium properties of the system.

While the set of Green's functions in eq.14 - eq.16 are present in all many-body systems, the anomalous Green's functions defined in eq.17 - eq.19 only exists in superconducting systems. Not only do they exist, they are crucial for describing superconducting systems. Recall that the underlying mechanism for superconductivity are two electrons being paired up in a Cooper-pair. In terms of field operators, Cooper-pairs correspond to creating an electron at position $\mathbf{r_1}$ and time t_1, while creating another electron at position $\mathbf{r_2}$ and time t_2. This is exactly the type of correlations the anomalous Green's functions in eq.17 - eq.19 describe.

The definition of the Green's functions and the corresponding anomalous counterparts are all defined with a general σ and σ'. If we now introduce the basis-vector $\Psi(\mathbf{r}_1, t_1) = (\Psi_\uparrow(\mathbf{r}_1, t_1), \Psi_\downarrow(\mathbf{r}_1, t_1), \Psi_\uparrow^\dagger(\mathbf{r}_1, t_1), \Psi_\downarrow^\dagger(\mathbf{r}_1, t_1))^T$, we can account for all combinations of the two spins, resulting in the following matrices in spin-space

$$\underline{G}^R = \begin{pmatrix} G_{\uparrow\uparrow}^R & G_{\uparrow\downarrow}^R \\ G_{\downarrow\uparrow}^R & G_{\downarrow\downarrow}^R \end{pmatrix}, \qquad \underline{G}^A = \begin{pmatrix} G_{\uparrow\uparrow}^A & G_{\uparrow\downarrow}^A \\ G_{\downarrow\uparrow}^A & G_{\downarrow\downarrow}^A \end{pmatrix}, \qquad \underline{G}^K = \begin{pmatrix} G_{\uparrow\uparrow}^K & G_{\uparrow\downarrow}^K \\ G_{\downarrow\uparrow}^K & G_{\downarrow\downarrow}^K \end{pmatrix}, \tag{20}$$

$$\underline{F}^R = \begin{pmatrix} F_{\uparrow\uparrow}^R & F_{\uparrow\downarrow}^R \\ F_{\downarrow\uparrow}^R & F_{\downarrow\downarrow}^R \end{pmatrix}, \qquad \underline{F}^A = \begin{pmatrix} F_{\uparrow\uparrow}^A & F_{\uparrow\downarrow}^A \\ F_{\downarrow\uparrow}^A & F_{\downarrow\downarrow}^A \end{pmatrix}, \qquad \underline{F}^K = \begin{pmatrix} F_{\uparrow\uparrow}^K & F_{\uparrow\downarrow}^K \\ F_{\downarrow\uparrow}^K & F_{\downarrow\downarrow}^K \end{pmatrix}. \tag{21}$$

These matrices can be combined further to form the following three matrices in Nambu space

$$\hat{G}^R \equiv \begin{pmatrix} \underline{G}^R & \underline{F}^R \\ \underline{F}^{R*} & \underline{G}^{R*} \end{pmatrix}, \qquad \hat{G}^A \equiv \begin{pmatrix} \underline{G}^A & \underline{F}^A \\ \underline{F}^{A*} & \underline{G}^{A*} \end{pmatrix}, \qquad \hat{G}^K \equiv \begin{pmatrix} \underline{G}^K & \underline{F}^K \\ -\underline{F}^{K*} & -\underline{G}^{K*} \end{pmatrix}. \tag{22}$$

Finally, to fully describe the general system, we can form the full 8×8 matrix in Keldysh-space

$$\check{G} \equiv \begin{pmatrix} \hat{G}^R & \hat{G}^K \\ 0 & \hat{G}^A \end{pmatrix}. \tag{23}$$

2.5 QUASICLASSICAL APPROXIMATION

From the definitions of the Green's functions (eq.14 - eq.19) we see that these functions depend on two spatial coordinates, $\mathbf{r}_1$ and $\mathbf{r}_2$, and two time coordinates, t_1 and t_2. Let us introduce a set of new center of mass coordinates, $\mathbf{R}$ and T, and difference coordinates, $\mathbf{r}$ and t. This set of new coordinates are related to our old coordinates $(\mathbf{r}_1, t_1)$ and $(\mathbf{r}_2, t_2)$ by [59]

$$\mathbf{r}_1 \equiv \mathbf{R} - \mathbf{r}/2, \qquad \mathbf{r}_2 \equiv \mathbf{R} + \mathbf{r}/2, \tag{24}$$

$$t_1 \equiv T - t/2, \qquad t_2 \equiv T + t/2. \tag{25}$$

Expressing the Green's function by these new coordinates $\check{G}(\mathbf{R}, T; \mathbf{r}, t)$, we notice that there are two ways this function can oscillate; either by variations in the difference coordinates $\mathbf{r}$ and t, or by variations of the center-of-mass coordinates $\mathbf{R}$ and T. The first way of oscillation originates from the two electrons forming the Cooper-pair. Since the electrons are confined close to the Fermi-surface with $|\mathbf{p}_F| = p_F$, these oscillations are over a length scale of $\lambda_F = 2\pi/p_F$. The second way of oscillation originates from the material as the electrons move through. For instance, having a normal metal, the length in which the Cooper-pairs can propagate is determined by the temperature $\xi_T = p_F/mT$ regardless of which spin state the Cooper-pairs have. If we instead have a ferromagnet though, the triplet Cooper-pairs with an equal-spin state who are defined as long-ranged, still have a coherence length determined by the temperature. Yet the triplet Cooper-pairs with an unequal spin-state, the short-ranged states, now have a shorter coherence length $\xi_F = p_F/mh$ due to the effect of the exchange field. By the same mechanism, Cooper-pairs in the singlet spin state will also have a coherence length ξ_F in a

ferromagnet, as this state also has unequal spins. Finally, for a superconducting material, the superconducting gap determines the coherence lenght $\xi_0 = p_F/m\Delta$. In our systems these are all typically much longer than λ_F. As we are interested in variations at a longer length scale, we therefore Fourier-transform $\check{G}(\mathbf{R}, T; \mathbf{r}, t)$ with respect to $\mathbf{r}$ and t, giving

$$\check{G}(\mathbf{R}, T; \mathbf{p}, \epsilon) = \int e^{i\epsilon t} e^{-i\mathbf{p}\cdot\mathbf{r}} \check{G}(\mathbf{R}, T; \mathbf{r}, t) d\mathbf{r} dt. \tag{26}$$

Next, we use the quasiclassical approximation. Since all conducting electrons lie close to the Fermi-surface, we restrict the magnitude of $\mathbf{p}$ to be the value at the Fermi-surface p_F. However, we still have to keep the dependence of the direction of the momentum. Introducing the variable $\xi_{\mathbf{p}} = \mathbf{p}^2/2m - \mu$, the quasiclassical approximation can be expressed as

$$\check{G}(\mathbf{R}, T; \mathbf{p}, \epsilon) \approx -i\pi\delta(\xi_{\mathbf{p}}) \cdot \check{g}(\mathbf{R}, T; \mathbf{e}_{p_F}, \epsilon). \tag{27}$$

Here $\mathbf{e}_{p_F}$ refers to the direction of the momentum at the Fermi-surface, and $\check{g}(\mathbf{R}, T; \mathbf{e}_{p_F}, \epsilon)$ is called the quasi-classical Green's function.

Alternatively, one can find $\check{g}(\mathbf{R}, T; \mathbf{e}_{p_F}, \epsilon)$ by integrating over all values of $\xi_{\mathbf{p}}$

$$\check{g}(\mathbf{R}, T; \mathbf{e}_{p_F}, \epsilon) = \frac{i}{\pi} \int d\xi_{\mathbf{p}} \cdot \check{G}(\mathbf{R}, T; \mathbf{p}, \epsilon). \tag{28}$$

The π-factor in the definitions above comes from the normalization condition.

In summary, the quasiclassical Green's function becomes

$$\check{g} = \begin{pmatrix} \hat{g}^R & \hat{g}^K \\ 0 & \hat{g}^A \end{pmatrix}, \tag{29}$$

with

$$\hat{g}^R = \begin{pmatrix} \underline{g}^R & \underline{f}^R \\ -\underline{f}^{R*} & -\underline{g}^{R*} \end{pmatrix}, \qquad \hat{g}^A = \begin{pmatrix} \underline{g}^A & \underline{f}^A \\ -\underline{f}^{A*} & -\underline{g}^{A*} \end{pmatrix}, \qquad \hat{g}^K = \begin{pmatrix} \underline{g}^K & \underline{f}^K \\ \underline{f}^{K*} & \underline{g}^{K*} \end{pmatrix}. \tag{30}$$

Note that in the quasiclassical Green's function it is the retarded and advanced components rather than the Keldysh-component that have a minus sign in the second row.

2.5.1   Useful relations

As a simple task, we will now derive some useful relations between the components of the Green's function. Starting with the definition of $\hat{G}^R$, we use the dagger operator, i.e. the conjugate transpose, and get the matrix

$$\hat{G}^{R\dagger}(\mathbf{r}_1, t_1; \mathbf{r}_2, t_2) = \begin{pmatrix} G^{R*}_{\uparrow\uparrow} & G^{R*}_{\downarrow\uparrow} & F^{R}_{\uparrow\uparrow} & F^{R}_{\downarrow\uparrow} \\ G^{R*}_{\uparrow\downarrow} & G^{R*}_{\downarrow\downarrow} & F^{R}_{\uparrow\downarrow} & F^{R}_{\downarrow\downarrow} \\ F^{R*}_{\uparrow\uparrow} & F^{R*}_{\downarrow\uparrow} & G^{R}_{\uparrow\uparrow} & G^{R}_{\downarrow\uparrow} \\ F^{R*}_{\uparrow\downarrow} & F^{R*}_{\downarrow\downarrow} & G^{R}_{\uparrow\downarrow} & G^{R}_{\downarrow\downarrow} \end{pmatrix}. \tag{31}$$

In the above matrix, each element has the same argument as $\hat{G}^{R\dagger}(\mathbf{r}_1, t_1; \mathbf{r}_2, t_2)$, even though this is not written explicitly.

Looking at the definition in eq.14, we notice that $G_{\sigma\sigma'}^{R*}$ can be written as

$$
\begin{aligned}
G_{\uparrow\uparrow}^{R*}(\mathbf{r}_1, t_1; \mathbf{r}_2, t_2) &= +i\langle[\Psi_\uparrow(\mathbf{r}_1, t_1), \Psi_\uparrow^\dagger(\mathbf{r}_2, t_2)]_+^*\rangle\theta(t_1 - t_2) \\
&= +i\langle[\Psi_\uparrow^\dagger(\mathbf{r}_1, t_1), \Psi_\uparrow(\mathbf{r}_2, t_2)]_+\rangle\theta(t_1 - t_2) \\
&= G_{\uparrow\uparrow}^A(\mathbf{r}_2, t_2; \mathbf{r}_1, t_1),
\end{aligned}
\tag{32}
$$

$$
\begin{aligned}
G_{\downarrow\uparrow}^{R*}(\mathbf{r}_1, t_1; \mathbf{r}_2, t_2) &= +i\langle[\Psi_\downarrow(\mathbf{r}_1, t_1), \Psi_\uparrow^\dagger(\mathbf{r}_2, t_2)]_+^*\rangle\theta(t_1 - t_2) \\
&= +i\langle[\Psi_\downarrow^\dagger(\mathbf{r}_1, t_1), \Psi_\uparrow(\mathbf{r}_2, t_2)]_+\rangle\theta(t_1 - t_2) \\
&= G_{\uparrow\downarrow}^A(\mathbf{r}_2, t_2; \mathbf{r}_1, t_1),
\end{aligned}
\tag{33}
$$

$$
\begin{aligned}
G_{\uparrow\downarrow}^{R*}(\mathbf{r}_1, t_1; \mathbf{r}_2, t_2) &= +i\langle[\Psi_\uparrow(\mathbf{r}_1, t_1), \Psi_\downarrow^\dagger(\mathbf{r}_2, t_2)]_+^*\rangle\theta(t_1 - t_2) \\
&= +i\langle[\Psi_\uparrow^\dagger(\mathbf{r}_1, t_1), \Psi_\downarrow(\mathbf{r}_2, t_2)]_+^*\rangle\theta(t_1 - t_2) \\
&= G_{\downarrow\uparrow}^A(\mathbf{r}_2, t_2; \mathbf{r}_1, t_1),
\end{aligned}
\tag{34}
$$

$$
\begin{aligned}
G_{\downarrow\downarrow}^{R*}(\mathbf{r}_1, t_1; \mathbf{r}_2, t_2) &= +i\langle[\Psi_\downarrow(\mathbf{r}_1, t_1), \Psi_\downarrow^\dagger(\mathbf{r}_2, t_2)]_+^*\rangle\theta(t_1 - t_2) \\
&= +i\langle[\Psi_\downarrow^\dagger(\mathbf{r}_1, t_1), \Psi_\downarrow(\mathbf{r}_2, t_2)]_+\rangle\theta(t_1 - t_2) \\
&= G_{\downarrow\downarrow}^A(\mathbf{r}_2, t_2; \mathbf{r}_1, t_1).
\end{aligned}
\tag{35}
$$

Similarly, using eq.17 we find the following elements for $F_{\sigma\sigma'}^{R*}$

$$
\begin{aligned}
F_{\uparrow\uparrow}^R(\mathbf{r}_1, t_1; \mathbf{r}_2, t_2) &= -i\langle[\Psi_\uparrow(\mathbf{r}_1, t_1), \Psi_\uparrow(\mathbf{r}_2, t_2)]_+\rangle\theta(t_1 - t_2) \\
&= -F_{\uparrow\uparrow}^A(\mathbf{r}_2, t_2; \mathbf{r}_1, t_1),
\end{aligned}
\tag{36}
$$

$$
\begin{aligned}
F_{\downarrow\uparrow}^R(\mathbf{r}_1, t_1; \mathbf{r}_2, t_2) &= -i\langle[\Psi_\downarrow(\mathbf{r}_1, t_1), \Psi_\uparrow(\mathbf{r}_2, t_2)]_+\rangle\theta(t_1 - t_2) \\
&= -F_{\uparrow\downarrow}^A(\mathbf{r}_2, t_2; \mathbf{r}_1, t_1),
\end{aligned}
\tag{37}
$$

$$
\begin{aligned}
F_{\uparrow\downarrow}^R(\mathbf{r}_1, t_1; \mathbf{r}_2, t_2) &= -i\langle[\Psi_\uparrow(\mathbf{r}_1, t_1), \Psi_\downarrow(\mathbf{r}_2, t_2)]_+\rangle\theta(t_1 - t_2) \\
&= -F_{\downarrow\uparrow}^A(\mathbf{r}_2, t_2; \mathbf{r}_1, t_1),
\end{aligned}
\tag{38}
$$

$$
\begin{aligned}
F_{\downarrow\downarrow}^R(\mathbf{r}_1, t_1; \mathbf{r}_2, t_2) &= -i\langle[\Psi_\downarrow(\mathbf{r}_1, t_1), \Psi_\downarrow(\mathbf{r}_2, t_2)]_+\rangle\theta(t_1 - t_2) \\
&= -F_{\downarrow\downarrow}^A(\mathbf{r}_2, t_2; \mathbf{r}_1, t_1).
\end{aligned}
\tag{39}
$$

Inserting the above expressions, $\hat{G}^{R\dagger}$ can be expressed by the advanced components as follows

$$\hat{G}^{R\dagger}(\mathbf{r}_1, t_1; \mathbf{r}_2, t_2)$$
$$= \begin{pmatrix} G^A_{\uparrow\uparrow}(\mathbf{r}_2, t_2; \mathbf{r}_1, t_1) & G^A_{\uparrow\downarrow}(\mathbf{r}_2, t_2; \mathbf{r}_1, t_1) & -F^A_{\uparrow\uparrow}(\mathbf{r}_2, t_2; \mathbf{r}_1, t_1) & -F^A_{\uparrow\downarrow}(\mathbf{r}_2, t_2; \mathbf{r}_1, t_1) \\ G^A_{\downarrow\uparrow}(\mathbf{r}_2, t_2; \mathbf{r}_1, t_1) & G^A_{\downarrow\downarrow}(\mathbf{r}_2, t_2; \mathbf{r}_1, t_1) & -F^A_{\downarrow\uparrow}(\mathbf{r}_2, t_2; \mathbf{r}_1, t_1) & -F^A_{\downarrow\downarrow}(\mathbf{r}_2, t_2; \mathbf{r}_1, t_1) \\ -F^{A*}_{\uparrow\uparrow}(\mathbf{r}_2, t_2; \mathbf{r}_1, t_1) & -F^{A*}_{\uparrow\downarrow}(\mathbf{r}_2, t_2; \mathbf{r}_1, t_1) & G^{A*}_{\uparrow\uparrow}(\mathbf{r}_2, t_2; \mathbf{r}_1, t_1) & G^{A*}_{\uparrow\downarrow}(\mathbf{r}_2, t_2; \mathbf{r}_1, t_1) \\ -F^{A*}_{\downarrow\uparrow}(\mathbf{r}_2, t_2; \mathbf{r}_1, t_1) & -F^{A*}_{\downarrow\downarrow}(\mathbf{r}_2, t_2; \mathbf{r}_1, t_1) & G^{A*}_{\downarrow\uparrow}(\mathbf{r}_2, t_2; \mathbf{r}_1, t_1) & G^{A*}_{\downarrow\downarrow}(\mathbf{r}_2, t_2; \mathbf{r}_1, t_1) \end{pmatrix}. \tag{40}$$

Multiplying the above matrix by $(\tau^3 \otimes \sigma^0)$ on both sides, we find a relation between the retarded and advanced components

$$\hat{G}^A(\mathbf{r}_2, t_2; \mathbf{r}_1, t_1) = (\tau^3 \otimes \sigma^0)\hat{G}^{R\dagger}(\mathbf{r}_1, t_1; \mathbf{r}_2, t_2)(\tau^3 \otimes \sigma^0). \tag{41}$$

However, in most cases we are interested in the quasiclassical Green's function. To see how the relation in eq.41 transforms in the quasiclassical approximation, we can simply use the definition in eq.26 and eq.28

$$\hat{g}^A(\mathbf{R}, T; \mathbf{e}_{p_F}, \epsilon) \tag{42}$$
$$= \frac{i}{\pi} \int d\zeta_{\mathbf{p}} \int e^{i\epsilon t} e^{-i\mathbf{p}\cdot\mathbf{r}} \hat{G}^A(\mathbf{R}, T; \mathbf{r}, t) d\mathbf{r} dt$$
$$= \frac{i}{\pi} \int d\zeta_{\mathbf{p}} \int e^{i\epsilon t} \cdot e^{-i\mathbf{p}\cdot\mathbf{r}} \hat{G}^A((\mathbf{r}_1 + \mathbf{r}_2)/2, (t_1 + t_2)/2; \mathbf{r}_2 - \mathbf{r}_1, \mathbf{t}_2 - \mathbf{t}_1) d\mathbf{r} dt$$
$$= \frac{i}{\pi} \int d\zeta_{\mathbf{p}} \int e^{i\epsilon t} \cdot e^{-i\mathbf{p}\cdot\mathbf{r}} (\tau^3 \otimes \sigma^0)\hat{G}^{R\dagger}((\mathbf{r}_2 + \mathbf{r}_1)/2, (t_2 + t_1)/2; \mathbf{r}_1 - \mathbf{r}_2, \mathbf{t}_1 - \mathbf{t}_2)(\tau^3 \otimes \sigma^0) d\mathbf{r} dt$$
$$= -\left[\frac{i}{\pi} \int d\zeta_{\mathbf{p}} \int e^{-i\epsilon t} \cdot e^{+i\mathbf{p}\cdot\mathbf{r}} (\tau^3 \otimes \sigma^0)\hat{G}^R((\mathbf{r}_2 + \mathbf{r}_1)/2, (t_2 + t_1)/2; \mathbf{r}_1 - \mathbf{r}_2, \mathbf{t}_1 - \mathbf{t}_2)(\tau^3 \otimes \sigma^0) d\mathbf{r} dt \right]^\dagger$$
$$= -\left[\frac{i}{\pi} \int d\zeta_{\mathbf{p}} \int e^{-i\epsilon t} \cdot e^{+i\mathbf{p}\cdot\mathbf{r}} (\tau^3 \otimes \sigma^0)\hat{G}^R(\mathbf{R}, T; -\mathbf{r}, -t)(\tau^3 \otimes \sigma^0) d\mathbf{r} dt \right]^\dagger$$
$$= -\left[\frac{i}{\pi} \int d\zeta_{\mathbf{p}} \int e^{+i\epsilon t} \cdot e^{-i\mathbf{p}\cdot\mathbf{r}} (\tau^3 \otimes \sigma^0)\hat{G}^R(\mathbf{R}, T; +\mathbf{r}, +t)(\tau^3 \otimes \sigma^0) d\mathbf{r} dt \right]^\dagger$$
$$= -(\tau^3 \otimes \sigma^0)\hat{g}^{R\dagger}(\mathbf{R}, T; \mathbf{e}_{p_F}, \epsilon)(\tau^3 \otimes \sigma^0). \tag{43}$$

In the above calculation there are two steps worth noticing. In the third line we have used that when inserting the relation in eq.41, we also have to interchange the roles of $(\mathbf{r}_1, t_1)$ and $(\mathbf{r}_2, t_2)$. However, integrating over all $\mathbf{r}$ and t in the sixth line, we can redefine $\mathbf{r}$ and t to their negative counterparts. Therefore, the interchanging of $(\mathbf{r}_1, t_1)$ and $(\mathbf{r}_2, t_2)$ in eq.41, will in the quasiclassical approximation preserve the roles of the relevant arguments. In short-hand notation, the relation between the retarded and advanced components of quasiclassical Green's function may be written

$$\hat{g}^A = -(\tau^3 \otimes \sigma^0)\hat{g}^{R\dagger}(\tau^3 \otimes \sigma^0). \tag{44}$$

Thus far, we have seen how to relate the retarded and advanced Green's functions. It turns out that there also exists a relation relating the Keldysh component to the retarded and advanced Green's function in equilibrium [59, 60]. The relation in question is the following $\hat{g}^K = (\hat{g}^R h - h\hat{g}^A)$, where h is some distribution function that is not unique. Using the definitions of the Green's functions one can show, by similar calculation as above, that one choice for the distribution function is $h = \tanh(\beta\tilde{\epsilon}_k/2)$, where $\tilde{\epsilon}_k$ is the quasiparticle energy measured with respect to the Fermi-level[61]. The relation between the Keldysh, retarded and advanced components in equilibrium therefore reads

$$\hat{g}^K = (\hat{g}^R - \hat{g}^A)\tanh(\beta\tilde{\epsilon}_k/2). \tag{45}$$

BCS-THEORY

Conventional s-wave low-temperature superconductors are well described by the BCS-theory developed by Bardeen, Cooper and Schrieffer [8]. Even though there are some major assumptions that limit the validity of the theory, the BCS-theory does a good job in describing the underlying physics for conventional s-wave superconductors. In this chapter, we will present the key-points of the theory.

3.1 THE ORIGIN OF THE ATTRACTIVE POTENTIAL

As stated in the introduction, the Cooper-pairs in a s-wave superconductor is the result of an attractive interaction between the the two electrons due to the lattice vibrations. Let us now investigate how this attractive interaction comes about. Our starting point is the Hamiltonian describing a system in which we both have electron-electron interaction and electron-phonon interactions. In reciprocal space this Hamiltonian is given by [11]

$$H = \sum_{\mathbf{k},\sigma}(\epsilon_{\mathbf{k}} - \mu)c^{\dagger}_{\mathbf{k}\sigma}c_{\mathbf{k}\sigma} + \sum_{\mathbf{k},\mathbf{k}',\mathbf{q},\sigma,\sigma'} \tilde{V}_{eff}c^{\dagger}_{\mathbf{k}+\mathbf{q},\sigma}c^{\dagger}_{\mathbf{k}'-\mathbf{q},\sigma'}c_{\mathbf{k}',\sigma'}c_{\mathbf{k}\sigma}. \tag{46}$$

Here $\epsilon_{\mathbf{k}}$ is the excitation spectrum of a free electron gas and $\tilde{V}_{eff} = 2|g_{\mathbf{q}}|^2\omega_{\mathbf{q}}/(\omega^2 - \omega_{\mathbf{q}}^2) + V_{columb}(\mathbf{q})$ is the effective potential. Note that due to the summations over $\mathbf{k}, \mathbf{k}', \mathbf{q}$ $\tilde{V}_{eff}$ is a function of the phonon frequency ω. Also $c^{\dagger}_{\mathbf{k}\sigma}$ and $c_{\mathbf{k}\sigma}$ are the creation and destruction operators, respectively.

Let us take a closer look at how $\tilde{V}_{eff}$ depends on the phonon-frequency ω. The effective potential consists of two terms, the first term originates from the electron-phonon interaction, while the second term originates from the electron-electron interaction. We start by discussing the first term. Looking at the expression for $\tilde{V}_{eff}$ we notice that the first term does contain a factor $2|g_{\mathbf{q}}|^2$. This factor just tells us something about the strength of the electron-phonon interaction; nevertheless, it is always positive. Therefore, the first term will be proportional to $\omega_{\mathbf{q}}/(\omega^2 - \omega_{\mathbf{q}}^2)$ where $\omega_{\mathbf{q}}$ is some fixed frequency, as sketched in figure 7. We notice that as $|\omega| \to \omega_{\mathbf{q}}^-$ a negative singularity appears. Furthermore, for frequencies higher than $\omega_{\mathbf{q}}$ the function is positive, while its negative for frequencies below $\omega_{\mathbf{q}}$. Moving on to the second term, we know that this goes like $\mathbf{q}^{-2}$, thus the second term will always be positive.
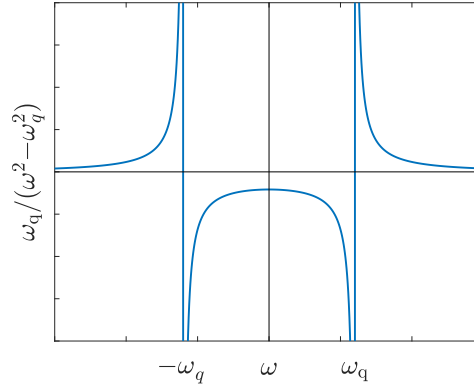
Figure 7: A qualitative sketch of the first term in $\tilde{V}_{eff}$.

The sign of $\tilde{V}_{eff}$ depends on the balance of the two terms. Let us know investigate when, if possible, $\tilde{V}_{eff}$ becomes negative. Since the second term always is positive, the only chance of getting a negative $\tilde{V}_{eff}$ is for the first term to be negative and beat the second term in magnitude. Due to the negative singularities of the first term as $|\omega| \to \omega_q^-$, the first term will always beat the positive second term for these frequencies, resulting in a negative potential. Remarkably, this holds no matter how weak the strength of the electron-phonon interaction is. In contrast if ω is very small the second term beats the first term resulting in a positive effective potential[1]. Finally, for large frequencies above ω_q both terms are positive, so $\tilde{V}_{eff}$ surely is positive also in this case. Hence there is a small frequency-window at $\omega \lesssim \omega_q$ where the effective potential $\tilde{V}_{eff}$ is negative, i.e. attractive.

This clearly demonstrates the origin of the attractive potential in the BCS-theory being a delicate balance between the electron-phonon interaction and the electron-electron interaction. As we have just seen, for this outcome to be an attractive interaction, the frequency need to be within a small frequency-window $\omega \lesssim \omega_q$. However, when the frequency are within this small window, the effective interaction is attractive no matter how weak the strength of the electron-phonon interaction is. This justifies the physical interpretation of the BCS-theory given in the introduction. Remember, we have two electrons moving in a lattice of positively charged ions. As the first electron moves though the lattice, it creates a shift in the local charge distribution. For the second electron to experience an attractive interaction, it cannot come too fast nor wait too long. If it waits too long or the lattice vibrates too fast, the positively charged ion will relax to the initial position, meaning that we no longer have a shifted local charge distribution. At the same time, the second electron cannot come to fast either, since the repulsive Coulomb force between the electrons then would win over the attractive force from the shifted charge distribution. The BCS-theory is therefore limited to describing low-temperature superconductors. For high temperatures, i.e. high phonon frequency, the effective interaction is no longer attractive, and the BCS-theory is no longer valid.

---

[1] The magnitude of the electron-phonon interaction typically is much smaller than the electron-electron interaction

The first assumption made in the BCS-theory is that the electrons only interact with each other within a thin shell around the Fermi-sphere. Thus, $\epsilon_k, \epsilon_{k'}, \epsilon_{k+q}$ and $\epsilon_{k'-q}$ must all lie inside a thin shell around the Fermi-surface. Let us now see how this assumption affects k'. In figure 8 we have sketched the Fermi-sphere, denoting the thin shell around as stipulated lines. The green vector denotes k, the red vector denotes k' and the blue vector denotes q. From this sketch we see that $\epsilon_{k'-q}$ in general lies outside the shell even though ϵ_k, $\epsilon_{k'}$ and ϵ_{k+q} lies within the shell. However, if we where to choose $k' = -k$ also $\epsilon_{k'-q}$ lies within the shell. This choice of k' also maximize the scattering phase space for attractive interactions. We therefore choose $k' = -k$ in what follows.
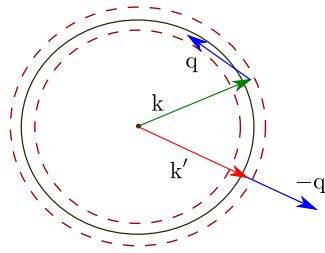
Figure 8: Illustration of the kinematics governing the wave-vectors k and k' in the BCS-Hamiltonian. The black line represents the Fermi-sphere, while the stipulated red line represents the thin shell around the Fermi-sphere where electrons interact.

The second assumption made in the BCS-theory is that $\sigma' = -\sigma$. This assumption is justified by the fact that if we where to only have an interaction between two electrons, the spins have to be opposite to obtain an antisymmetric wavefunction. Having interactions between all electrons within a thin shell around the Fermi-sphere, as in our case, the antisymmetry of the many-body wavefunction becomes more complicated. However, it turns out that the choice of $\sigma' = -\sigma$ works well.

Finally redefining variables $k \rightarrow k'$ and $k + q \rightarrow k$, we end up with the standard BCS-Hamiltonian

$$H = \sum_{\mathbf{k},\sigma} (\epsilon_k - \mu) c_{k\sigma}^{\dagger} c_{k\sigma} + \sum_{k,k'} V_{kk'} c_{k,\uparrow}^{\dagger} c_{-k,\downarrow}^{\dagger} c_{-k',\downarrow} c_{k'\uparrow}. \tag{47}$$

Note that in the above equation we have used the fact that the effective potential $\tilde{V}_{eff}$ is spin independent and redefined $\tilde{V}_{eff} \rightarrow V_{kk'}/2$. If k and k' lies within a thin shell around the Fermi-sphere $V_{kk'}$ is attractive, otherwise $V_{kk'}$ is zero.

3.3 MEAN-FIELD APPROXIMATION

The BCS-Hamiltonian in eq.47 cannot be treated exactly. It is therefore useful to approximate the Hamiltonian. For this purpose we will use the mean-field approximation which now will be introduced. We start by rewriting $c_{-k,\downarrow} c_{k\uparrow}$ and $c_{k,\uparrow}^{\dagger} c_{-k,\downarrow}^{\dagger}$ in terms of the average value

$$c_{-k,\downarrow}c_{k\uparrow} = \langle c_{-k,\downarrow}c_{k\uparrow}\rangle + (c_{-k,\downarrow}c_{k\uparrow} - \langle c_{-k,\downarrow}c_{k\uparrow}\rangle)$$
$$\equiv b_k + \delta b_k, \tag{48}$$

$$c_{k,\uparrow}^\dagger c_{-k,\downarrow}^\dagger = \langle c_{k,\uparrow}^\dagger c_{-k,\downarrow}^\dagger\rangle + (c_{k,\uparrow}^\dagger c_{-k,\downarrow}^\dagger - \langle c_{k,\uparrow}^\dagger c_{-k,\downarrow}^\dagger\rangle)$$
$$\equiv b_k^\dagger + \delta b_k^\dagger, \tag{49}$$

where we have defined the statistical averages

$$b_k = \langle c_{-k,\downarrow}c_{k\uparrow}\rangle, \tag{50}$$

$$b_k^\dagger = \langle c_{k,\uparrow}^\dagger c_{-k,\downarrow}^\dagger\rangle. \tag{51}$$

Next, we insert these expressions for $c_{-k,\downarrow}c_{k\uparrow}$ and $c_{k,\uparrow}^\dagger c_{-k,\downarrow}^\dagger$ into the BCS-Hamiltonian in eq.47, and impose the mean-field approximation by ignoring terms of order $\mathcal{O}(\delta b_k^2)$

$$
\begin{aligned}
H &= \sum_{\mathbf{k},\sigma}(\epsilon_k - \mu)c_{k\sigma}^\dagger c_{k\sigma} + \sum_{k,k'}V_{kk'}c_{k,\uparrow}^\dagger c_{-k,\downarrow}^\dagger c_{-k',\downarrow}c_{k'\uparrow} \\
&= \sum_{\mathbf{k},\sigma}(\epsilon_k - \mu)c_{k\sigma}^\dagger c_{k\sigma} + \sum_{k,k'}V_{kk'}(b_k^\dagger + \delta b_k^\dagger)(b_{k'} + \delta b_{k'}) \\
&\simeq \sum_{\mathbf{k},\sigma}(\epsilon_k - \mu)c_{k\sigma}^\dagger c_{k\sigma} + \sum_{k,k'}V_{kk'}(b_k^\dagger b_{k'} + b_k^\dagger \delta b_{k'} + \delta b_k^\dagger b_{k'}) \\
&= \sum_{\mathbf{k},\sigma}(\epsilon_k - \mu)c_{k\sigma}^\dagger c_{k\sigma} + \sum_{k,k'}V_{kk'}(b_k^\dagger b_{k'} + b_k^\dagger c_{-k',\downarrow}c_{k'\uparrow} + b_{k'}c_{k,\uparrow}^\dagger c_{-k,\downarrow}^\dagger - 2b_k^\dagger b_{k'}).
\end{aligned} \tag{52}
$$

We now proceed by defining the following quantities

$$\Delta_k = -\sum_{k'}V_{kk'}b_{k'}, \tag{53}$$

$$\Delta_{k'}^\dagger = -\sum_{k}V_{kk'}b_k^\dagger. \tag{54}$$

Applying the above definitions, the Hamiltonian reads

$$H = \sum_{\mathbf{k},\sigma}(\epsilon_k - \mu)c_{k\sigma}^\dagger c_{k\sigma} - \sum_{k}(\Delta_k c_{k,\uparrow}^\dagger c_{-k,\downarrow}^\dagger + \Delta_k^\dagger c_{-k,\downarrow}c_{k\uparrow}) + \sum_{k}\Delta_k b_k^\dagger. \tag{55}$$

Comparing the above Hamiltonian with the standard BCS-Hamiltonian in eq.47, we notice that using mean-field approximation we have managed to transform the Hamiltonian from a many-body problem to a one-particle problem. Admittedly, at the cost of neglecting higher-order terms in δb_k, making the BCS-theory incapable of capturing the effects of higher-order terms. This is the second assumption that limits the validity of the BCS-theory.

3.4 THE GAP EQUATION

In the previous section we managed to reduce the many-body Hamiltonian into a one-particle Hamiltonian. Nevertheless, looking at eq.55 we notice that the Hamiltonian is not diagnolized. To diagnoalize the Hamiltonian we introduce some new fermionic operators

$$\begin{pmatrix} \eta_k \\ \gamma_k \end{pmatrix} = \begin{pmatrix} u_k & v_k \\ -v_k & u_k \end{pmatrix} \begin{pmatrix} c_{k\uparrow} \\ c^{\dagger}_{-k,\downarrow} \end{pmatrix} ; \qquad u_k = \cos(\theta_k), v_k = \sin(\theta_k). \tag{56}$$

Seeking a diagnolized Hamiltonian we want to express the Hamiltonian in terms of coefficients on the form $\gamma_k^{\dagger}\gamma_k$ and $\eta_k^{\dagger}\eta_k$. In contrast, coefficients that are a mixture of η_k and γ_k, like $\eta_k^{\dagger}\gamma_k$, must vanish. We start by focusing on the coefficients that do have to vanish. Inserting our new fermionic operators into eq.55, and demanding that coefficients on the form $\eta_k^{\dagger}\gamma_k$ have to vanish, we obtain the following two equations

$$-2(\epsilon_k - \mu)u_k v_k = u_k^2 \Delta_k - v_k^2 \Delta_k^{\dagger}, \tag{57}$$

$$-2(\epsilon_k - \mu)u_k v_k = u_k^2 \Delta_k^{\dagger} - v_k^2 \Delta_k. \tag{58}$$

Adding the above equations and using the relation $\Delta_k + \Delta_k^{\dagger} = 2\text{Re}(\Delta_k) \equiv 2\tilde{\Delta}_k$, we obtain the following equation

$$-4(\epsilon_k - \mu)u_k v_k = 2(u_k^2 - v_k^2)\tilde{\Delta}_k. \tag{59}$$

Redefining the quasi-particle energy with respect to the Fermi level $\tilde{\epsilon}_k \equiv \epsilon_k - \mu$, as well as utilizing the mathematical form of u_k and v_k, the above equation transforms according to

$$-2\tilde{\epsilon}_k u_k v_k = (u_k^2 - v_k^2)\tilde{\Delta}_k$$

$$-\tilde{\epsilon}_k \sin(2\theta_k) = \tilde{\Delta}_k \cos((2\theta_k)$$

$$\tan(2\theta_k) = -\frac{\tilde{\Delta}_k}{\tilde{\epsilon}_k}. \tag{60}$$

Choosing $\tilde{\Delta}_k$ to be positive and using the identity $\sin^2(2\theta_k) + \cos^2(2\theta_k) = 1$, one can show that eq.60 results in the following expression for $\cos(2\theta_k)$

$$\cos(2\theta_k) = \begin{cases} -\frac{1}{\sqrt{1+(\tilde{\Delta}_k/\tilde{\epsilon}_k)^2}} & ; \tilde{\epsilon}_k > 0 \\ +\frac{1}{\sqrt{1+(\tilde{\Delta}_k/\tilde{\epsilon}_k)^2}} & ; \tilde{\epsilon}_k < 0. \end{cases} \tag{61}$$

We now move on to the coefficients that do not vanish, namely $\gamma_k^{\dagger}\gamma_k$ and $\eta_k^{\dagger}\eta_k$. Again, inserting our new fermionic operators into eq.55, the coefficients of $\gamma_k^{\dagger}\gamma_k$ and $\eta_k^{\dagger}\eta_k$ respectively yields the following

$$(\epsilon_k - \mu)(v_k^2 - u_k^2) + u_k v_k(\Delta_k + \Delta_k^{\dagger}), \tag{62}$$

$$(\epsilon_k - \mu)(u_k^2 - v_k^2) - u_k v_k(\Delta_k + \Delta_k^{\dagger}). \tag{63}$$

Using eq.60 and eq.61 the coefficients for $\gamma_k^\dagger \gamma_k$ and $\eta_k^\dagger \eta_k$ simplifies to $\sqrt{\tilde{\epsilon}_k^2 + \tilde{\Delta}_k^2}$ and $-\sqrt{\tilde{\epsilon}_k^2 + \tilde{\Delta}_k^2}$ respectively.

We are now finally able to write down the diagnolized Hamiltonian in the mean field approximation

$$H = \sum_k [(\tilde{\epsilon}_k - \mu) + \Delta_k b_k^\dagger] + \sum_k E_k (\gamma_k^\dagger \gamma_k - \eta_k^\dagger \eta_k); \qquad E_k = \sqrt{\tilde{\epsilon}_k^2 + \tilde{\Delta}_k^2}. \tag{64}$$

Looking at the diagonalized Hamiltonian above, we notice that it consists of two parts, one representing the ground-state energy and one representing the excitation spectrum for our new fermionic operators γ_k and η_k. In other words, our new fermionic operators γ_k and η_k represents nothing but long-lived excitations.

By invoking the mean-field approximation and introducing some new operators, we have managed to diagnolize the BCS-Hamiltonian. However, we still need to find an equation determining Δ_k. We do so by using the definition of Δ_k in eq.53 along with the definition of b_k in eq.50

$$\begin{aligned}
\Delta_k &= -\sum_{k'} V_{kk'} b_{k'} \\
&= -\sum_{k'} V_{kk'} \langle c_{-k',\downarrow} c_{k'\uparrow} \rangle \\
&= -\sum_{k'} V_{kk'} \langle (v_{k'} \eta_{k'}^\dagger - u_{k'} \gamma_{k'}^\dagger)(u_{k'} \eta_{k'} + v_{k'} \gamma_{k'}) \rangle \\
&= -\sum_{k'} V_{kk'} u_{k'} v_{k'} (\langle \eta_{k'}^\dagger \eta_{k'} \rangle + \langle \gamma_{k'}^\dagger \gamma_{k'} \rangle) \\
&= -\sum_{k'} V_{kk'} u_{k'} v_{k'} \left(\frac{1}{e^{-\beta E_{k'}} + 1} - \frac{1}{e^{\beta E_{k'}} + 1} \right) \\
&= -\sum_{k'} V_{kk'} u_{k'} v_{k'} \tanh(\beta E_{k'}/2).
\end{aligned} \tag{65}$$

Using eq.60 and eq.61 we can relate u_k and v_k to Δ_k and $\tilde{\epsilon}_k$

$$\begin{aligned}
\Delta_k &= -\sum_{k'} V_{kk'} \frac{1}{2} \sin(2\theta_{k'}) \tanh(\beta E_{k'}/2) \\
&= -\sum_{k'} V_{kk'} \frac{1}{2} \frac{\tilde{\Delta}_{k'}/\tilde{\epsilon}_{k'}}{\sqrt{1 + (\tilde{\Delta}_{k'}/\tilde{\epsilon}_{k'})^2}} \tanh(\beta E_{k'}/2) \\
&= -\sum_{k'} V_{kk'} \frac{\tilde{\Delta}_{k'}}{2E_{k'}} \tanh(\beta E_{k'}/2).
\end{aligned} \tag{66}$$

Where we in the second line have utilized the particle-hole symmetry by choosing the + sign of $\cos(2\theta_{k'})$ in eq.61.

The above equation is referred to as the BCS-gap equation. The physical interpretation of Δ_k is that it is a gap in the excitation spectrum. To see this let us plot the excitation spectrum for the new fermionic operators γ_k and η_k given by $\pm E_k$. We start by setting $\Delta_k = 0$, then

$E_{\mathrm{k}} = |\tilde{\epsilon}_{\mathrm{k}}|$ and $-E_{\mathrm{k}} = -|\tilde{\epsilon}_{\mathrm{k}}|$. Remembering that $\tilde{\epsilon}_{\mathrm{k}}$ represent the excitation spectrum for a free electron gas, we expect the standard parabolic dispersion relation. However, since we are only interested in k's around the Fermi-wavevector, we can linearize the dispersion relation around k_F, thus giving a linear dispersion relation for large k's. Taking the absolute value we obtain the dispersion relation for E_{k} and $-E_{\mathrm{k}}$ represented by the blue and green stipulated lines respectively in figure 9. If we now include a finite gap $\Delta_{\mathrm{k}} \neq 0$ on the Fermi-surface the dispersion relations now reads $\pm E_{\mathrm{k}} = \pm\sqrt{\tilde{\epsilon}_{\mathrm{k}}^2 + \tilde{\Delta}_{\mathrm{k}}^2}$. Thus, the dispersion relation for E_{k} is raised with respect to the k-axis, represented by the blue line in figure 9. Similarly, the dispersion relation for $-E_{\mathrm{k}}$ get lowered with respect to the k-axis, represented by the green line in figure 9. Hence, the presence of a finite Δ_{k} results in a gap of $2\Delta_{\mathrm{k}}$ in the excitation spectrum. As there are no energy eigenvalues inside this gap, the gap protects electrons from scattering, thus giving zero resistance.

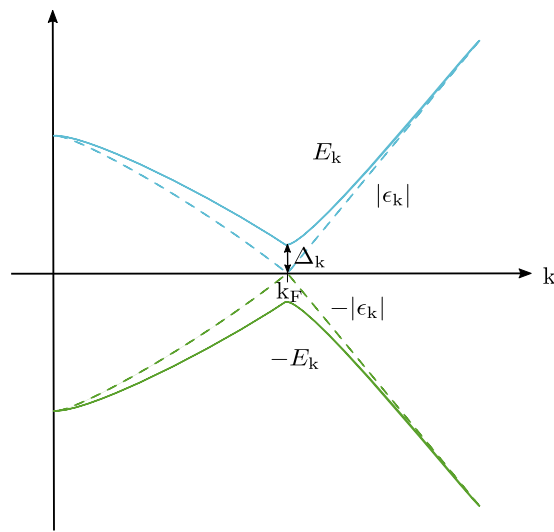Figure 9: Illustration of the physical meaning of the superconducting gap Δ_{k}. As the gap goes from a zero value, shown by stipulated lines, to a nonzero value, shown by full lines, a gap of $2\Delta_{\mathrm{k}}$ opens up in the excitation spectrum.

USADEL

The goal of this chapter is to derive the equations determining the Green's function in a general material. In the first part of this chapter, we focus on deriving these equations. We will start by deriving the Usadel equation for a general material from the exact transport equation. Moreover, since we are interested in describing systems in equilibrium, the Usadel equation simplifies. Next, a discussion of appropriate boundary conditions follows. In the second part of this chapter we introduce a useful parameterization for numeric simulations, the so-called Riccati-parameterization. Riccati-parameterizing the Usadel equation, along with appropriate boundary conditions, provides us with the tools needed for numerical simulations.

4.1 USADEL EQUATION

Suppose we have a material in which electromagnetic fields, superconducting properties, ferromagnetic properties, SO-coupling, spin-flip scattering and impurity scattering all can be present. The exact transport equation for such a material is [62, 61]

$$\frac{\mathbf{p}}{m}\{\nabla_{\mathbf{R}}\check{G} - i[\check{\mathcal{A}},]^{\bullet}_{-}\} = i[\epsilon\tau^3\otimes\underline{\sigma}^0 - \hat{\Delta} + \mathbf{h}\cdot\hat{\sigma} - V_{sf}\mathbf{s}\cdot\hat{\sigma} - e\varphi - V_{imp},\check{G}]^{\bullet}_{-}$$
$$+ \frac{1}{4m}\{[\nabla_{\mathbf{R}}\check{\mathcal{A}},\check{G}]^{\bullet}_{+} + [\check{\mathcal{A}},\nabla_{\mathbf{R}}\check{G}]^{\bullet}_{+}\} - \frac{i}{2m}[\check{\mathcal{A}}^2,\check{G}]^{\bullet}_{-}. \tag{67}$$

Here $\bullet$ is the bullet-product[1], $\mathbf{s} = \mathbf{s}(\mathbf{R}, T)$ is the spin field of the magnetic impuriies and φ is the scalar electromagnetic background field. Moreover, the matrices $\check{\mathcal{A}}$, $\hat{\Delta}$ and $\hat{\sigma}$ are defined as

$$\hat{\Delta} = \begin{pmatrix} 0 & 0 & 0 & \Delta \\ 0 & 0 & -\Delta & 0 \\ 0 & \Delta^* & 0 & 0 \\ -\Delta^* & 0 & 0 & 0 \end{pmatrix}, \qquad \check{\mathcal{A}} = \begin{pmatrix} \underline{\mathcal{A}} & 0 \\ 0 & -\underline{\mathcal{A}}^* \end{pmatrix}, \qquad \hat{\sigma} = \begin{pmatrix} \sigma & 0 \\ 0 & \sigma^* \end{pmatrix}. \tag{68}$$

As a first step to simplify the above equation, we use the quasiclassical approximation. That is, in our type of systems, the length L typically is much longer than the wavelength λ_F of the electrons forming the Cooper-pair. Hence, to leading order the transport equation is given by the terms of lowest order in the smallness parameter $\eta \equiv \lambda_F/L$. Furthermore, we notice that $\tilde{\nabla}_{\mathbf{R}} = (\nabla_{\mathbf{R}} - i\check{\mathcal{A}}) \sim 1/L$ and $\mathbf{p} \sim p_F \sim 1/\lambda_F$.

Looking at eq.67 we see that the left-hand side goes like $1/m\lambda_F L$. Hence, in terms of the smallness parameter η, the left-hand side goes like $\eta/m\lambda_F^2$. Furthermore, the last three terms on the right-hand side all go like $1/mL^2$, or equivalently as $\eta^2/m\lambda_F^2$. The three last terms in eq.67 can therefore be discarded when evaluating to leading order in η.

---

[1] $A \bullet B \equiv \exp\{\frac{1}{2}(\partial_\epsilon^A\partial_T^B - \partial_T^A\partial_\epsilon^B)\}\exp\{\frac{1}{2}(\nabla_{\mathbf{R}}^A\nabla_{\mathbf{p}}^B - \nabla_{\mathbf{p}}^A\nabla_{\mathbf{R}}^B)\}A(\mathbf{R},\mathbf{p},\epsilon,T)B(\mathbf{R},\mathbf{p},\epsilon,T)$; where $\nabla_{\mathbf{R}}^A$ means differention with respect to $\mathbf{R}$ only affecting function A etc. [62]

Next, we expand the gradient in the definition of the bullet product in terms of η. Looking at the definition of the bullet product, we realize that only the energy and time derivatives remain, leaving us with what we define as the ring-product $\circ$ [2]. Thus, keeping only the zero'th order reduces the bullet product to a ring product. Moreover, since $\check{A}$ is time-independent, we can replace the left hand side with the covariant derivative $\tilde{\nabla}$, where we have dropped the subscript $\mathbf{R}$. Finally, letting $\mathbf{p}/m \to \mathbf{v}_F$ and $\check{G} \to \check{g}$, we arrive at an equation referred to as the Eilenberger equation

$$\mathbf{v}_F \cdot \tilde{\nabla}\check{g} = i[\epsilon\tau^3 \otimes \underline{\sigma}^0 - \hat{\Delta} + \mathbf{h} \cdot \hat{\sigma} - V_{sf}\mathbf{s} \cdot \hat{\sigma} - e\varphi - V_{imp}, \check{g}]_-^\circ. \tag{69}$$

4.1.1 *Diffusive limit*

We now take into account impurity scattering in the material. Due to the relatively high concentration of nonmagnetic impurities in the diffusive limit, and hence a high frequency of random scattering events, the Green's function becomes nearly isotropic. We can therefore approximate the Green's function to a first-order expansion in spherical harmonics [59]

$$\check{g}(\mathbf{R}, T; \mathbf{e}_{\mathbf{p}_F}, \epsilon) \cong \check{g}_s(\mathbf{R}, T; \epsilon) + \mathbf{e}_{\mathbf{p}_F} \cdot \check{g}_p(\mathbf{R}, T; \epsilon). \tag{70}$$

Here $\check{g}_s$ is the isotropic (in momentum space) s-wave component of the Green's function, while $\check{g}_p$ denote the non-isotropic p-wave component. To take into account the direction of momentum, the p-wave component is multiplied by $\mathbf{e}_{\mathbf{p}_F}$.

Furthermore, evaluating in the diffusive limit, we can express the impurity potential and spin-flip potential by introducing the momentum relaxation time τ_0 and the spin relaxation time τ_s [59]

$$V_{imp} \cong -\frac{i}{2\tau_0}\langle\check{g}\rangle, \qquad V_{sf}\mathbf{s} \cdot \hat{\sigma} \cong -\frac{i}{2\tau_s}(\tau^3 \otimes \underline{\sigma}^0)\langle\check{g}\rangle(\tau^3 \otimes \underline{\sigma}^0). \tag{71}$$

Defining $v_0 \equiv 1/2\tau_0$ and $v_s \equiv 1/2\tau_s$ and using that $\langle\check{g}\rangle = \langle\check{g}_s\rangle + \langle\mathbf{e}_{\mathbf{p}_F} \cdot \check{g}_p\rangle = \check{g}_s$, the potentials simplify to

$$V_{imp} \cong -iv_0\check{g}_s, \qquad V_{sf}\mathbf{s} \cdot \hat{\sigma} \cong -iv_s(\tau^3 \otimes \underline{\sigma}^0)\check{g}_s(\tau^3 \otimes \underline{\sigma}^0). \tag{72}$$

If we now insert eq.72 into eq.69, rewrite $\mathbf{v}_F = v_F\mathbf{e}_{\mathbf{p}_F}$ and finally average over the Fermi-surface, we get the following equation[3]

$$\frac{1}{3}v_F \cdot \tilde{\nabla}\check{g}_p = i[\epsilon\tau^3 \otimes \underline{\sigma}^0 - \hat{\Delta} + \mathbf{h} \cdot \hat{\sigma} + iv_s(\tau^3 \otimes \underline{\sigma}^0)\check{g}_s(\tau^3 \otimes \underline{\sigma}^0) - e\phi, \check{g}_s]_-^\circ. \tag{73}$$

The equation above depends both on $\check{g}_s$ and $\check{g}_p$. To decompose the equation, we need an expression that relates the two components. The normalization condition $\check{g} \circ \check{g} = 1$ provides such a relation [62, 59]

$$\check{g}_p = -\tau_0 v_F\check{g}_s \circ \tilde{\nabla}\check{g}_s. \tag{74}$$

---

[2] $A \circ B \equiv \exp\{\frac{1}{2}(\partial_\epsilon^A \partial_T^B - \partial_T^A \partial_\epsilon^B)\}A(\mathbf{R}, \mathbf{p}, \epsilon, T)B(\mathbf{R}, \mathbf{p}, \epsilon, T)$
[3] Notice that the impurity scattering term vanishes since $[\check{g}_s, \check{g}_s]_-^\circ = 0$.

Defining the diffusion coefficient $D \equiv \frac{1}{3}v_F^2\tau_0$ and inserting 74 into 73, we arrive at the well-known Usadel equation

$$iD\tilde{\nabla}\cdot(\check{g}_s \circ \tilde{\nabla}\check{g}_s) = [\epsilon\tau^3\otimes\underline{\sigma}^0 - \hat{\Delta} + \mathbf{h}\cdot\hat{\sigma} + iv_s(\tau^3\otimes\underline{\sigma}^0)\check{g}_s(\tau^3\otimes\underline{\sigma}^0) - e\varphi, \check{g}_s]_-^\circ. \tag{75}$$

In the same manner as the exact transport equation, the Usadel equation describes the transport of electrons and holes in a general system. However, having used the quasiclassical approximation and the diffusive limit, we have managed to significantly simplify the exact transport equation. Not only have we managed to reduce the bullet-product to a ring-product, we have also managed to decouple the s- and p-wave components of the Green's function. Having determined the s-wave component of the Green's function using eq.75, we can always find the p-component by using the relation in eq.74. For further details and discussion of the derivations of the Eilenberger and Usadel equations, we refer to [59, 62, 61]. It is also worth noticing that the only place the SO-field enters in the Usadel equation is in the covariant derivative, instead of separate commutator terms as in the exact transport equation.

4.1.2 *Equilibrium, dimensionality and ideal materials*

The Usadel equation as it stands in eq.75 holds for a time-dependent $\check{g}_s$. However, if the system is in equilibrium, the Green's function $\check{g}_s$ will become time independent. In this limit the Usadel equation simplifies further. First, we notice that $e\varphi$ is just a scalar, so it clearly commutes with $\check{g}_s$. Therefore the term $e\varphi$ in the commutator vanishes. Furthermore, since the Green's function $\check{g}_s$ is time-independent, the ring-product reduces to just normal matrix multiplication. This follows directly from the definition of the ring product. Finally, we know that the components of $\check{g}_s$ are not all independent, and in equilibrium are related by eq.44 and eq.45. We therefore do not have to solve the Usadel equation for all three components, if we know for instance $\hat{g}_s^R$ we also know $\hat{g}_s^A$ and $\hat{g}_s^K$. In summary, the Usadel equation in equilibrium becomes

$$iD\tilde{\nabla}\cdot(\hat{g}_s^R \cdot \tilde{\nabla}\hat{g}_s^R) = [\epsilon\tau^3\otimes\underline{\sigma}^0 - \hat{\Delta} + \mathbf{h}\cdot\hat{\sigma} + iv_s(\tau^3\otimes\underline{\sigma}^0)\check{g}_s(\tau^3\otimes\underline{\sigma}^0), \hat{g}_s^R]_-. \tag{76}$$

The equation above is a three-dimensional equation. However, the systems we are going to evaluate in the end are one-dimensional, since one-dimensional systems can be solved directly numerically[4]. The underlying physics in one-dimensional systems is also easier to grasp, making such systems well suited for qualitative discussion. Mainly, there are two ways to achieve such one-dimensional systems, either by having thin films or nanowires. In both cases, spatial confinement makes the system one-dimensional. In the following, we will discuss these two ways in the case of propagation direction along z, assuming the SO-coupling to be of Rashba-type.

The first way of constructing such a system is by having a finite extent in the z-direction, while the system is so large along the x and y-direction that it can be treated as translation invariant in the xy-plane. Geometrically, this type of set-up corresponds to a thin film with the layering direction in z. Since the system is translation invariant in the xy-plane, the broken-inversion symmetry vector $\mathbf{e}_n$ in eq.6 is pointing in z-direction. Inserting $\mathbf{e}_n = \mathbf{e}_z$ in eq.6 we

---

[4] For a discussion of how one could solve three dimensional systems numerically we refer to the finite element method developed by Amundsen [63]

end up with the Hamiltonian $H = -\frac{\alpha}{2m}(-p_y \cdot \underline{\sigma}^1 + p_x \cdot \underline{\sigma}^2)$. Looking at this Hamiltonian we notice that it only contains p_y and p_x. Remembering the general definition of SO-coupling in eq.5, the SO-field $\underline{\mathcal{A}}$ therefore can only contain a x and y-component. Furthermore, since the system is so large along the x and y-directions, the Green's function only changes along the z-direction, making the system one dimensional. Hence, constructing our system in such way that the system is invariant in xy-plane, causes the component $\underline{\mathcal{A}}_z = 0$.

The other way to achieve a one-dimensional system with propagation direction along z, is by making it infinitesimal along the x and y-directions. Geometrically, this type of set-up corresponds to a nanowire along the z-direction, surrounded by vacuum at the radial boundaries. In this case, the broken inversion symmetry vector $\mathbf{e}_n$ in eq.6 becomes $\mathbf{e}_n = (\mathbf{e}_x + \mathbf{e}_y)/\sqrt{2}$. Inserting this into eq.6, we obtain the Hamiltonian $H = -\frac{\alpha}{2m}(p_z \cdot \underline{\sigma}^1 - p_z \cdot \underline{\sigma}^2 + (p_y - p_x) \cdot \underline{\sigma}^3)$. Comparing with the general definition in eq.5, we now get a SO-field $\underline{\mathcal{A}}$ with components along all directions. Though utilizing that both the Green's function and its derivative must be zero at the radial boundaries [5], we can neglect p_x and p_y, giving a one dimensional system along the z-direction. Notably, constructing our system in this way we have allowed for a nonzero $\underline{\mathcal{A}}_z$, in contrast to the first method. This leads to a different criteria for generating long-ranged triplet components compared to the thin film case where $\underline{\mathcal{A}}_z$ is zero.

In the above discussion, we have assumed the SO-coupling to be of Rashba-type. Even though the mathematical details in the derivation would differ if we instead had assumed the SO-coupling to be of Dresselhaus-type, the bottom line is still the same. To construct a one-dimensional system along the k-direction (k being x, y or z), we could either make the system finite in the k-direction and translation invariant in the other two directions, leading to $\underline{\mathcal{A}}_k = 0$. Alternatively, we could construct the system in such a way that we still have a finite extent in the k-direction, while the other two directions become infinitesimal, leading to a finite $\underline{\mathcal{A}}_k$. Either way, the gradient in eq.76 simplifies to the partial derivative in the k-direction. In this thesis we will construct our system in the second way, i.e. a nanowire set-up, allowing for a finite $\underline{\mathcal{A}}_k$.

For simplicity, we also assume an ideal system; i.e. no spin-flip scattering. In the following, we will also drop the subscript s, as well as the superscript R, since we only solve for the isotropic s-wave component of the retarded Green's function. Therefore, whenever we refer to $\hat{g}$ in the rest of the thesis we implicitly mean the isotropic s-wave component of the retarded Green's function. In conclusion, the one-dimensional Usadel equation in equilibrium reads

$$iD\tilde{\partial}_k(\hat{g}\tilde{\partial}_k\hat{g}) = [\epsilon\tau^3 \otimes \underline{\sigma}^0 - \hat{\Delta} + \mathbf{h} \cdot \hat{\sigma}, \hat{g}]_-. \tag{77}$$

4.2 KUPRIYANOV–LUKICHEV BOUNDARY CONDITIONS

In the previous section we found an equation describing the Green's function in a general material in equilibrium. Although, to be able to solve the equation for a specific heterostructure, we have to impose some appropriate boundary conditions. For this purpose, we will use the Kupriyanov–Lukichev boundary conditions [64].

Suppose that we have a heterostructure along the k-direction ($k = x, y$ or z), with a material interface at $k = 0$. For simplicity, we assume the interfaces to be not spin-active. Our system can therefore be described by spin-independent boundary conditions. The material to the left of the interface is referred to as the region with $n = 1$, while the material to the right is referred to as

---

[5] The latter follows from the boundary-condition at vacuum-regions, for details see eq.79

the region with $n = 2$. Moreover, the material to the left of the interface has a length L_1, while the material to the right of the interface has a length L_2. For such an interface, we can use the standard spin-independent Kupriyanov–Lukichev boundary conditions [64]. At the material interface, the boundary condition reads

$$\hat{g}_n \tilde{\partial}_k \hat{g}_n = \frac{1}{2} \frac{1}{L_n \xi_n} [\hat{g}_1, \hat{g}_2]_- \equiv \frac{1}{2} \Omega_n [\hat{g}_1, \hat{g}_2]_-. \tag{78}$$

Here $\hat{g}_n$ refers to the Green's function in region n with length L_n. Furthermore, we have introduced the ratio $\xi_n = R_B / R_n$, where R_n is the bulk resistance of the material in region n and R_B is the barrier resistance of the interface. Finally, the notation can be further simplified by defining the interface parameter $\Omega_n = 1/L_n \xi_n$.

At vacuum interfaces, it is reasonable to assume the barrier resistance to become infinitely large, causing the interface parameter Ω_n to drop to zero. At these interfaces, the Kupriyanov–Lukichev boundary condition therefore simplifies to

$$\tilde{\partial}_k \hat{g}_1 \Big|_{-L_1} = 0, \qquad \tilde{\partial}_k \hat{g}_2 \Big|_{L_2} = 0. \tag{79}$$

4.3 BULK SOLUTION

The Usadel equation in eq.77, along with the Kupriyanov–Lukichev boundary conditions, do hold for a general system in equilibrium in which electromagnetic fields, superconducting properties, ferromagnetic properties and SO-coupling all can be present. However, there is one case worth highlighting, namely the bulk superconductor with a phase ϕ_n and magnitude Δ. Without going into detail, one can show that the retarded Green's function in this particular case reads [29, 61]

$$\hat{g}_{\text{bulk}} = \begin{pmatrix} c \cdot \underline{\sigma}^0 & s \cdot i\underline{\sigma}^2 e^{i\phi_n} \\ s \cdot i\underline{\sigma}^2 e^{-i\phi_n} & -c \cdot \underline{\sigma}^0 \end{pmatrix}, \tag{80}$$

where $s = \sinh(\Theta)$ and $c = \cosh(\Theta)$, with $\Theta = \text{atanh}(\Delta/\epsilon)$.

4.4 RICCATI-PARAMETERIZATION

Thus far we have expressed the Green's functions $\hat{g}$ by the normal component $\underline{g}$ and the anomalous part $\underline{f}$. However, this way of expressing $\hat{g}$ gives an infinite range of variation in $\hat{g}$. This infinite range of variation is a big disadvantage in terms of numerical simulations. It would therefore be beneficial to parameterize the Green's function in such a way that we generate a *infinite* range of variation in $\hat{g}$, from a *finite* range of variation in some unknown quantity. Seeking such a parameterization there are two conditions that must be fulfilled, namely the symmetry and normalization of the Green's function $\hat{g}$. One parameterization that fulfills these requirements is the so-called Riccati-parameterization [29, 65]

$$\begin{aligned} \underline{f} &= 2\underline{N}\gamma, & \underline{\tilde{f}} &= 2\underline{\tilde{N}}\tilde{\gamma}, \\ \underline{g} &= \underline{N}(1 + \gamma\tilde{\gamma}), & \underline{\tilde{g}} &= \underline{\tilde{N}}(1 + \tilde{\gamma}\gamma). \end{aligned} \tag{81}$$

Here we have introduced the 2×2 matrices γ and $\tilde{\gamma}$, as well as the matrices $\underline{N} = [1 - \gamma\tilde{\gamma}]^{-1}$ and $\underline{\tilde{N}} = [1 - \tilde{\gamma}\gamma]^{-1}$. Also the tilde conjugate is defined as taking the complex conjugate and letting $\epsilon \to -\epsilon$. Before we proceed we notice that the definition of $\underline{N}$ can be rewritten according to $1 + \underline{N}\gamma\tilde{\gamma} = \underline{N}$. Similarly, for $\underline{\tilde{N}}$ we find $1 + \underline{\tilde{N}}\tilde{\gamma}\gamma = \underline{\tilde{N}}$. In addition, we also have the identities $\underline{N}\gamma = \gamma\underline{\tilde{N}}$ and $\underline{\tilde{N}}\tilde{\gamma} = \tilde{\gamma}\underline{N}$ [29]. These relations will turn out useful later on.

From the definition in eq.81 we immediately notice the numerical advantage of this parameterizatoin. When $\tilde{\gamma} \to 0$ then $\hat{g} \to 1$, and when $\tilde{\gamma} \to 1$ then $\hat{g} \to \infty$. Hence a finite variation in $\tilde{\gamma}$ results in a infinite variation in $\hat{g}$, exactly what we aimed for.

As stated, there are certain properties any parameterization of the Green's function has to fulfill. Let us now verify that the Riccati-parameterization indeed fulfills the required properties. Starting with the symmetry property, we recall that in the quasiclassical approximation we have expressed the Green's function by the Fourier transform with respect to $\mathbf{r}$ and t according to eq.26. Hence, when evaluating quantities such as $\underline{f}(\mathbf{R}, +\epsilon)^*$, the energy dependence simply changes according to $\epsilon \to -\epsilon$ when performing the complex conjugate. However, this is nothing but the definition of the tilde conjugate. The quasiclassical retarded Green's function therefore reads

$$\hat{g} = \begin{pmatrix} \underline{g}(\mathbf{R}, +\epsilon) & \underline{f}(\mathbf{R}, +\epsilon) \\ -\underline{f}(\mathbf{R}, -\epsilon)^* & -\underline{g}(\mathbf{R}, -\epsilon)^* \end{pmatrix}$$
$$= \begin{pmatrix} \underline{g} & \underline{f} \\ -\underline{\tilde{f}} & -\underline{\tilde{g}} \end{pmatrix}. \tag{82}$$

If we now insert the Riccati-parameterization in eq.81, we get the following expression for the retarded Green's function $\hat{g}$

$$\hat{g} = \begin{pmatrix} \underline{N}(1 + \gamma\tilde{\gamma}) & 2\underline{N}\gamma \\ -2\underline{\tilde{N}}\tilde{\gamma} & -\underline{\tilde{N}}(1 + \tilde{\gamma}\gamma) \end{pmatrix}$$
$$= \begin{pmatrix} \underline{N} & 0 \\ 0 & -\underline{\tilde{N}} \end{pmatrix} \begin{pmatrix} 1 + \gamma\tilde{\gamma} & 2\gamma \\ 2\tilde{\gamma} & 1 + \tilde{\gamma}\gamma \end{pmatrix}. \tag{83}$$

Comparing the Riccati-parameterized retarded Green's function above with the general retarded Green's function in eq.82, we see that the Riccati-parameterization indeed fulfills the required symmetry.

It now remains to verify that the Riccati-parameterization fulfills the normalization condition $\hat{g}\hat{g} = 1$. Using the general $\hat{g}$ in eq.82, the normalization condition yields the following equations

$$\underline{g}\underline{g} - \underline{f}\underline{\tilde{f}} = 1, \tag{84}$$
$$\underline{g}\underline{f} - \underline{f}\underline{\tilde{g}} = 0, \tag{85}$$
$$-\underline{\tilde{f}}\underline{g} + \underline{\tilde{g}}\underline{\tilde{f}} = 0, \tag{86}$$
$$-\underline{\tilde{f}}\underline{f} + \underline{\tilde{g}}\underline{\tilde{g}} = 1. \tag{87}$$

Inserting the Riccati-parameterization, it is straightforward to see that the above equations are fulfilled. Hence, the Riccati-parameterization indeed fulfills the the normalization condition $\hat{g}\hat{g} = 1$.

4.4.1 *Parameterized Usadel equation*

Having established a suitable parameterization for the Green's function, namely the Riccati-parameterization, we now focus on rewriting the Usadel equation in eq.77 in terms of this parameterization. Since the equation is a differential equation, we need the derivatives of $\underline{N}$ and $\underline{\tilde{N}}$. By the definition of $\underline{N}$ we get

$$
\begin{aligned}
\partial_k \underline{N} &= \partial_k (1 - \underline{\gamma \tilde{\gamma}})^{-1/2} \\
&= -\frac{1}{(1 - \underline{\gamma \tilde{\gamma}})^2} \partial_k ((1 - \underline{\gamma \tilde{\gamma}})) \\
&= -\frac{1}{(1 - \underline{\gamma \tilde{\gamma}})} [-\underline{\gamma}(\partial_k \tilde{\gamma}) - (\partial_k \underline{\gamma})\tilde{\gamma}] \frac{1}{(1 - \underline{\gamma \tilde{\gamma}})} \\
&= \underline{N}[\underline{\gamma}(\partial_k \tilde{\gamma}) + (\partial_k \underline{\gamma})\tilde{\gamma}]\underline{N}.
\end{aligned}
\tag{88}
$$

Similarly, for $\underline{\tilde{N}}$ we find

$$
\partial_k \underline{\tilde{N}} = \underline{\tilde{N}}[(\partial_k \tilde{\gamma})\underline{\gamma} + \tilde{\gamma}(\partial_k \underline{\gamma})]\underline{\tilde{N}}.
\tag{89}
$$

Let us start by parameterizing the left-hand side of the Usadel equation. Using the definition of the covariant derivative in eq.8 we have

$$
\begin{aligned}
\hat{g}\tilde{\partial}_k \hat{g} &= \hat{g}\partial_k \hat{g} - i\hat{g}[\check{A}_k, \hat{g}]_-, \tag{90} \\
\tilde{\partial}_k(\hat{g}\tilde{\partial}_k \hat{g}) &= \partial_k(\hat{g}\partial_k \hat{g}) - i[\check{A}_k, \hat{g}\partial_k \hat{g}]_- - i\partial_k(\hat{g}[\check{A}_k, \hat{g}]_-) - [\check{A}, \hat{g}[\check{A}, \hat{g}]_-]_- \\
&= \partial_k(\hat{g}\partial_k \hat{g}) - i[\check{A}_k, \hat{g}\partial_k \hat{g}]_- - i\partial_k(\hat{g}\check{A}_k \hat{g} - \hat{g}\hat{g}\check{A}_k) \\
&\quad - [\check{A}, \hat{g}\check{A}\hat{g}]_- + [\check{A}, \hat{g}\hat{g}\check{A}]_-. \tag{91}
\end{aligned}
$$

The last equation can be further simplified by utilizing the fact that the components of $\check{A}$ are constant, i.e. $i\partial_k \check{A}_k = 0$, as well as the normalization condition $\hat{g}\hat{g} = 1$. Hence, we have the following

$$
\tilde{\partial}_k(\hat{g}\tilde{\partial}_k \hat{g}) = \partial_k(\hat{g}\partial_k \hat{g}) - i[\check{A}_k, \hat{g}\partial_k \hat{g}]_- - i\partial_k(\hat{g}\check{A}_k \hat{g}) - [\check{A}, \hat{g}\check{A}\hat{g}]_-.
\tag{92}
$$

The above equation shows all the terms we need to evaluate for the left-hand side of the Usadel equation. We now begin to evaluate each of these terms. However, to avoid getting lost in mathematical manipulation, we will state only the final result and not all intermediate steps. Furthermore, since not all components of $\hat{g}$ are independent, we only need to parameterize the (1,1) and (1,2) components in each term. The equations coming from the (2,1) and (2,2) components can be found simply by taking the tilde conjugate of the equations we find using the (1,1) and (1,2) components.

Starting with $\partial_k \hat{g}$ we find

$$
\partial_k \hat{g}^{(1,1)} = 2\underline{N}[\underline{\gamma}(\partial_k \tilde{\gamma}) + (\partial_k \underline{\gamma})\tilde{\gamma}]\underline{N},
\tag{93}
$$

$$
\partial_k \hat{g}^{(1,2)} = 2\underline{N}\underline{\gamma}(\partial_k \tilde{\gamma})\underline{N}\underline{\gamma} + 2\underline{N}(\partial_k \underline{\gamma})[\tilde{\gamma}\underline{\gamma}\underline{\tilde{N}} + 1].
\tag{94}
$$

After matrix multiplication with $\hat{g}$ this yields the following components for $\hat{g}\partial_k\hat{g}$

$$\hat{g}\partial_k\hat{g}^{(1,1)} = 2\underline{N}[(\partial_k\underline{\gamma})\tilde{\gamma} - \underline{\gamma}(\partial_k\tilde{\gamma})]\underline{N}, \tag{95}$$

$$\hat{g}\partial_k\hat{g}^{(1,2)} = 2\underline{N}[(\partial_k\underline{\gamma}) - \underline{\gamma}(\partial_k\tilde{\gamma})\underline{\gamma}]\tilde{N}. \tag{96}$$

Finally, taking the derivative of $\hat{g}\partial_k\hat{g}$ we get the first term in eq.92, with the following components

$$\partial_k(\hat{g}\partial_k\hat{g})^{(1,1)} = -2\underline{N}\underline{\gamma}[(\partial_k^2\tilde{\gamma}) + 2(\partial_k\tilde{\gamma})\underline{N}\underline{\gamma}(\partial_k\tilde{\gamma})]\underline{N}, \tag{97}$$

$$\partial_k(\hat{g}\partial_k\hat{g})^{(1,2)} = 2\underline{N}[(\partial_k^2\underline{\gamma}) + 2(\partial_k\underline{\gamma})\tilde{\gamma}\underline{N}(\partial_k\underline{\gamma})]\tilde{N}$$
$$- 2\underline{N}\underline{\gamma}[(\partial_k^2\tilde{\gamma}) + 2(\partial_k\tilde{\gamma})\underline{N}\underline{\gamma}(\partial_k\tilde{\gamma})]\underline{\gamma}\tilde{N}. \tag{98}$$

We now proceed to the second term $[\check{\mathcal{A}}_k, \hat{g}\partial_k\hat{g}]_-$. By similar calculations, we find

$$[\check{\mathcal{A}}_k, \hat{g}\partial_k\hat{g}]_-^{(1,1)} = 2\underline{\mathcal{A}}_k\underline{N}[(\partial_k\underline{\gamma})\tilde{\gamma} - \underline{\gamma}(\partial_k\tilde{\gamma})]\underline{N}$$
$$- 2\underline{N}[(\partial_k\underline{\gamma})\tilde{\gamma} - \underline{\gamma}(\partial_k\tilde{\gamma})]\underline{N}\underline{\mathcal{A}}_k(1 - \underline{\gamma}\tilde{\gamma})\underline{N}, \tag{99}$$

$$[\check{\mathcal{A}}_k, \hat{g}\partial_k\hat{g}]_-^{(1,2)} = 2\underline{N}(1 - \underline{\gamma}\tilde{\gamma})\underline{\mathcal{A}}_k\underline{N}[(\partial_k\underline{\gamma}) - \underline{\gamma}(\partial_k\tilde{\gamma})\underline{\gamma}]\tilde{N}$$
$$+ 2\underline{N}[(\partial_k\underline{\gamma}) - \underline{\gamma}(\partial_k\tilde{\gamma})\underline{\gamma}]\tilde{N}\mathcal{A}_k^*(1 - \underline{\gamma}\tilde{\gamma})\tilde{N}. \tag{100}$$

Now, moving on to the third term, calculation yields

$$\partial_k(\hat{g}\check{\mathcal{A}}_k\hat{g})^{(1,1)} = 2\underline{N}[\underline{\gamma}(\partial_k\tilde{\gamma}) + (\partial_k\underline{\gamma})\tilde{\gamma}]\underline{N}\underline{\mathcal{A}}_k(1 + \underline{\gamma}\tilde{\gamma})\underline{N}$$
$$+ 2\underline{N}(1 + \underline{\gamma}\tilde{\gamma})\underline{\mathcal{A}}_k\underline{N}[\underline{\gamma}(\partial_k\tilde{\gamma}) + (\partial_k\underline{\gamma})\tilde{\gamma}]\underline{N}$$
$$+ 4\underline{N}[\underline{\gamma}(\partial_k\tilde{\gamma})\underline{\gamma} + (\partial_k\underline{\gamma})]\tilde{N}\mathcal{A}_k^*\tilde{\gamma}\underline{N}$$
$$+ 4\underline{N}\mathcal{A}_k^*\tilde{N}[(\partial_k\tilde{\gamma}) + \tilde{\gamma}(\partial_k\underline{\gamma})\tilde{\gamma}]\underline{N}, \tag{101}$$

$$\partial_k(\hat{g}\check{\mathcal{A}}_k\hat{g})^{(1,2)} = 4\underline{N}[\underline{\gamma}(\partial_k\tilde{\gamma}) + (\partial_k\underline{\gamma})\tilde{\gamma}]\underline{N}\underline{\mathcal{A}}_k\underline{\gamma}\tilde{N}$$
$$+ 2\underline{N}(1 + \underline{\gamma}\tilde{\gamma})\underline{\mathcal{A}}_k\underline{N}[\underline{\gamma}(\partial_k\tilde{\gamma})\underline{\gamma} + (\partial_k\underline{\gamma})]\tilde{N}$$
$$+ 2\underline{N}[\underline{\gamma}(\partial_k\tilde{\gamma})\underline{\gamma} + (\partial_k\underline{\gamma})]\tilde{N}\mathcal{A}_k^*(1 + \underline{\gamma}\tilde{\gamma})\tilde{N}$$
$$+ 4\underline{N}\underline{\gamma}\mathcal{A}_k^*\tilde{N}[(\partial_k\tilde{\gamma})\underline{\gamma} + \tilde{\gamma}(\partial_k\underline{\gamma})]\tilde{N}. \tag{102}$$

Finally, we calculate the last term $[\check{\mathcal{A}}, \hat{g}\check{\mathcal{A}}\hat{g}]_-$, whose components are

$$[\check{\mathcal{A}}, \hat{g}\check{\mathcal{A}}\hat{g}]_-^{(1,1)} = 4\underline{\mathcal{A}}\underline{N}[\underline{\mathcal{A}} + \underline{\gamma}\mathcal{A}^*\tilde{\gamma}]\underline{N} - 2[\underline{\mathcal{A}}^2, \underline{N}]_-$$
$$- 4\underline{N}[\underline{\mathcal{A}} + \underline{\gamma}\mathcal{A}^*\tilde{\gamma}]\underline{N}\underline{\mathcal{A}}, \tag{103}$$

$$[\check{\mathcal{A}}, \hat{g}\check{\mathcal{A}}\hat{g}]_-^{(1,2)} = 4\underline{\mathcal{A}}\underline{N}[\underline{\mathcal{A}}\underline{\gamma} + \underline{\gamma}\mathcal{A}^*]\tilde{N} + 4\underline{N}[\underline{\mathcal{A}}\underline{\gamma} + \underline{\gamma}\mathcal{A}^*]\tilde{N}\mathcal{A}^*$$
$$- 4\underline{\mathcal{A}}\underline{N}\underline{\gamma}\mathcal{A}^* - 2\underline{\mathcal{A}}\underline{\mathcal{A}}\underline{N}\underline{\gamma} - 2\underline{N}\underline{\gamma}\mathcal{A}^*\mathcal{A}^*. \tag{104}$$

Having found all terms belonging to the left-hand side of eq.77, we now focus on the right-hand side. We notice that it contains the 4×4-matrices $\epsilon\tau^3 \otimes \underline{\sigma}^0$, $\hat{\Delta}$ and $\mathbf{h} \cdot \hat{\sigma}$. On the other hand, the Riccati-paramterization expresses $\hat{g}$ as a 2×2-matrix. Therefore, we need to express

these 4×4-matrices as 2×2-matrices. Since $\underline{\sigma}^0$ is just the identity matrix, the matrix $\epsilon\tau^3 \otimes \underline{\sigma}^0$ simply reduces to $\epsilon\tau^3$ in the 2×2-matrix version. Moreover, from the definition of $\hat{\Delta}$ and $\mathbf{h} \cdot \hat{\sigma}$ we notice that these 4×4-matrices can be expressed as the following 2×2-matrices

$$\hat{\Delta} = \begin{pmatrix} 0 & \Delta i\underline{\sigma}^2 \\ \Delta^* i\underline{\sigma}^2 & 0 \end{pmatrix}, \qquad \mathbf{h} \cdot \hat{\sigma} = \begin{pmatrix} \mathbf{h} \cdot \sigma & 0 \\ 0 & \mathbf{h} \cdot \sigma^* \end{pmatrix}. \tag{105}$$

Altogether, rewriting the Usadel equation in terms of 2×2-matrices we get the following

$$iD\tilde{\partial}_k(\hat{g}\tilde{\partial}_k\hat{g}) = \left[\epsilon\tau^3 - \begin{pmatrix} 0 & \Delta i\underline{\sigma}^2 \\ \Delta^* i\underline{\sigma}^2 & 0 \end{pmatrix} + \begin{pmatrix} \mathbf{h} \cdot \sigma & 0 \\ 0 & \mathbf{h} \cdot \sigma^* \end{pmatrix}, \hat{g}\right]_-. \tag{106}$$

If we now insert the Riccati-parameterization, the terms on the right-hand side reads

$$[\epsilon\tau^3, \hat{g}]_- = \epsilon \begin{pmatrix} 0 & 4\underline{N}\gamma \\ \underline{\tilde{N}}\tilde{\gamma} & 0 \end{pmatrix}, \tag{107}$$

$$\left[\begin{pmatrix} 0 & \Delta i\underline{\sigma}^2 \\ \Delta^* i\underline{\sigma}^2 & 0 \end{pmatrix}, \hat{g}\right]_-$$
$$= \begin{pmatrix} -2(\Delta i\underline{\sigma}^2\underline{\tilde{N}}\tilde{\gamma} + \underline{N}\gamma\Delta^* i\underline{\sigma}^2) & -\Delta i\underline{\sigma}^2\underline{\tilde{N}}(1 + \tilde{\gamma}\gamma) - \underline{N}(1 + \gamma\tilde{\gamma})\Delta i\underline{\sigma}^2 \\ \Delta^* i\underline{\sigma}^2\underline{N}(1 + \gamma\tilde{\gamma}) + \underline{\tilde{N}}(1 + \tilde{\gamma}\gamma)\Delta^* i\underline{\sigma}^2 & 2(\Delta^* i\underline{\sigma}^2\underline{N}\gamma + \underline{\tilde{N}}\tilde{\gamma}\Delta i\underline{\sigma}^2) \end{pmatrix}, \tag{108}$$

$$\left[\begin{pmatrix} \mathbf{h} \cdot \sigma & 0 \\ 0 & \mathbf{h} \cdot \sigma^* \end{pmatrix}, \hat{g}\right]_- = \begin{pmatrix} 0 & 2\mathbf{h} \cdot \sigma\underline{N}\gamma - 2\underline{N}\gamma\mathbf{h} \cdot \sigma^* \\ 2\underline{\tilde{N}}\tilde{\gamma}\mathbf{h} \cdot \sigma - 2\mathbf{h} \cdot \sigma^*\underline{\tilde{N}}\tilde{\gamma} & 0 \end{pmatrix}. \tag{109}$$

We have now parameterized both the left-hand side and the right-hand side of eq.77, giving a fully parameterized Usadel equation in eq.106. That is, we have managed to rewrite the Usadel equation into a 2×2-matrix equation, whose (1,1) and (1,2)-components describe the system. The equations are still quite complicated to solve though. After all, the (1,1) and (1,2)-components of the parameterized Usadel equation give rise to two coupled second-order differential equations, both including $\partial_k^2\tilde{\gamma}$ and $\partial_k^2\gamma$. Luckily we can isolate $\partial_k^2\gamma$ by considering the following trick. Multiplying the equation for $\tilde{\partial}_k(\hat{g}\tilde{\partial}_k\hat{g})^{(1,1)}$ with $\underline{N}^{-1}\gamma\underline{\tilde{N}}$ from the right, we get an equation for $\partial_k^2\underline{\tilde{\gamma}}$ which is present in both components (see eq.97 and eq.98). If we now insert our newfound equation for $\partial_k^2\tilde{\gamma}$ into $\tilde{\partial}_k(\hat{g}\tilde{\partial}_k\hat{g})^{(1,2)}$, all terms involving $\partial_k^2\tilde{\gamma}$ and $\partial_k\tilde{\gamma}$ will cancel, giving an equation only including $\partial_k^2\gamma$. Executing the described procedure, we arrive at the equation

$$\begin{aligned} iD2\underline{N}&[(\partial_k^2\underline{\gamma}) + 2(\partial_k\underline{\gamma})\tilde{\gamma}\underline{N}(\partial_k\underline{\gamma})] \\ &= iD\Big\{4i\underline{N}[(\partial_k\underline{\gamma})\underline{\tilde{N}}(\tilde{\gamma}\underline{\mathcal{A}_k}\underline{\gamma} + \underline{\mathcal{A}_k^*}) + (\underline{\mathcal{A}_k} + \underline{\gamma}\underline{\mathcal{A}_k^*}\tilde{\gamma})\underline{N}(\partial_k\underline{\gamma})] \\ &\quad + 2\underline{N}[\underline{\mathcal{A}}\underline{\mathcal{A}}\underline{\gamma} - \underline{\gamma}\underline{\mathcal{A}^*}\underline{\mathcal{A}^*}] \\ &\quad + 4\underline{N}(\underline{\mathcal{A}}\underline{\gamma}\gamma\underline{\mathcal{A}^*})\underline{\tilde{N}}(\tilde{\gamma}\underline{\mathcal{A}}\underline{\gamma} + \underline{\mathcal{A}^*})\Big\} \\ &\quad + 2\underline{N}i(\gamma\Delta^*\underline{\sigma}^2\gamma - \Delta\underline{\sigma}) + 4\underline{N}\gamma\epsilon + 2\mathbf{h} \cdot \sigma\underline{N}\gamma - 2\underline{N}\gamma\mathbf{h} \cdot \sigma^*. \end{aligned} \tag{110}$$

The above equation can be simplified further by multiplying by $-i\underline{N}^{-1}/2$ from the left[6]

$$
\begin{aligned}
D[(\partial_k^2\underline{\gamma}) &+ 2(\partial_k\underline{\gamma})\tilde{\underline{\gamma}}\underline{N}(\partial_k\underline{\gamma})] \\
&= 2iD\big[(\partial_k\underline{\gamma})\tilde{\underline{N}}(\tilde{\underline{\gamma}}\underline{\mathcal{A}}_k\underline{\gamma} + \underline{\mathcal{A}}_k^*) + (\underline{\mathcal{A}}_k + \underline{\gamma}\underline{\mathcal{A}}_k^*\tilde{\underline{\gamma}})\underline{N}(\partial_k\underline{\gamma})\big] \\
&+ D\big[\underline{\mathcal{A}}\underline{\mathcal{A}}\underline{\gamma} - \underline{\gamma}\underline{\mathcal{A}}^*\underline{\mathcal{A}}^*\big] \\
&+ 2D(\underline{\mathcal{A}}\underline{\gamma} + \underline{\gamma}\underline{\mathcal{A}}^*)\tilde{\underline{N}}(\tilde{\underline{\gamma}}\underline{\mathcal{A}}\underline{\gamma} + \underline{\mathcal{A}}^*) \\
&+ (\underline{\gamma}\Delta^*\underline{\sigma}^2\underline{\gamma} - \Delta\underline{\sigma}^2) - 2i\underline{\gamma}\epsilon - i\mathbf{h}\cdot(\sigma\underline{\gamma} - \underline{\gamma}\sigma^*).
\end{aligned}
\tag{111}
$$

We have now finally arrived at an equation for the 2×2-matrix $\underline{\gamma}$. The equation for $\tilde{\underline{\gamma}}$ is found by simply taking the tilde conjugate of the above equation.

4.4.2 *Parameterized Kupriyanov–Lukichev boundary conditions*

In the previous section, we expressed the Usadel equation in terms of $\underline{\gamma}$ and $\tilde{\underline{\gamma}}$ for a region n. It now remains to Riccati-parameterize the Kupriyanov–Lukichev boundary conditions. Let us first focus on the boundary condition at the material interface, as defined in eq.78. Using the definition of the covariant derivative in eq.8, with only components along the k-direction, the Kupriyanov–Lukichev boundary condition reads

$$
\hat{g}_n\partial_k\hat{g}_n = \frac{1}{2}\Omega_n[\hat{g}_1,\hat{g}_2]_- + i\hat{g}_n[\check{\mathcal{A}}_k,\hat{g}_n]_-.
\tag{112}
$$

Looking at the above equation, we first notice that the left-hand side has already been calculated in eq.95 and eq.96. Thus, only the right-hand side remains to be considered.

Utilizing the definition of the Riccati-parameterization in eq.81 with the appropriate subscripts, the first term $[\hat{g}_1,\hat{g}_2]_-$ yields

$$
[\hat{g}_1,\hat{g}_2]_-^{(1,1)} = \frac{1}{2}\Omega_n\big[4\underline{N}_1(1 - \underline{\gamma}_1\tilde{\underline{\gamma}}_2)\underline{N}_2 - 4\underline{N}_2(1 - \underline{\gamma}_2\tilde{\underline{\gamma}}_1)\big]\underline{N}_1,
\tag{113}
$$

$$
[\hat{g}_1,\hat{g}_2]_-^{(1,2)} = \frac{1}{2}\Omega_n\big[4\underline{N}_1(1 - \underline{\gamma}_1\tilde{\underline{\gamma}}_2)\underline{\gamma}_2\tilde{\underline{N}}_2 - 4\underline{N}_2(1 - \underline{\gamma}_2\tilde{\underline{\gamma}}_1)\underline{\gamma}_1\tilde{\underline{N}}_1\big].
\tag{114}
$$

Similarly, for $\hat{g}_n[\check{\mathcal{A}}_k,\hat{g}_n]_-$ we find

$$
\begin{aligned}
\hat{g}_n[\check{\mathcal{A}}_k,\hat{g}_n]_-^{(1,1)} &= 4\underline{N}_n[\underline{\mathcal{A}}_k + \underline{\gamma}_n\underline{\mathcal{A}}_k^*\tilde{\underline{\gamma}}_n]\underline{N}_n - 2\underline{N}_n(1 - \underline{\gamma}_n\tilde{\underline{\gamma}}_n)\underline{\mathcal{A}}_k\underline{N}_n \\
&\quad - 2\underline{N}_n\underline{\mathcal{A}}_k(1 - \underline{\gamma}_n\tilde{\underline{\gamma}}_n)\underline{N}_n,
\end{aligned}
\tag{115}
$$

$$
\hat{g}_n[\check{\mathcal{A}}_k,\hat{g}_n]_-^{(1,2)} = 2\underline{N}_n(1 + \underline{\gamma}_n\tilde{\underline{\gamma}}_n)\underline{\mathcal{A}}_k\underline{\gamma}_n\tilde{\underline{N}}_n + 2\underline{N}_n\underline{\gamma}_n\underline{\mathcal{A}}_k^*(1 + \tilde{\underline{\gamma}}_n\underline{\gamma}_n)\tilde{\underline{N}}_n.
\tag{116}
$$

Altogether, the Kupriyanov–Lukichev boundary condition in eq.112 gives rise to the following equations for the (1,1) and (1,2)-components

---

6 $\mathbf{h}\cdot\sigma$ is a scalar, so we are allowed to interchange the order of $\mathbf{h}\cdot\sigma$ and $\underline{N}$

$$\begin{aligned}
\underline{N}_n[(\partial_k\underline{\gamma}_n)\underline{\tilde{\gamma}}_n - \underline{\gamma}_n(\partial_k\underline{\tilde{\gamma}}_n)]\underline{N}_n &= \Omega_n[\underline{N}_1(1 - \underline{\gamma}_1\underline{\tilde{\gamma}}_2)\underline{N}_2 - \underline{N}_2(1 - \underline{\gamma}_2\underline{\tilde{\gamma}}_1)]\underline{N}_1 \\
&\quad + 2i\underline{N}_n[\underline{A}_k + \underline{\gamma}_n\underline{A}_k^*\underline{\tilde{\gamma}}_n]\underline{N}_n \\
&\quad - i\underline{N}_n(1 - \underline{\gamma}_n\underline{\tilde{\gamma}}_n)\underline{A}_k\underline{N}_n \\
&\quad - i\underline{N}_n\underline{A}_k(1 - \underline{\gamma}_n\underline{\tilde{\gamma}}_n)\underline{N}_n,
\end{aligned} \tag{117}$$

$$\begin{aligned}
\underline{N}_n[(\partial_k\underline{\gamma}_n) - \underline{\gamma}_n(\partial_k\underline{\tilde{\gamma}}_n)\underline{\gamma}_n]\tilde{N}_n &= \Omega_n[\underline{N}_1(1 - \underline{\gamma}_1\underline{\tilde{\gamma}}_2)\underline{\gamma}_2\tilde{N}_2 - \underline{N}_2(1 - \underline{\gamma}_2\underline{\tilde{\gamma}}_1)\underline{\gamma}_1\tilde{N}_1] \\
&\quad + i\underline{N}_n(1 + \underline{\gamma}_n\underline{\tilde{\gamma}}_n)\underline{A}_k\underline{\gamma}_n\tilde{N}_n \\
&\quad + i\underline{N}_n\underline{\gamma}_n\underline{A}_k^*(1 + \underline{\tilde{\gamma}}_n\underline{\gamma}_n)\tilde{N}_n.
\end{aligned} \tag{118}$$

Looking at the two equations above, we notice that we can isolate $\partial_k\underline{\gamma}_n$ by doing a similar procedure as earlier when discussing the Usadel equation. If we multiply the first equation with $\underline{N}_n^{-1}\underline{\gamma}_n\tilde{N}_n$ from the right, thereafter subtract the resulting equation from the second equation, we have managed to isolate $\partial_k\underline{\gamma}_n$. Performing the described procedure, the equation for $\partial_k\underline{\gamma}_n$ reads

$$\begin{aligned}
\underline{N}_n(\partial_k\underline{\gamma}_n) &= \Omega_n\underline{N}_1(1 - \underline{\gamma}_1\underline{\tilde{\gamma}}_2)\underline{N}_2(\underline{\gamma}_2 - \underline{\gamma}_n) \\
&\quad + \Omega_n\underline{N}_2(1 - \underline{\gamma}_2\underline{\tilde{\gamma}}_1)\underline{N}_1(\underline{\gamma}_n - \underline{\gamma}_1) \\
&\quad + i\underline{N}_n\underline{\gamma}_n\underline{A}_k^* + i\underline{N}_n\underline{A}_k\underline{\gamma}_n.
\end{aligned} \tag{119}$$

The equation above holds for a general region n, in which $n = 1$ refers to the left region while $n = 2$ refers to the right region. If we now insert for $n = 1$ we notice that the second term in eq.119 vanishes, enabling us to divide with $\underline{N}_1^{-1}$ from the left. Similarly, inserting for $n = 2$ the first term in eq.119 vanishes, enabling us to divide with $\underline{N}_2^{-1}$ from the left. Thus, the equations for $n = 1$ and $n = 2$ simplify to

$$\partial_k\underline{\gamma}_1 = \Omega_1(1 - \underline{\gamma}_1\underline{\tilde{\gamma}}_2)\underline{N}_2(\underline{\gamma}_2 - \underline{\gamma}_1) + i\underline{\gamma}_1\underline{A}_k^* + i\underline{A}_k\underline{\gamma}_1, \tag{120}$$

$$\partial_k\underline{\gamma}_2 = \Omega_2(1 - \underline{\gamma}_2\underline{\tilde{\gamma}}_1)\underline{N}_1(\underline{\gamma}_2 - \underline{\gamma}_1) + i\underline{\gamma}_2\underline{A}_k^* + i\underline{A}_k\underline{\gamma}_2. \tag{121}$$

Now that we have Riccati-parameterized the boundary condition at the material interface, it is straight-forward to parameterize the vacuum interfaces. Recalling the expression for $\partial_k\hat{g}_n$ found in eq.93 and eq.94, and doing the same mathematical procedure as above, the boundary conditions at the vacuum interfaces in eq.79 simply becomes

$$\partial_k\underline{\gamma}_1\Big|_{-L_1} = i\underline{\gamma}_1\underline{A}_k^* + i\underline{A}_k\underline{\gamma}_1, \qquad \partial_k\underline{\gamma}_2\Big|_{L_2} = i\underline{\gamma}_2\underline{A}_k^* + i\underline{A}_k\underline{\gamma}_2. \tag{122}$$

As before, the equations for $\underline{\tilde{\gamma}}_1$ and $\underline{\tilde{\gamma}}_2$ are found by taking the tilde conjugate of eq,120, eq.121 and eq.122.

4.4.3 *The bulk solution in the Riccati-parameterization*

Having expressed the Usadel equation, as well as the appropriate boundary conditions in terms of the Riccati-parameterization, it is useful to relate the well-known bulk solution in eq.80 to this parameterization. Looking at the general definition of the Riccati-parameterization in eq.83, we notice the elements of the retarded Green's function are products of $\underline{\gamma}$ and $\underline{\tilde{\gamma}}$, making it

hard to read-out expressions for γ and $\tilde{\gamma}$ by direct comparison. Fortunately, we notice that we can express $\underline{\gamma}$ and $\underline{\tilde{\gamma}}$ in terms of the matrix elements of eq.83, e.g. $\underline{\gamma} = 2\underline{N}\gamma/(1 + \underline{N}(1 + \gamma\tilde{\gamma}))$. Comparing these matrix elements with the bulk solution in eq.80, we find the following expressions for $\underline{\gamma}$ and $\underline{\tilde{\gamma}}$ in a bulk superconductor

$$\underline{\gamma} = s \cdot i\underline{\sigma}^2 e^{i\phi_n}/(1 + c \cdot \underline{\sigma}^0), \qquad \underline{\tilde{\gamma}} = -s \cdot i\underline{\sigma}^2 e^{-i\phi_n}/(1 + c \cdot \underline{\sigma}^0). \tag{123}$$

Here ϕ_n is the phase of the superconductor in region n and 1 is the 2×2 identity matrix. Moreover, recall that $s = \sinh(\Theta)$, $c = \cosh(\Theta)$ and $\Theta = \mathrm{atanh}(\Delta/\epsilon)$, as defined previously.

4.4.4   *Summary*

We started out this chapter by wanting to find the equations that describe spin and charge transport in general heterostructures. Seeking such equations led to the well-known Usadel equation in the diffusive limit, accompanied by the Kupriyanov–Lukichev boundary conditions. Expressing the Green's function $\hat{g}$ in terms of the Riccati-parameterization, we were able to rewrite the equations in a more suitable manner for numerical simulations. Before we proceed, let us summarize the main results of what we have found so far.

Accompanied by the Kupriyanov–Lukichev boundary conditions, the Green's function $\underline{\gamma}_n$ in region n is determined by the equation

$$
\begin{aligned}
&D[(\partial_k^2 \underline{\gamma}_n) + 2(\partial_k \underline{\gamma}_n)\underline{\tilde{\gamma}}_n \underline{N}_n (\partial_k \underline{\gamma}_n)] \\
&= 2iD[(\partial_k \underline{\gamma}_n)\tilde{N}_n(\underline{\tilde{\gamma}}_n \underline{\mathcal{A}}_k \underline{\gamma}_n + \underline{\mathcal{A}}_k^*) + (\underline{\mathcal{A}}_k + \underline{\gamma}_n \underline{\mathcal{A}}_k^* \underline{\tilde{\gamma}}_n)\underline{N}_n(\partial_k \underline{\gamma}_n)] \\
&+ D[\underline{\mathcal{A}}\underline{\mathcal{A}}\underline{\gamma}_n - \underline{\gamma}_n \underline{\mathcal{A}}^* \underline{\mathcal{A}}^*] \\
&+ 2D(\underline{\mathcal{A}}\underline{\gamma}_n + \underline{\gamma}_n \underline{\mathcal{A}}^*)\tilde{N}_n(\underline{\tilde{\gamma}}_n \underline{\mathcal{A}}\underline{\gamma}_n + \underline{\mathcal{A}}^*) \\
&+ (\underline{\gamma}_n \Delta^* \underline{\sigma}^2 \underline{\gamma}_n - \Delta \underline{\sigma}^2) - 2i\underline{\gamma}_n \epsilon - i\mathbf{h} \cdot (\sigma \underline{\gamma}_n - \underline{\gamma}_n \sigma^*).
\end{aligned}
\tag{124}
$$

At material interfaces these boundary conditions read

$$\partial_k \underline{\gamma}_1 = \Omega_1(1 - \underline{\gamma}_1 \underline{\tilde{\gamma}}_2)\underline{N}_2(\underline{\gamma}_2 - \underline{\gamma}_1) + i\underline{\gamma}_1 \underline{\mathcal{A}}_k^* + i\underline{\mathcal{A}}_k \underline{\gamma}_1, \tag{125}$$

$$\partial_k \underline{\gamma}_2 = \Omega_2(1 - \underline{\gamma}_2 \underline{\tilde{\gamma}}_1)\underline{N}_1(\underline{\gamma}_2 - \underline{\gamma}_1) + i\underline{\gamma}_2 \underline{\mathcal{A}}_k^* + i\underline{\mathcal{A}}_k \underline{\gamma}_2. \tag{126}$$

Here $n = 1$ denotes the region to the left of the interface and $n = 2$ denotes the region to the right.

In the special case of having a vacuum-region adjacent to a material, the boundary conditions simplify according to

$$\partial_k \underline{\gamma}_1\Big|_{-L_1} = i\underline{\gamma}_1 \underline{\mathcal{A}}_k^* + i\underline{\mathcal{A}}_k \underline{\gamma}_1, \qquad \partial_k \underline{\gamma}_2\Big|_{L_2} = i\underline{\gamma}_2 \underline{\mathcal{A}}_k^* + i\underline{\mathcal{A}}_k \underline{\gamma}_2, \tag{127}$$

where L_1 and L_2 denote the position of the vacuum interface.

As emphasized earlier, by taking the tilde conjugate of the relevant boundary conditions, we obtain the boundary condition for $\underline{\tilde{\gamma}}_n$.

D-VECTOR FORMALISM AND PHYSICAL OBSERVABLES

In the previous chapters, we have developed a solid understanding of the underlying physics governing superconducting systems. We have introduced the fundamental concepts, as well as established the mathematical framework needed to describe Cooper-pairs. We also derived the equations determining the Green's function in a general system. In this chapter, we will connect what we have learned so far by expressing common physical quantities in terms of the Green's function. We start by introducing the d-vector formalism, which will be useful when discussing physical quantities. Then, we will express the current, density of states and superconducting gap, respectively, in terms of the Green's function.

5.1 D-VECTOR FORMALISM

Thus far, we have expressed the Green's function by its normal component $\underline{g}$ and anomalous component $\underline{f}$. To better see the interplay between the singlet and triplet components, we introduce the d-vector formalism [66]

$$\underline{f} = (f_s + \mathbf{d} \cdot \boldsymbol{\sigma})i\underline{\sigma}^2. \tag{128}$$

Here f_s is the singlet component, which is a scalar quantity, i.e. rotationally invariant, and $\mathbf{d} = (d_x, d_y, d_z)$ is the triplet component, which is a Cartesian vector.

Alternatively, we can also express the matrix $\underline{\gamma}$ in terms of the d-vector formalism, giving

$$2\underline{N}\underline{\gamma} = \begin{pmatrix} id_y - d_x & d_z + f_s \\ d_z - f_s & id_y + d_x \end{pmatrix}. \tag{129}$$

Before we proceed, let us get some intuition about the triplet component. If we have an exchange field $\mathbf{h}$ pointing in the $\mathbf{e}_h$ direction, we know that the triplet component can be either a long-ranged triplet component (LRTC) or a short-range triplet component (SRTC), depending on how the spins of the Cooper-pair are oriented with respect to the direction of the exchange field $\mathbf{h}$. Having spins parallel to the direction of the exchange field the Cooper-pair is defined as an LRTC, whereas spins perpendicular to the exchange field produce an SRTC. Naively, one might think that the LRTC is the one with $\mathbf{d} \| \mathbf{h}$ and the SRTC is the one with $\mathbf{d} \perp \mathbf{h}$. However, looking at the definition of $\underline{f}^R$ in eq.128, we notice that $\mathbf{d}$ is multiplied by $\underline{\sigma}^2$. In a two-dimensional plane, this matrix represents nothing than a $\theta = \pi/2$-rotation. Thus, if we start out with a triplet component $\mathbf{d} \| \mathbf{h}$, the triplet component becomes rotated by an angle $= \pi/2$ and consequently ends up being perpendicular to $\mathbf{h}$. Therefore, the SRTC is defined as $d_\| = \mathbf{d} \cdot \mathbf{e}_h$, while the LRTC is defined as $d_\perp = |\mathbf{d} \times \mathbf{e}_h|$.

5.2   DENSITY OF STATES

The local density of states for particles with spin σ and energy ϵ at position z is defined by the following [67]

$$N_\sigma(\epsilon, z) = N_0 \text{Re}\{g_{\sigma\sigma}(\epsilon, z)\}. \tag{130}$$

Here N_0 is the local density of states per spin at the Fermi level when the material is in its normal state[1].

The definition as it stands is spin-dependent. In materials where the exchange field is not too strong, it is sufficient to describe the system by a spin-independent local density of states $N = (N_\uparrow + N_\downarrow)/2$. For convenience, we will focus on the normalized local density of states $D = N/N_0$. Therefore, the equation for the normalized spin-independent local density of states becomes

$$D(\epsilon, z) = \frac{1}{2}\text{ReTr}\{\underline{g}(\epsilon, z)\}. \tag{131}$$

Expressing the Green's function by the Ricatti-parameterization, the density of states becomes

$$D(\epsilon, z) = \frac{1}{2}\text{ReTr}\{\underline{N}(1 + \underline{\gamma}\tilde{\gamma})\}. \tag{132}$$

Although the density of states defined above is a local quantity, we will often refer to it as $D(\epsilon)$ without specifying the position. In such a case, the position is taken to be in the middle of the material of interest.

5.2.1   *Density of states in the weak proximity limit*

Before we proceed, let us consider how the weak proximity effect affects the density of states in a non-superconducting material. Remembering that the bulk of a non-superconducting material is characterized by $\underline{g}_0 = 1$ and $\underline{f}_0 = 0$, we can write the retarded Green's function of the non-superconducting material in the weak proximity limit as a correction to the bulk case

$$\hat{g} = \hat{g}_0 + \hat{f} + \hat{g}_2. \tag{133}$$

where $\hat{g}_0 = \text{diag}(1, -1)$ is the solution for the bulk of a non-superconducting material, $\hat{f}$ is the first order correction and $\hat{g}_2$ is the second order correction.

Using the normalization condition $\hat{g}^2 = 1$, we get the following equation

$$(\hat{g}_0\hat{f} + \hat{f}\hat{g}_0) + (\hat{g}_0\hat{g}_2 + \hat{g}_2\hat{g}_0) + \hat{f}^2 + (\hat{g}_2\hat{f} + \hat{f}\hat{g}_2) + \hat{g}_2^2 = 0. \tag{134}$$

Neglecting terms higher than second order, the two last terms drop out. Also, demanding the first and second-order terms to separately fulfill the equation, we are left with two equations

$$(\hat{g}_0\hat{f} + \hat{f}\hat{g}_0) = 0, \tag{135}$$

$$(\hat{g}_0\hat{g}_2 + \hat{g}_2\hat{g}_0) + \hat{f}^2 = 0. \tag{136}$$

---

[1] Although N_0 in general depends on the energy ϵ, it is fair to treat N_0 as a constant value measured at the Fermi level when using the quasiclassical approximation.

Recalling that $\hat{g}_0$ is diagonal, we see from the first-order equation that $\hat{f}$ must be antidiagonal. From the general structure of the retarded Green's function in eq.30 we can write

$$\hat{f} = \begin{pmatrix} 0 & f \\ -\underline{f}^* & 0 \end{pmatrix}. \tag{137}$$

Or, equivalently, using the tilde conjugate

$$\hat{f} = \begin{pmatrix} 0 & f \\ -\tilde{\underline{f}} & 0 \end{pmatrix}. \tag{138}$$

Calculating $\hat{f}^2$ and inserting this into the second-order equation yields

$$0 = \begin{pmatrix} 1 & 0 \\ 0 & -1 \end{pmatrix} \hat{g}_2 + \hat{g}_2 \begin{pmatrix} 1 & 0 \\ 0 & -1 \end{pmatrix} + \begin{pmatrix} -f\tilde{\underline{f}} & 0 \\ 0 & -\tilde{\underline{f}}f \end{pmatrix}. \tag{139}$$

The only way for the above equation to hold is by having $\hat{g}_2$ diagonal. Again, using the general structure of the retarded Green's function we have

$$\hat{g}_2 = \begin{pmatrix} g & 0 \\ 0 & -\underline{g} \end{pmatrix}. \tag{140}$$

Solving for g in the second-order equation, we then find $g = \frac{1}{2}f\tilde{\underline{f}}$. Going back to the total retarded Green's function, we have now found

$$\hat{g} = \begin{pmatrix} 1 & 0 \\ 0 & -1 \end{pmatrix} + \begin{pmatrix} 0 & f \\ -\tilde{\underline{f}} & 0 \end{pmatrix} + \begin{pmatrix} g & 0 \\ 0 & -\underline{g} \end{pmatrix}$$

$$= \begin{pmatrix} 1 & 0 \\ 0 & -1 \end{pmatrix} + \begin{pmatrix} 0 & f \\ -\tilde{\underline{f}} & 0 \end{pmatrix} + \begin{pmatrix} \frac{1}{2}f\tilde{\underline{f}} & 0 \\ 0 & -\frac{1}{2}\tilde{\underline{f}}f \end{pmatrix}. \tag{141}$$

We are now finally ready to express the linearized density of states. Recalling the general definition of the density of states in eq.131, we simply get

$$D(\epsilon, z) = \frac{1}{2}\mathrm{ReTr}\left\{1 + \frac{1}{2}f\tilde{\underline{f}}\right\}. \tag{142}$$

The above expression for the linearized density of states is written in terms of the anomalous Green's function $\underline{f}$. Equivalently, we can also express the density of states in the d-vector formalism, where the expression for zero energy becomes[2]

$$D(\epsilon = 0) = 1 + \frac{1}{2}|\mathbf{d}|^2 - \frac{1}{2}|f_s|^2 \tag{143}$$

---

[2] Choosing to evaluate the density of states at zero energy, the tilde conjugate simply becomes the complex conjugate.

The expression above shows an important feature of the density of states. From the linearized expression, we clearly see that having triplet components **d** present results in an enhancement of the density of states, while the singlet part f_s reduces the density of states. In the case of a normal metal, where both the singlet and triplet parts are zero, the density of states is featureless with a constant value of 1. On the other hand, if we have an s-wave superconductor, the singlet part has a finite value while the triplet parts are zero, resulting in a gap in the density of states at $\epsilon = 0$. We can therefore determine if the system is dominated by singlet or triplet parts by measuring the density of states. A peak around $\epsilon = 0$ corresponds to a system dominated by the triplet component, while a gap corresponds to a system dominated by the singlet component.

5.3   CURRENT

We now move on to discuss the current in terms of the Green's functions. The dimensionless transport equation for the system can be written as

$$i\tilde{\partial}_z(\check{g}\tilde{\partial}_z\check{g}) - [H, \check{g}]_- = 0. \tag{144}$$

Using the relation $[\check{g}, H]_- = i\partial_t\check{g}$, and multiplying both sides with the constant electrical conductivity σ, we get the following equation

$$i\tilde{\partial}_z(\sigma\check{g}\tilde{\partial}_z\check{g}) + i\partial_t\check{g} = 0. \tag{145}$$

If we now define the current density matrix as $\check{\mathbf{j}} = \rho\mathbf{v} = \sigma\check{g}\tilde{\partial}_z\check{g}$ [27, 68], meaning that $\rho = \sigma\check{g}$, the above equation can be written as

$$\tilde{\partial}_z\check{\mathbf{j}} + \partial_t\rho = 0. \tag{146}$$

This is nothing but the continuity equation in one dimension, telling that our definition of the current density matrix indeed conserves the current matrix as it should.

Let us now take a closer look at our definition of the current density matrix. Remembering the matrix structure of the Green's function $\check{g}$ in eq.29, it is reasonable to expect the current density matrix $\check{\mathbf{j}}$ to have the same matrix structure. Hence, we do have

$$\check{\mathbf{j}} = \begin{pmatrix} \hat{\mathbf{j}}^R & \hat{\mathbf{j}}^K \\ 0 & \hat{\mathbf{j}}^A \end{pmatrix}. \tag{147}$$

However, as the equation stands, it is a matrix equation. To get expressions for e.g. charge- and spincurrent density, we have to rewrite the current density matrix into expressions for the scalar current densities.

Let us first look at the charge current density. As a general expression for the charge current density should be able to account for both the equilibrium and nonequilibrium-cases, we have to use the Keldysh component. Furthermore, the upper diagonal element of the Keldysh component represents electrons with a charge $-e$, while the lower diagonal element represents holes with a charge $+e$. To account for this sign difference in the charge, we therefore multiply the Keldysh component by $\hat{\rho}^3$, and then take the trace. Moreover, we are interested in all energies, so we integrate over the quasiparticle energy ϵ. To normalize the expression, we divide by a factor of $2 \cdot 2e^2$. The first factor comes from the trace, while the second factor appears as a result of the integration over quasiparticle energies with charge $2e^2$. Finally, to

obtain the charge current density we multiply by a factor of e. Doing the above steps, the charge current density reads

$$j_e = \frac{1}{4e} \int d\epsilon \, \mathrm{Tr}\{\hat{\rho}^3 \hat{\mathbf{j}}^K\}. \tag{148}$$

Moving on to the spin current density [30, 27], we follow a similar procedure as outlined for the charge current density. The only difference is that we now have to extract the spin information from $\hat{\mathbf{j}}^K$. We do so by multiplying $\hat{\mathbf{j}}^K$ by the a matrix containing the Pauli vector along unit vector $\mathbf{e_n}$, $\hat{\sigma}_\mathbf{n} = \mathrm{diag}(\mathbf{e_n} \cdot \sigma, \mathbf{e_n} \cdot \sigma^*)$. Therefore $\hat{\rho}^3 \hat{\mathbf{j}}^K$ in the charge current density modifies to $\hat{\rho}^3 \hat{\sigma}_\mathbf{n} \hat{\mathbf{j}}^K$ in the case of spin current density. Besides, due to the two possible values for spin, we divide the normalization factor by an extra factor of 2. Finally, being interested in the spin current density we do not multiply with a factor of e at the end. The resulting expression for spin-current density polarized along unit vector $\mathbf{e_n}$ becomes

$$j_{S,\mathbf{n}} = \frac{1}{8e^2} \int d\epsilon \, \mathrm{Tr}\{\hat{\rho}^3 \hat{\sigma}_\mathbf{n} \hat{\mathbf{j}}^K\}. \tag{149}$$

In the above, we have expressed the current density by the Green's function. To obtain an expression for the current itself, we only need to multiply $\check{\mathbf{j}}$ by the cross-sectional area A. In that case, the electrical conductivity transforms into $\sigma A = (\sigma A L)/L = GL$ where L is the length of the system and G is the conductance. Hence, the definition of the current matrix in terms of the Green's function becomes

$$\check{\mathbf{I}} = GL\check{g}\tilde{\partial}_z\check{g}. \tag{150}$$

Since the current $\check{\mathbf{I}}$ has the same matrix structure as $\check{\mathbf{j}}$, the charge and spin currents in eq.148 and eq.149 simply modifies to

$$I_e = \frac{1}{4e} \int d\epsilon \, \mathrm{Tr}\{\hat{\rho}^3 \hat{\mathbf{I}}^K\}, \tag{151}$$

$$I_{S,\mathbf{n}} = \frac{1}{8e^2} \int d\epsilon \, \mathrm{Tr}\{\hat{\rho}^3 \hat{\sigma}_\mathbf{n} \hat{\mathbf{I}}^K\}. \tag{152}$$

As we have seen earlier, the triplet state has one long-ranged component (LRTC) and one short-ranged component (SRTC). Therefore, it is useful to decompose the spincurrent $I_{S,\mathbf{n}}$ above into a spincurrent for each of these components. Recalling that the LRTC is defined as having spins parallel to the exchange field, we extract the LRTC from eq.152 by choosing a unit vector $\mathbf{e_n}$ parallel to exchange field $\mathbf{h}$. Whereas for the SRTC, whose spins are perpendicular to the exchange field, we choose a unit vector $\mathbf{e_n}$ perpendicular to the exchange field $\mathbf{h}$[3]. The singlet spin current will always be zero due to the fact that this state has a spin quantum number equal to zero.

Before we proceed, let us take a closer look at the magnitude of the spincurrent to get a better understanding of the origin of the two polarization components. The spin-expectation vector of a triplet Cooper-pair is defined as $\langle \mathbf{S} \rangle = i\mathbf{d} \times \tilde{\mathbf{d}}$, where $\mathbf{d} = \mathbf{d}_{\mathrm{LRTC}} + \mathbf{d}_{\mathrm{SRTC}}$ is the (total) triplet component in the d-vector formalism and $\tilde{\mathbf{d}} = \mathbf{d}(-\epsilon)^*$[27, 30]. Writing out the spin expectation vector of the total proximity-induced superconducting state, we obtain

---

[3] Note that this is just the general definitions of the LRTC and SRTC.

$$\langle \mathbf{S} \rangle_{\text{tot}} = i(\mathbf{d}_{\text{LRTC}} + \mathbf{d}_{\text{SRTC}}) \times (\tilde{\mathbf{d}}_{\text{LRTC}} + \tilde{\mathbf{d}}_{\text{SRTC}})$$
$$= \langle \mathbf{S} \rangle_{\text{LRTC}} + \langle \mathbf{S} \rangle_{\text{SRTC}} + i(\mathbf{d}_{\text{LRTC}} \times \tilde{\mathbf{d}}_{\text{SRTC}} + \tilde{\mathbf{d}}_{\text{LRTC}} \times \mathbf{d}_{\text{SRTC}}). \tag{153}$$

From the above, we see that the spin expectation vector of the total proximity-induced superconducting state $\langle \mathbf{S} \rangle_{\text{tot}}$ splits into three parts: two terms entirely due to the LRTC and SRTC, $\langle \mathbf{S} \rangle_{\text{LRTC}}$ and $\langle \mathbf{S} \rangle_{\text{SRTC}}$ respectively, and one interference term between the LRTC and STRC $\langle \mathbf{S} \rangle_{\text{int}} = i(\mathbf{d}_{\text{LRTC}} \times \tilde{\mathbf{d}}_{\text{SRTC}} + \tilde{\mathbf{d}}_{\text{LRTC}} \times \mathbf{d}_{\text{SRTC}})$. To unravel the physical meaning of the different terms, let us choose a pure Rashba SO-coupling and an exchange field in the yz-plane $\mathbf{h} = h_y \mathbf{e}_y + h_z \mathbf{e}_z$. This choice produces

$$\mathbf{d}_{\text{LRTC}} = (g_1, -g_2 h_z/h, g_2 h_y/h), \qquad \mathbf{d}_{\text{SRTC}} = (0, d_{\text{SRTC}} h_y, d_{\text{SRTC}} h_z)/h. \tag{154}$$

where g_1, g_2 and d_{SRTC} are complex scalars that describe the LRTC and SRTC respectively. Also note that when $\mathbf{d}_{\text{SRTC}} || \mathbf{h}$ then $\mathbf{d}_{\text{LRTC}} \cdot \mathbf{h} = 0$ as expected[4].

We first focus on the two terms entirely due to the SRTC and LRTC. Inserting the specific form of the triplet components, we obtain

$$\langle \mathbf{S} \rangle_{\text{SRTC}} = i\mathbf{d}_{\text{SRTC}} \times \tilde{\mathbf{d}}_{\text{SRTC}}$$
$$= i(d_{\text{SRTC}} \cdot \tilde{d}_{\text{SRTC}} h_y h_z - d_{\text{SRTC}} \cdot \tilde{d}_{\text{SRTC}} h_z h_y)/h^2$$
$$= 0, \tag{155}$$
$$\langle \mathbf{S} \rangle_{\text{LRTC}} = i\mathbf{d}_{\text{LRTC}} \times \tilde{\mathbf{d}}_{\text{LRTC}}$$
$$= -i(\tilde{g}_2 \cdot g_1 - g_2 \cdot \tilde{g}_1)(h_y \mathbf{e}_y + h_z \mathbf{e}_z)/h. \tag{156}$$

From the above, we notice that the term entirely due to the SRTC vanishes, while the term entirely due to the LRTC is nonzero and points along $\mathbf{h}$. In other words, the spin-expectation vector of the LRTC points along $\mathbf{h}$ as expected.

Let us now take a closer look at the interference term. Suppose the interference term can written as $\langle \mathbf{S} \rangle_{\text{int}} = \langle \mathbf{S} \rangle_{\text{ex}} + \langle \mathbf{S} \rangle_{\text{mix}}$, where the exchange term $\langle \mathbf{S} \rangle_{\text{ex}}$ and mixing term $\langle \mathbf{S} \rangle_{\text{mix}}$ jet to be determined. Inserting the specific expressions for the two triplet components, the interference term now reads

$$\langle \mathbf{S} \rangle_{\text{int}} = i(\mathbf{d}_{\text{LRTC}} \times \tilde{\mathbf{d}}_{\text{SRTC}} + \tilde{\mathbf{d}}_{\text{LRTC}} \times \mathbf{d}_{\text{SRTC}})$$
$$= -i(\tilde{d}_{\text{SRTC}} g_2 - d_{\text{SRTC}} \tilde{g}_2)\mathbf{e}_x - i(\tilde{d}_{\text{SRTC}} g_1 - d_{\text{SRTC}} \tilde{g}_1)(\mathbf{e}_y h_z - \mathbf{e}_z h_y)/h$$
$$\equiv \langle \mathbf{S} \rangle_{\text{ex}} + \langle \mathbf{S} \rangle_{\text{mix}}. \tag{157}$$

From the above, we immediately notice that the exchange term $\langle \mathbf{S} \rangle_{\text{ex}}$ is independent of the direction of the exchange field $\mathbf{h}$, whereas the polarization direction of the mixing term changes as the direction of $\mathbf{h}$ changes. Although both terms are perpendicular to the exchange field $\mathbf{h}$.

Going back to the spincurrent in eq.152, we can now discuss the two polarization components. The only spin-expectation value parallel with $\mathbf{h}$ is the term originating entirely from the LRTC, i.e. $\langle \mathbf{S} \rangle_{\text{LRTC}}$. In other words, $\langle \mathbf{S} \rangle_{\text{LRTC}}$ is the only term that contributes to the parallel component of the critical spincurrent $\mathrm{I}^C_{S,||}$. If we instead now focus on the perpendicular component of

---

4 This is nothing but the definition of the LRTC and SRTC in the d-vector formalism.

the critical spincurrent $I_{S,\perp}^C$, we know that there are two spin-expectation values pointing perpendicular to $\mathbf{h}$, namely $\langle \mathbf{S} \rangle_{ex}$ and $\langle \mathbf{S} \rangle_{mix}$. Consequently, the magnitude of the perpendicular component of the critical spincurrent $I_{S,\perp}^C$ can be decomposed as

$$|I_{S,\perp}^C| = \sqrt{(I_{S,ex}^C)^2 + (I_{S,mix}^C)^2}. \tag{158}$$

The two contributions $I_{S,ex}^C$ and $I_{S,mix}^C$, as well as the magnitude of the parallel component of the critical spin-current $I_{S,||}^C$, were presented in [30], which we show in figure 10. From the figure we notice that while the mixing term qualitatively has the same behaviour as the parallel component, i.e. a sinusoidal form vanishing at $\phi = 0$ and $\phi = \pi$, the exchange term is finite even at $\phi = 0$ where no net charge flows. Hence, the exchange term can be interpreted as a superconductivity-induced torque acting on the magnetization, which is present even in the absence of any charge current. On the other hand, the mixing term represents the spin polarization that originates from interference between the LRTC and SRTC carried by the charge current, while the parallel component originates from pure LRTC carried by the charge current. The mixing term and parallel component therefore has qualitatively the same behaviour as the charge current, i.e. sinusoidal behaviour, which we clearly see in figure 10.
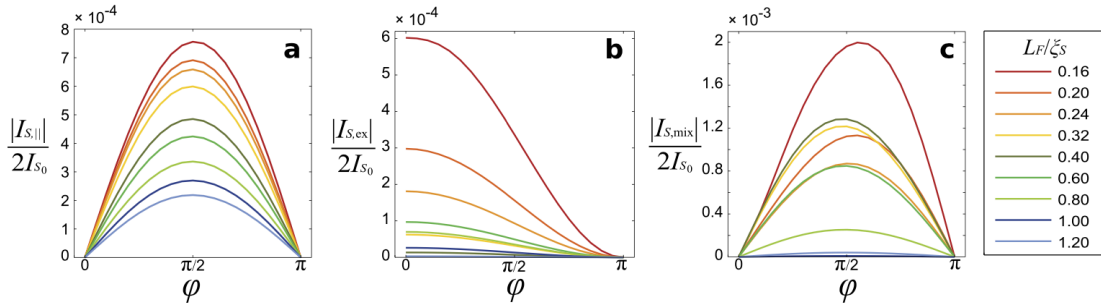
Figure 10: The different polarization components of the normalized critical current for a S/N/F/N/S-Josephson junction plotted as a function of the phase difference φ between the superconductors. The length of the ferromagnet is denoted L_F, while a superconducting coherence length of $\xi_S = 25$ nm is used. Note that in our notation we have reserved φ to the azimuthal angle, using ϕ instead to denote the phase difference. Moreover, I_{S_0} in the figure is just a normalization constant comparable to the prefactor in eq.150. Figure is taken from [30].

5.4 THE GAP-EQUATION

We finally complete this section by expressing the superconducting gap by the Green's function. Our starting point is the general definition [61]

$$\Delta(\mathbf{r}_1) = \lambda \langle \Psi_\downarrow(\mathbf{r}_1, t_1) \Psi_\uparrow(\mathbf{r}_1, t_1) \rangle. \tag{159}$$

Looking at the definition of the anomalous Keldysh Green's function $F_{\sigma\sigma'}^K(\mathbf{r}_1, t_1; \mathbf{r}_1, t_1)$ in eq.19 and using the fermionic anticommutation relation, we notice that we can express the expectation value above in two different ways

$$F_{\downarrow\uparrow}^{K}(\mathbf{r_1}, t_1; \mathbf{r_1}, t_1) = -i\langle[\Psi_\downarrow(\mathbf{r_1}, t_1), \Psi_\uparrow(\mathbf{r_1}, t_1)]_-\rangle$$
$$= -i\langle(\Psi_\downarrow(\mathbf{r_1}, t_1)\Psi_\uparrow(\mathbf{r_1}, t_1) - \Psi_\uparrow(\mathbf{r_1}, t_1)\Psi_\downarrow(\mathbf{r_1}, t_1))\rangle$$
$$= -2i\langle(\Psi_\downarrow(\mathbf{r_1}, t_1)\Psi_\uparrow(\mathbf{r_1}, t_1))\rangle, \tag{160}$$
$$F_{\uparrow\downarrow}^{K}(\mathbf{r_1}, t_1; \mathbf{r_1}, t_1) = -i\langle[\Psi_\uparrow(\mathbf{r_1}, t_1), \Psi_\downarrow(\mathbf{r_1}, t_1)]_-\rangle$$
$$= -i\langle(\Psi_\uparrow(\mathbf{r_1}, t_1)\Psi_\downarrow(\mathbf{r_1}, t_1) - \Psi_\downarrow(\mathbf{r_1}, t_1)\Psi_\uparrow(\mathbf{r_1}, t_1))\rangle$$
$$= +2i\langle(\Psi_\downarrow(\mathbf{r_1}, t_1)\Psi_\uparrow(\mathbf{r_1}, t_1))\rangle. \tag{161}$$

Hence, the superconducting gap can be expressed as

$$\Delta(\mathbf{r_1}) = -i\frac{\lambda}{4}\left(F_{\uparrow\downarrow}^{K}(\mathbf{r_1}, t_1; \mathbf{r_1}, t_1) - F_{\downarrow\uparrow}^{K}(\mathbf{r_1}, t_1; \mathbf{r_1}, t_1)\right). \tag{162}$$

Looking at the above equation, we notice that the first term is nothing but the (1,4)-element of the 4×4-matrix $\hat{G}^{K}$, while the second term corresponds to the (2,3)-element. These elements can be extracted from $\hat{G}^{K}$ by doing the following

$$F_{\uparrow\downarrow}^{K}(\mathbf{r_1}, t_1; \mathbf{r_1}, t_1) - F_{\downarrow\uparrow}^{K}(\mathbf{r_1}, t_1; \mathbf{r_1}, t_1) = \text{Tr}\left\{\frac{1}{2}(\hat{\rho}^1 - i\hat{\rho}^2)\hat{\rho}^3\hat{G}^{K}\right\}, \tag{163}$$

giving the following expression for the superconducting gap

$$\Delta(\mathbf{r_1}) = -i\frac{\lambda}{4}\text{Tr}\left\{\frac{1}{2}(\hat{\rho}^1 - i\hat{\rho}^2)\hat{\rho}^3\hat{G}^{K}\right\}. \tag{164}$$

The above expression can be further rewritten by taking the quasiclassical approximation as defined in eq.26 and eq.28, along with a general rewriting of the momentum integral[5]

$$\Delta(\mathbf{r_1}) = -i\frac{\lambda}{4}\text{Tr}\left\{\frac{1}{2}(\hat{\rho}^1 - i\hat{\rho}^2)\hat{\rho}^3\hat{G}^{K}(\mathbf{r_1}, t_1; \mathbf{r_1}, t_1)\right\}$$
$$= -i\frac{\lambda}{4}\text{Tr}\left\{\frac{1}{2}(\hat{\rho}^1 - i\hat{\rho}^2)\hat{\rho}^3\frac{1}{(2\pi)^4}\lim_{\substack{r\to 0 \\ t\to 0}}\int d\mathbf{p}\,e^{+i\mathbf{r}\cdot\mathbf{p}}\int d\epsilon\,e^{-i\epsilon t}\hat{G}^{K}(\mathbf{R}, T; \mathbf{p}, \epsilon)\right\}$$
$$= -i\frac{\lambda}{4}\text{Tr}\left\{\frac{1}{2}(\hat{\rho}^1 - i\hat{\rho}^2)\hat{\rho}^3\frac{N_0}{2\pi}\int d\epsilon\int\frac{d\mathbf{e}_{p_F}}{4\pi}\frac{\pi}{i}\hat{g}^{K}(\mathbf{R}, T; \mathbf{e}_{p_F}, \epsilon)\right\}. \tag{165}$$

Finally, we can approximate the Green's function to first order in spherical harmonics as shown in eq.70. The integration over the direction of the momentum at the Fermi-surface $\int d\mathbf{e}_{p_F}$ therefore vanishes, resulting in the so-called gap equation

$$\Delta(\mathbf{R}) = -\frac{1}{8}N_0\lambda\text{Tr}\left\{\frac{1}{2}(\hat{\rho}^1 - i\hat{\rho}^2)\hat{\rho}^3\int d\epsilon\,\hat{g}^{K}(\mathbf{R}, T, \epsilon)\right\} \tag{166}$$

---

[5] $\int\frac{d\mathbf{p}}{(2\pi^3)} \to N_0\int d\xi_{\mathbf{p}}\frac{d\mathbf{e}_F}{(4\pi)}$, where N_0 is the density of states at the Fermi-energy.

LINEARIZED EQUATIONS

In Chapter 4 we set up the machinery for describing general heterostructures. However, looking at eq.124 we notice that it is still a nonlinear equation in terms of $\underline{\gamma}_n$ and $\partial_k \underline{\gamma}_n$. To gain some physical insight into what to expect, we will in this chapter linearize the Usadel equation and insert the relevant parameters for a particular system. The system of our choice will be an S/F/S-Josephson junction, where we are interested in describing the Green's function in the ferromagnetic region. To avoid being overwhelmed by equations, we will choose our system to lie in the z-direction. For this specific system we will insert the relevant form of SO-coupling, invoke the d-vector formalism, and finally discuss our choice of the exchange field **h**. The qualitative discussion of a corresponding S/F/S-Josephson junction laying in the x or y-direction will indeed be qualitatively similar, with only minor differences in terms of subscripts.

6.1 USADEL EQUATION IN THE WEAK PROXIMITY LIMIT

Mathematically, the equations for $\underline{\gamma}_n$ and $\underline{\tilde{\gamma}}_n$ are linearized by imposing the weak proximity limit. Recall that the weak proximity limit means that we assume the properties of the superconductor to have a small (but finite) impact on the ferromagnet close to the interface. Therefore, the weak proximity limit is defined as $\underline{g} \simeq 1$ and $|\underline{f}| << 1$ in the ferromagnet. In terms of the Riccati-parameterization, this reads

$$\underline{N}_n \simeq 1, \qquad \underline{\gamma}_n << 1. \tag{167}$$

Inserting the definition above into eq.124, as well as only keeping first-order terms of $\partial_k \underline{\gamma}_n$ and $\underline{\gamma}_n$, we obtain the following linearized Usadel equation for propagation along the z-direction

$$\begin{aligned}
D(\partial_z^2 \underline{\gamma}_n) &= 2iD[(\partial_z \underline{\gamma}_n)\underline{\mathcal{A}}_z^* + \underline{\mathcal{A}}_z(\partial_z \underline{\gamma}_n)] \\
&\quad + D[\underline{\mathcal{A}}\underline{\mathcal{A}}\underline{\gamma}_n + \underline{\gamma}_n \underline{\mathcal{A}}^* \underline{\mathcal{A}}^* + 2\underline{\mathcal{A}}\underline{\gamma}_n \underline{\mathcal{A}}^*] \\
&\quad - 2i\underline{\gamma}_n \epsilon - i\mathbf{h} \cdot (\sigma \underline{\gamma}_n - \underline{\gamma}_n \sigma^*).
\end{aligned} \tag{168}$$

Here, we have chosen a general exchange field $\mathbf{h} = h_x \mathbf{e}_x + h_y \mathbf{e}_y + h_z \mathbf{e}_z$. Moreover, as emphasized earlier, the linearized equation for $\underline{\tilde{\gamma}}_n$ can be found from the equation above by taking the tilde conjugate.

6.2   USADEL EQUATION WITH D-VECTOR FORMALISM

As a first step to more clearly see the interplay between the singlet and triplet components, we now invoke the d-vector formalism in the linearized Usadel equation as written in eq.168. In the weak proximity limit, the d-vector formalism in eq.129 reads

$$\underline{\gamma} = \frac{1}{2} \begin{pmatrix} i\mathrm{d}_y - \mathrm{d}_x & \mathrm{d}_z + \mathrm{f_s} \\ \mathrm{d}_z - \mathrm{f_s} & i\mathrm{d}_y + \mathrm{d}_x \end{pmatrix}. \tag{169}$$

Furthermore, as we derived in section 2.1, a nanowire setup along the z-direction results in a Rashba SO-coupling $\underline{A}_R = (0, 0, \alpha(\underline{\sigma}^1 - \underline{\sigma}^2))$. Choosing our material in such a way that we can neglect the Dresselhaus contribution, the SO-field is purely of Rashba type. In addition, it is worth noticing that our particular choice of SO-field fulfills

$$\underline{A}\underline{A} = \underline{A}_z\underline{A}_z = 2\alpha \begin{pmatrix} 1 & 0 \\ 0 & 1 \end{pmatrix} = \underline{A}_z^*\underline{A}_z^* = \underline{A}^*\underline{A}^*, \tag{170}$$

which simplifies the two first terms in the second row in eq.168.

Altogether, inserting the d-vector formalism and the specific form of SO-coupling into eq.168, we end up with a 2×2-matrix equation that has a structure similar to the definition of the d-vector in eq. 169. Isolating the different components is simply a matter of adding or subtracting the desired matrix elements. Doing so results in the following equations

$$\frac{i}{2}D\partial_z^2\mathrm{d}_x = 2iD\alpha\partial_z\mathrm{d}_z + 2iD\alpha^2(\mathrm{d}_x + \mathrm{d}_y) + \epsilon\mathrm{d}_x + \mathrm{h}_x\mathrm{f_s}, \tag{171}$$

$$\frac{i}{2}D\partial_z^2\mathrm{d}_y = 2iD\alpha\partial_z\mathrm{d}_z + 2iD\alpha^2(\mathrm{d}_x + \mathrm{d}_y) + \epsilon\mathrm{d}_y + \mathrm{h}_y\mathrm{f_s}, \tag{172}$$

$$\frac{i}{2}D\partial_z^2\mathrm{d}_z = -2iD\alpha\partial_z(\mathrm{d}_x + \mathrm{d}_y) + 4iD\alpha^2\mathrm{d}_z + \epsilon\mathrm{d}_z + \mathrm{h}_z\mathrm{f_s}, \tag{173}$$

$$\frac{i}{2}D\partial_z^2\mathrm{f_s} = \epsilon\mathrm{f_s} + \mathbf{h} \cdot \mathbf{d}. \tag{174}$$

6.3   CHOICE OF EXCHANGE FIELD

Inserting the d-vector formalism, we were able to more clearly see the interplay between the different components of the d-vector. However, we still cannot easily see the interplay between the SRTC $\mathrm{d}_{||}$ and LRTC $\mathrm{d}_\perp$. For this purpose, we will now discuss and specify the exchange-field $\mathbf{h}$.

Having a finite component $\underline{A}_z$, we recall that the criterion for generating LRTC is a nonzero commutator $[\underline{A}, \mathbf{h} \cdot \sigma]_-$. Calculating the commutator, it is straightforward to show that both an exchange field in e.g. the xy and yz-plane produce a nonzero commutator (with some exceptions for the former case). Let us choose an exchange field in the yz-plane as sketched in figure 11.
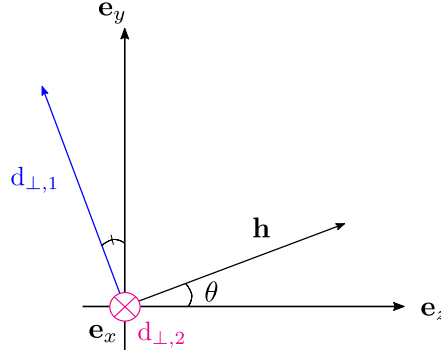
Figure 11: Illustration of how the long-ranged and short-ranged triplet components in the d-vector formalism relates to an exchange field $\mathbf{h}$ in the yz-plane. The SRTC lies parallel to $\mathbf{h}$, while the two LRTC $d_{\perp,1}$ (blue) and $d_{\perp,2}$ (pink) lies perpendicular to $\mathbf{h}$.

Having an exchange field in the yz-plane, we can write $\mathbf{h} = h(\sin(\theta)\mathbf{e}_y + \cos(\theta)\mathbf{e}_z) = h\mathbf{e}_h$, as illustrated in figure 11. Thus, the SRTC $d_{||}$ becomes $d_{||} = \mathbf{d} \cdot \mathbf{e}_h = d_y\sin(\theta) + d_z\cos(\theta)$. To find the LRTC $d_\perp$ we can use a geometric approach. From the definition of $d_\perp = |\mathbf{d} \times \mathbf{e}_h|$ we know that this component must be perpendicular to $\mathbf{e}_h$. Instead of calculating the cross-product directly, we can find the unit vector perpendicular to $\mathbf{e}_h$, let us call this $\mathbf{e}_{h,\perp}$, and then find $d_\perp$ by taking the dot product with $\mathbf{e}_{h,\perp}$. From figure 11 we see that there are two options for $\mathbf{e}_{h,\perp}$, the vector has to lie either in the yz-plane or entirely along the x-axis. In the following, we will refer to the perpendicular component generated from $\mathbf{e}_{h,\perp}$ lying in the yz-plane as $d_{\perp,1} = d_\perp$, while the other case is referred to as simply $d_{\perp,2} = d_x$. Looking at figure 11 we see that $d_\perp = -d_z\sin(\theta) + d_y\cos(\theta)$, while $d_x = d_x$. We stress that both $d_\perp$ and d_x are defined as LRTC. Finally, we notice that we can rewrite d_y and d_z in terms of $d_{||}$ and $d_\perp$. In summary, the equations we have to disposal are as follows

$$d_{||} = d_y\sin(\theta) + d_z\cos(\theta), \tag{175}$$

$$d_\perp = -d_z\sin(\theta) + d_y\cos(\theta), \tag{176}$$

$$d_y = d_{||}\sin(\theta) + d_\perp\cos(\theta), \tag{177}$$

$$d_z = d_{||}\cos(\theta) - d_\perp\sin(\theta). \tag{178}$$

Inserting the above set of equations into eq.171 - eq.174, we find the following equations for the system

$$\begin{aligned}
\frac{i}{2}D\partial_z^2 d_x &= 2iD\alpha\partial_z d_{||}\cos(\theta) - 2iD\alpha\partial_z d_\perp\sin(\theta) \\
&\quad + 2iD\alpha^2 d_{||}\sin(\theta) + 2iD\alpha^2 d_\perp\cos(\theta) \\
&\quad + [\epsilon + 2iD\alpha^2]d_x,
\end{aligned} \tag{179}$$

$$\begin{aligned}
\frac{i}{2}D\partial_z^2 d_{||} &= -2iD\alpha\partial_z d_\perp - 2iD\alpha\partial_z d_x\cos(\theta) \\
&\quad + 2iD\alpha^2 d_x\sin(\theta) - iD\alpha^2 d_\perp\sin(2\theta) \\
&\quad + [\epsilon + 2iD\alpha^2(1 + \cos^2(\theta))]d_{||} + hf_s,
\end{aligned} \tag{180}$$

$$\frac{i}{2}D\partial_z^2 \mathbf{d}_\perp = 2iD\alpha\partial_z \mathbf{d}_x \sin(\theta) + 2iD\alpha\partial_z \mathbf{d}_{||}$$
$$+ 2iD\alpha^2 \mathbf{d}_x \cos(\theta) - iD\alpha^2 \mathbf{d}_{||}\sin(2\theta) \qquad (181)$$
$$+ [\epsilon + 2iD\alpha^2(1 + \sin^2(\theta))]\mathbf{d}_\perp,$$

$$\frac{i}{2}D\partial_z^2 \mathbf{f}_s = \epsilon\mathbf{f}_s + h\mathbf{d}_{||}. \qquad (182)$$

Looking at the above set of equations, we clearly see the effect of having a ferromagnet with SO-coupling in contact with a superconductor. When the Cooper-pairs enter the ferromagnet, these are all in a singlet state. Hence, the only nonzero component is f_s. However, according to eq.182, having an exchange field present in the ferromagnet generates an SRTC. When the SRTC is generated, the presence of SO-coupling can then generate LRTC according to eq.180.

It is also worth emphasizing that even though a nonzero commutator is the criterion for generating LRTC, this quantity alone does not tell the whole story. The reason is that the commutator does not tell us anything about which choice of **h** generates the triplet components that are most easily seen in experiments. To illustrate this, suppose that we have two different **h** fields, both giving a nonzero commutator. However, when inserting these particular choices into the linearized equations, we find that in one of the cases the ratio between the imaginary part of the quasiparticle energies at zero-energy, $\mathrm{Im}\{\epsilon_\perp(0)\}/\mathrm{Im}\{\epsilon_{||}(0)\}$, goes to zero while in the other case it diverges. Hence, in the former case we have $\mathrm{Im}\{\epsilon_\perp(0)\} \ll \mathrm{Im}\{\epsilon_{||}(0)\}$, while in the latter case we have $\mathrm{Im}\{\epsilon_\perp(0)\} \gg \mathrm{Im}\{\epsilon_{||}(0)\}$. As a large imaginary energy part tends to destabilize and destroy Cooper-pairs, this can be seen directly from eq.26, Cooper-pairs with a large imaginary part are also harder to see experimentally. Therefore, when the ratio $\mathrm{Im}\{\epsilon_\perp(0)\}/\mathrm{Im}\{\epsilon_{||}(0)\} \to 0$ the LRTC is more energetically favorable than the SRTC. In contrast, if the ratio $\mathrm{Im}\{\epsilon_\perp(0)\}/\mathrm{Im}\{\epsilon_{||}(0)\} \to \infty$, it is SRTC that is the most energetically favourable. This will of course drastically affect for which choice of **h** we will most easily measure the triplet component. After all, it does not really help to generate a triplet component if this state is also so energetically unfavorable and unstable that it becomes hard to measure.

Although, the ratio $\mathrm{Im}\{\epsilon_\perp(0)\}/\mathrm{Im}\{\epsilon_{||}(0)\}$ in general will affect for which orientations of the exchange field we expect to most easily see the LRTC, we notice from eq.179 - eq.182 that for a exchange field in the yz-plane the ratio reads $\mathrm{Im}\{\epsilon_\perp(0)\}/\mathrm{Im}\{\epsilon_{||}(0)\} = (1 + \sin^2(\theta))/(1 + \cos^2(\theta))$. This varies only between a minimum value $1/2$ and a maximum value 2. Thus, in our particular case, we do not expect the stability between the LRTC and SRTC to matter. Although we notify that this ratio may become important in other cases.

6.4 DIMENSIONLESS EQUATIONS

Finally, for numerical simulations, it is useful to find a dimensionless analogue of eq.179 - eq.182. We do so simply by introducing the Thouless energy $\epsilon_T = D/L^2$ and the dimensionless position $z' = z/L$. Using these definitions, it is straight forward to rewrite eq.179 - eq.182 into a dimensionless form. For qualitative discussions, making the equations dimensionless do not matter, the physics remains the same. However, doing numerical simulations it is convenient to make the equations dimensionless to simply reduce the number of parameters. In the numerical simulations presented in this thesis, we therefore use the dimensionless equations rather than the dimensionfull equations as stated in the previous section.

THE BASIC BUILDING BLOCK: S/F/S-JOSEPHSON JUNCTION

In previous chapters, we have presented the underlying theory and derived the equations describing general heterostructures. We have also linearized the equations for a system with Rashba SO-coupling and exchange field in the yz-plane, to better understand the underlying physics. However, the systems in mind are still rather general. We have not said anything about the specific strength of the Rashba SO-coupling, the specific orientation of the exchange field or the geometry of the set-up. In this chapter, we will discuss the S/F/S-Josephson junction with SO-coupling and phase difference ϕ investigated by Jacobsen and Linder [1], the very building block for the more complicated H-geometry.

7.1 EXPERIMENTAL SET-UP

The physical system of interest is shown in figure 12. The trilayer consists of two s-wave superconductors, with phases ϕ_L and ϕ_R. Thus, the phase difference reads $\phi = \phi_L - \phi_R$. The two superconductors have the same magnitude Δ. Furthermore, we scale all energies and exchange fields to Δ. The two superconductors are then connected by a ferromagnetic nanowire of length L along the z-axis. We choose the left interface to be at a position $z = 0$, which means that the ferromagnetic nanowire goes from $z = 0$ to $z = L$. We assume a pure Rashba SO-coupling $\underline{\mathcal{A}} = \underline{\mathcal{A}}_R = (0, 0, \alpha(\underline{\varrho}^1 - \underline{\varrho}^2))$ in the ferromagnetic wire, as derived in section 2.1. Finally, we have chosen an exchange field in the yz-plane $\mathbf{h} = h(\sin(\theta)\mathbf{e}_y + \cos(\theta)\mathbf{e}_z) = h\mathbf{e}_h$, with θ governing the proportion of in- and out-of-plane components of the field.
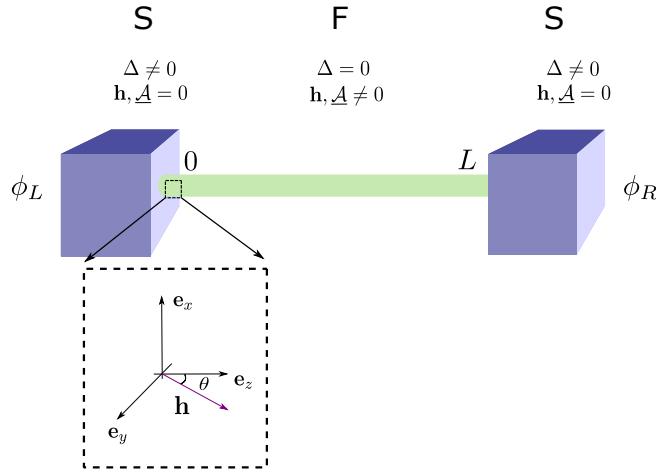

Figure 12: A sketch of the experimental set-up. Two superconductors S with phase ϕ_L and ϕ_R are connected by a ferromagnetic nanowire F. The ferromagnet has a length L, an exchange field $\mathbf{h}$ and a SO-field $\underline{\mathcal{A}}$.

7.2   NUMERICAL METHOD

In this section, we will summarize the most important key-points from the numerical method used to solve our system. For more details see the main-file attached in Appendix C.

The numerical method goes as follows. For the first energy, we calculate the bulk solution in the two superconductors according to eq.123, which enters the boundary conditions. Next, we set the initial guess for our solution. Whether the bulk solution in the superconductors or the normal metal solution (i.e. $\underline{\gamma} = \underline{\tilde{\gamma}} = 0$) is most suitable depends on the parameters for which we solve. If we expect the density of states to resemble the behavior seen in a normal metal, we use the normal metal solution $\underline{\gamma} = \underline{\tilde{\gamma}} = 0$ as an initial guess. If instead we expect the solution in the superconductor to be a better fit for the density of states, the bulk solution in the superconductor tends to be the most numerically stable[1]. In our case, choosing $\underline{\gamma} = \underline{\tilde{\gamma}} = 0$ as our initial guess in the ferromagnet tends to be the most numerically stable. We emphasize that this initial guess is used only for the first energy which we solve for. Next, we solve the differential equation eq.124, with the Kupriyanov–Lukichev boundary conditions in eq.125 and eq.126, by using the bvp6c-matlab solver implemented by Hale and Moore [69]. As stated at the end of the previous chapter, for numerical convenience, we will use the dimensionless analogue of these equations. Having found the solution of $\underline{\gamma}$ and $\underline{\tilde{\gamma}}$ for a given energy, we use this solution as an initial guess for the next energy. By doing so, we improve numerical efficiency and stability. The above procedure is repeated until all energies are iterated through. If we also iterate through different choices of phases, we update the initial guess for all energies and positions with the current solution before moving on to the next phase.

There are some remarks about the numerical method described above worth highlighting. When we iterate through the energies, it is beneficial to start with the highest energy. Starting with the highest energy, our first initial guess (which is the normal metal solution in our case) will be a better guess for the correct solution. Thus, starting with the highest energy improves the numerical efficiency and stability. As the density of states rapidly falls off for energies much larger than the superconducting gap, it is sufficient to set the highest energy to 1.3Δ. For numerical convergence, it is also beneficial to add a small imaginary part to the energy, which models the inelastic scattering. For simplicity, we will choose the Fermi-level $\mu = 0$, in which the density of states becomes symmetric with respect to energy. Therefore, it is sufficient to only solve for positive energies. With these choices around $200 - 300$ energy points are sufficient for the bvp6c-matlab solver.

Finally, we emphasize that we assume a bulk solution in the superconducting region, thus not solving the system fully self-consistently. This is a valid assumption as long as we choose the interface parameter between the superconductor and the ferromagnet to be small. For small values of the interface parameter, i.e. small transparency across the interface, the effect of the ferromagnet on the superconductor is minimal, thus we can assume a constant solution in the superconductor equal to the solution of the bulk.

---

[1] Although we should be able to solve our equations numerically regardless of our initial guess, choosing an initial guess not too far away from the correct solution will improve the numerical efficiency and stability. If we choose a really bad initial guess, the numerical solver may not converge to a solution.

7.3 RESULTS

In figure 13a we have plotted the density of states for a field along the y-axis, $\mathbf{h} = 10\Delta \mathbf{e}_y$, and a pure Rashba spin-orbit coupling of strength $\alpha = 0.4/L$, where $L = 15$ nm is the length of the ferromagnet. In the same figure, we have also shown the results for an S/N/S and S/F/S junction without SO-coupling. From this figure we clearly see that the density of states is strongly enhanced at a phase difference $\phi = \phi_L - \phi_R = \pi$, giving what the authors call the giant proximity effect. As we know from section 5.2.1 the density of states in the limit of weak proximity can be used to determine if we have singlet or triplet states present. Triplet states result in a peak in the density of states whereas the singlet state produces a gap. Therefore, the peak in the density of states at $\phi = \pi$ tells us that the system is dominated by triplet components. Moreover, as we will see, the peak is entirely due to the triplet states, here the LRTC.
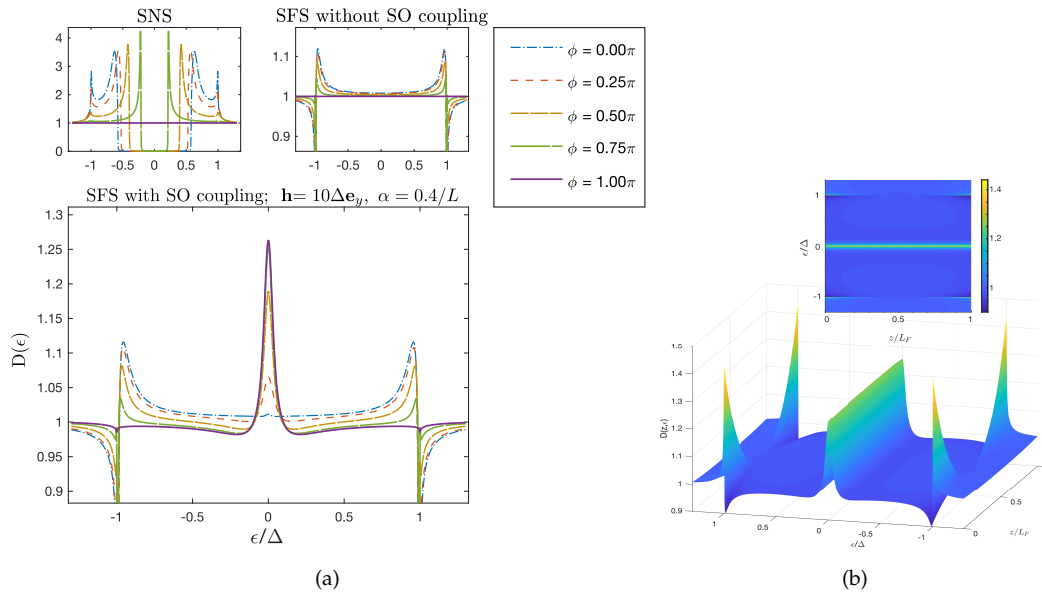

Figure 13: Reproduction of result first presented in [1]. Figure (a) shows the density of states $D(\epsilon)$ for a S/F/S-Josephson junction with phase difference ϕ. In the ferromagnet an exchange filed $\mathbf{h} = 10\Delta\mathbf{e}_y$ is chosen and the strength of the SO-coupling is $\alpha = 0.4$. The density of states is evaluated in the middle of the junction. Furthermore, the standard S/N/S and S/F/S junctions without SO-coupling are included. In (b) we have shown the spatial dependence of the density of states for the special case of $\phi = \pi$.

This result was presented by Jacobsen and Linder [1], and is in stark contrast to the presupposed behavior for any S/F/S-Josephson junction with a phase difference of $\phi = \pi$. To understand why let us calculate the Green's function in the S/F/S-Josephson junction. For now, the ferromagnet is assumed to be without SO-coupling. Thus, the relevant components of the Green's function present are the singlet component and SRTC. Assuming the two superconductors to be s-wave superconductors, the singlet state has an s-wave symmetry. Moving on to induced triplet states, we will assume that also these have an s-wave symmetry. This assumption is justified by the fact that in the diffusive limit we approximate the Green function to first-order expansion in spherical harmonics; see eq.70. Looking at the linearized

eq.180 and eq.182 we notice that if we define the quantity $f_\pm \equiv d_\| \pm f_s$, eq.180 and eq.182 can be combined to form one single equation. Similarly, the linearized Kupriyanov–Lukichev boundary conditions, as derived in eq.221/eq.225 and eq.223/eq.227 in Appendix A, reduces to one equation for each of the two interfaces. Thus, the quantity $f_\pm$ is determined by

$$\frac{i}{2}D\partial_z^2 f_\pm + \epsilon_\pm f_\pm = 0, \tag{183}$$

$$\zeta L \partial_z f_\pm \Big|_{z=0} = \mp f_{BCS} e^{i\phi_L}, \qquad \zeta L \partial_z f_\pm \Big|_{z=L} = \pm f_{BCS} e^{i\phi_R}, \tag{184}$$

where $\epsilon_\pm \equiv \epsilon \pm h$ and $f_{BCS} = s \cdot i\underline{\sigma}^2$ according to the bulk solution in eq.80.

Solving the above set of equations and defining $k_\pm = \sqrt{2i\epsilon_\pm/D}$, one finds that $f_\pm$ in the middle of the ferromagnet reads [2]

$$f_\pm = \frac{\pm f_{BCS}}{-\zeta L k_\pm \sin(k_\pm L)} \cos(k_\pm L/2)\left(e^{i\phi_R} + e^{i\phi_L}\right). \tag{185}$$

Looking at the above solution, we notice that if $\phi = 0$, $f_\pm$ becomes nonzero. Hence, in this case $f_\pm$ is symmetric with respect to the middle of the ferromagnet. Since $f_\pm$ is just a linear combination of $d_\|$ and f_s, these components must also be symmetric. If we now instead were to choose $\phi = \pi$ things become different. In this case, $f_\pm$ becomes zero. Thus, for a phase difference $\phi = \pi$, $f_\pm$ becomes antisymmetric with respect to the middle of the ferromagnet, meaning that also $d_\|$ and f_s are antisymmetric. In other words, for a phase difference $\phi = \pi$ one has expected the SRTC component to vanish in the middle of the ferromagnet, as well as the singlet, leading to a featureless density of states. As these symmetry properties of the singlet and SRTC components hold both in the case of a ferromagnet without SO-coupling, as well as in the case of just a normal metal (when the SRTC is just zero always), one might think that these symmetry properties also should hold for the long-ranged triplet component when including SO-coupling. Thus, up till now, one has expected both the triplet components to be antisymmetric with respect to the middle of the junction for any S/F/S-Josephson junction with phase difference $\phi = \pi$, as sketched in figure 14.
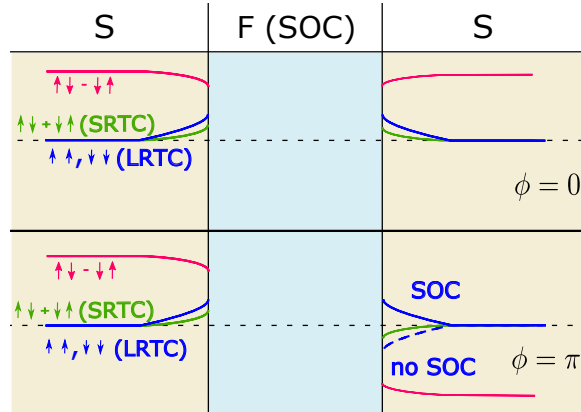
Figure 14: Symmetries properties for the different components in an S/F/S-Josephson junction with SO-coupling(SOC). Pink denotes the singlet component f_s, green denotes SRTC $d_\|$ and blue denotes the LRTC $d_\perp$. The blue stipulated line shows the presupposed symmetry of the LRTC $d_\perp$ based on the behavior without SO-coupling, while the blue line shows the actual symmetry property with SO-coupling.

---

[2] A full calculation is given in the Appendix B.

In figure 13a we see that the presupposed behavior indeed fits well with the S/N/S-Josephson junction and S/F/S-Josephson junction without SO-coupling. At $\phi = \pi$ the density of states is a constant equal to 1. However, when SO-coupling is included, things become different. Instead of a featureless density of states, we get a giant proximity effect at $\phi = \pi$. This surprising result can be understood by looking at the linearized equations derived in section 6.3. Having a field entirely along the (positive) y-axis corresponds to an angle of $\theta = \pi/2$ in eq.175 - eq.176 and eq.179 - eq.182. This produces the following short-ranged and long-ranged triplet components

$$
\left.
\begin{array}{llll}
\text{SRTC:} & d_{||} & \text{in} & \mathbf{e}_y \\
\text{LRTC:} & d_{\perp} & \text{in} & \mathbf{e}_z \\
& d_x & \text{in} & \mathbf{e}_x
\end{array}
\right\} \mathbf{h} = h\mathbf{e}_y,
\tag{186}
$$

determined by the linearized equations

$$
\frac{i}{2}D\partial_z^2 d_x = -2iD\alpha\partial_z d_{\perp} + 2iD\alpha^2 d_{||} + [\epsilon + 2iD\alpha^2]d_x,
\tag{187}
$$

$$
\frac{i}{2}D\partial_z^2 d_{||} = -2iD\alpha\partial_z d_{\perp} + 2iD\alpha^2 d_x + [\epsilon + 2iD\alpha^2]d_{||} + hf_s,
\tag{188}
$$

$$
\frac{i}{2}D\partial_z^2 d_{\perp} = 2iD\alpha\partial_z d_x + 2iD\alpha\partial_z d_{||} + [\epsilon + 4iD\alpha^2]d_{\perp},
\tag{189}
$$

$$
\frac{i}{2}D\partial_z^2 f_s = \epsilon f_s + hd_{||}.
\tag{190}
$$

Knowing that f_s, and hence $\partial_z^2 f_s$, is a symmetric function for phase difference $\phi = 0$ we see from the last equation that also $d_{||}$ must be symmetric for $\phi = 0$. In the case of a phase difference of $\phi = \pi$, then both f_s and $d_{||}$ becomes antisymmetric. We now focus on the equation for $\partial_z^2 d_{||}$. Letting $z \to -z$, the left-hand side is still antisymmetric, meaning that all terms on the right-hand side must be antisymmetric. We already know that the two last terms on the right-hand side are antisymmetric, so these two terms fulfill the requirement of antisymmetry as they should. Looking at the first term $-2iD\alpha\partial_z d_{\perp}$ on the right-hand side we notice that this term contains a first-order partial derivative with respect to z. Therefore, when $z \to -z$, $d_{\perp}$ must be symmetric for this term to be antisymmetric. Furthermore, the second term on the right-hand side ,$2iD\alpha^2 d_x$, contains no partial derivatives, resulting in d_x being antisymmetric to fulfill the symmetry requirement. In other words, we have shown based on the linearized equations that the perpendicular triplet component $d_{\perp}$ is symmetric with respect to the middle of the junction for a phase difference of $\phi = \pi$. This is the opposite of what we found by direct inspection of the solution of the Green's function in eq.185, in the case of no SO-coupling. Looking at figure 13a, we see that a symmetric triplet component $d_{\perp}$ fits well with the numerical results. Having a triplet component $d_{\perp}$ present in the middle of the junction will result in a peak in the density of states, which is exactly what we see in the figure. Furthermore, since the singlet component vanishes in the middle of the junction, this peak is entirely due to the long-ranged triplet component LRTC.

In the argumentation above, we have used a specific choice of SO-coupling and exchange field. One can therefore question the general validity of the giant proximity effect in an S/F/S-Josephson junction with SO-coupling. However, the key requirement in the argumentation

above is that we have a first-order derivative coupled to the exchange field in the corresponding direction. Looking at the general Riccati-parameterized Usadel eq.124 this is exactly what we have. The giant proximity effect is therefore not dependent on the specific choice of the SO-coupling or exchange field. As long as we have a component along the direction of the partial derivative, the argument above holds.

Another important question is how the giant proximity effect depends on the distance from the interfaces. After all, the density of states plotted in figure 13a is evaluated in the middle of the ferromagnet. Plotting the spatial dependence of the density of states for a phase difference of $\phi = \pi$, see figure 13b, we see that the giant proximity effect is independent of the distance from the interfaces. The peak originating from the LRTC persists throughout the system and barely changes. In other words, the spin-triplet polarized state generated by the SO-coupling persists throughout the junction. If we increase the length of the ferromagnet, we expect the magnitude to decrease, yet remain constant throughout the ferromagnet. Checking for different lengths we indeed find that the latter holds (plots not included). Furthermore, when plotting the zero-energy density of states as a function of the length of the ferromagnet L in figure 15, we clearly see that the magnitude decreases rapidly, becoming featureless with a value of 1 at 55 nm. As the LRTC has a coherence length comparable to the coherence length of the singlet state in a normal metal, which typically is in the range 60 - 100 nm [70], the displayed behavior is indeed as expected.
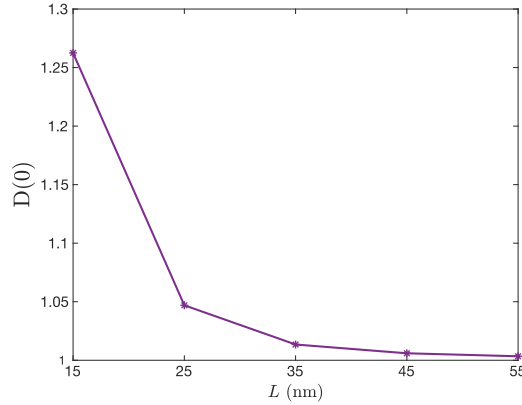

Figure 15: The zero-energy density of states D(0) as a function of the length of the ferromagnet L. The ferromagnet has an exchange field $\mathbf{h} = 10\Delta\mathbf{e}_y$ and the strength of the SO-coupling is $\alpha = 0.4$. Moreover, the phase difference between the superconductors is $\phi = \pi$

To summarize, what Jacobsen and Linder showed was that having SO-coupling present in an S/F/S-Josephson junction with a phase difference ϕ, in fact generates a pure spin triplet state[3] which can persist throughout the ferromagnet. This pure spin triplet state manifests as a giant peak in the density of states, giving what the authors call the giant proximity effect. This giant proximity effect is in stark contrast to what one finds when SO-coupling is not present. Being solely based on symmetry arguments, this effect is independent of the specific system parameters. The S/F/S-Josephson junction with SO-coupling investigated by Jacobsen and Linder indeed offers a promising way to generate, control and isolate LRTC.

---

[3] Having assumed the induced triplet states to have an s-wave symmetry, they have to be odd in frequency to fulfill the antisymmetry of the total wavefunction according to figure 5

S/F/S IN A H-GEOMETRY

Now that we have a basic understanding of how the one-dimensional S/F/S-Josephson junction with SO-coupling behaves, we will explore the new H-geometry suggested by Ouassou [34], where two such junctions are connected by a perpendicular nanowire, thereby creating an effective odd-frequency Josephson junction. We first discuss the experimental set-up of the system we want to simulate, as well as a brief discussion of the numerical method used. We also present the linearized equations, before discussing our results. The results are presented for the case in which the nanowire is a normal metal and a ferromagnet without and with SO-coupling.

8.1 EXPERIMENTAL SET-UP

The geometrical set-up for the H-geometry is shown in figure 16. The two parallel S/F/S-Josephson junctions are assumed to lie along the z-axis, with an exchange field $\mathbf{h} = 10\Delta\mathbf{e}_y$ and length $L = 15$ nm. Furthermore, a Rashba SO-coupling strength $\alpha = 0.4/L$ is chosen. Hence, the two parallel S/F/S-Josephson junctions are nothing but what we explored in the previous chapter, with the same SO-field and exchange field. Furthermore, we denote the phase difference of the S/F/S-Josephson junction to the left by $\phi_1 = \phi_{21} - \phi_{11}$, while $\phi_2 = \phi_{22} - \phi_{12}$ denotes the phase difference of the S/F/S-Josephson junction to the right. All superconductors are assumed to have the same magnitude Δ, and we use a superconducting coherence length of $\xi = 30$. Therefore, the Thouless energy when solving in the two parallel systems becomes $\epsilon_T = D/L^2 = (\xi/L)^2 = 4$. For the interfaces with the superconductors we have chosen an interface parameter $\xi_n = R_B/R_n = 3$.

Figure 16: A sketch of our experimental set-up for the H-geometry. The two parallel S/F/S-Josephson junctions explored previously are connected by a perpendicular nanowire of length L'. In general, we allow for nonzero fields $\mathbf{h}'$ and $\underline{\mathcal{A}}'$ in the central nanowire.

To complete the H-geometry, the two parallel S/F/S-Josephson junctions are connected by a nanowire of length L' lying in the y-direction. We will consider both a normal and a ferromagnetic wire. When the nanowire is ferromagnetic, we choose a SO-field $\underline{\mathcal{A}}'$ along the y-direction. Having a broken inversion symmetry vector $\mathbf{e}_n = (\mathbf{e}_x + \mathbf{e}_z)/\sqrt{2}$, the SO-field reads $\underline{\mathcal{A}}' = (0, \alpha'(-\underline{\sigma}^1 + \underline{\sigma}^3), 0)$. We have chosen a SO-coupling strength $\alpha' = 0.4/L'$.

Moreover, we allow for a general exchange field $\mathbf{h}' = h'_x\mathbf{e}_x + h'_y\mathbf{e}_y + h'_z\mathbf{e}_z = h'\sin(\theta')\cos(\varphi')\mathbf{e}_x + h'\sin(\theta')\sin(\varphi')\mathbf{e}_y + h'\cos(\theta')\mathbf{e}_z$, where θ' denotes the polar angle and φ' denotes the azimuthal angle. Furthermore, the strength of the exchange field is denoted h'. As for the two parallel S/F/S-Josephson junctions, we will use $\zeta = 30$ in the Thouless energy $\epsilon_T = D/L'^2 = (\zeta/L')^2$ when solving for the central nanowire. We will also assume the interfaces with the parallel S/F/S-Josephson junctions to have an interface parameter $\zeta_n = R_B/R_n = 3$.

8.2   NUMERICAL METHOD

In this section, we summarize the non-trivial key-points of the numerical method used to simulate the system. Assuming the central nanowire to have a minimal effect on the two parallel S/F/S-Josephson junctions, we can solve the two parallel S/F/S-Josephson junctions independently. That is, to solve the two parallel S/F/S-Josephson junctions, we use the same method as outlined in the previous chapter. As in the previous chapter, we assume the superconductors to have the bulk solution encountered earlier in eq.123, with in general four different phases. Then we solve in the central nanowire with the respective fields, still with the same method as in the two parallel S/F/S-Josephson junctions, but now using the Green's function in the middle of the two parallel S/F/S-Josephson junctions as input in the new Kupriyanov–Lukichev boundary conditions for the central nanowire. For simplicity, we connect the central nanowire in the middle of the two parallel S/F/S-Josephson junctions. Since we only solve in one direction each time, we can still use the one-dimensional Usadel equation, even though the geometry is two-dimensional. Finally, in the central nanowire we again scale the energy and exchange fields to the superconducting gap Δ.

8.3   ANALYTICAL FOUNDATION

Before we present the results, we will in this section present the linearized equations for the case of an exchange field $\mathbf{h}'$ in xy- and xz-plane separately. The linearized equations in the yz-plane become qualitatively similar to what we find in the xy-case. The only difference is that we need to interchange the role of z and y in the equations. Therefore, we will not list the equations.

We start by considering a field in the xy-plane, i.e. $\mathbf{h}' = h'(\cos(\varphi')\mathbf{e}_x + \sin(\varphi')\mathbf{e}_y)$, where the SRTC' $d'_{||}$ and LRTC' $d'_\perp$ are defined as

$$\begin{aligned} d'_{||} &= d'_x\cos(\varphi') + d'_y\sin(\varphi'), \\ d'_\perp &= -d'_x\sin(\varphi') + d'_y\cos(\varphi'). \end{aligned} \tag{191}$$

Along with the relevant form of the SO-field $\underline{A}'$, an exchange field in the xy-plane produces the following linearized equations

$$\begin{aligned} \frac{i}{2}D\partial_y^2 d'_z &= 2iD\alpha'\partial_y d'_{||}\sin(\varphi') + 2iD\alpha'\partial_y d'_\perp\cos(\varphi') \\ &+ 2iD\alpha'^2 d'_{||}\cos(\varphi') - 2iD\alpha'^2 d'_\perp\sin(\varphi') \\ &+ [\epsilon + 2iD\alpha'^2]d'_z, \end{aligned} \tag{192}$$

$$\frac{i}{2}D\partial_y^2 d'_{||} = 2iD\alpha'\partial_y d'_\perp - 2iD\alpha'\partial_y d'_z \sin(\varphi')$$
$$+ 2iD\alpha'^2 d'_z \cos(\varphi') + iD\alpha'^2 d'_\perp \sin(2\varphi') \qquad (193)$$
$$+ [\epsilon + 2iD\alpha'^2(1 + \sin^2(\varphi'))]d'_{||} + h'f'_s,$$

$$\frac{i}{2}D\partial_y^2 d'_\perp = -2iD\alpha'\partial_y d'_z \cos(\varphi') - 2iD\alpha'\partial_y d'_{||}$$
$$- 2iD\alpha'^2 d'_z \sin(\varphi') + iD\alpha'^2 d'_{||} \sin(2\varphi') \qquad (194)$$
$$+ [\epsilon + 2iD\alpha'^2(1 + \cos^2(\varphi'))]d'_\perp,$$

$$\frac{i}{2}D\partial_y^2 f'_s = \epsilon f'_s + h'd'_{||}. \qquad (195)$$

On the other hand, having an exchange field in the xz-plane, i.e. $\mathbf{h}' = h'(\sin(\theta')\mathbf{e}_x + \cos(\theta')\mathbf{e}_z)$, the SRTC' $d'_{||}$ and LRTC' $d'_\perp$ reads

$$d'_{||} = d'_x \sin(\theta') + d'_z \cos(\theta'),$$
$$d'_\perp = -d'_z \sin(\theta') + d'_x \cos(\theta'). \qquad (196)$$

Upon insertion, the linearized equations for an exchange field in the xz-plane becomes

$$\frac{i}{2}D\partial_y^2 d'_y = -2iD\alpha'\partial_y d'_{||}(\cos(\theta') + \sin(\theta'))$$
$$- 2iD\alpha'\partial_y d'_\perp(\cos(\theta') + \sin(\theta')) \qquad (197)$$
$$+ [\epsilon + 4iD\alpha'^2]d'_y,$$

$$\frac{i}{2}D\partial_y^2 d'_{||} = 2iD\alpha'\partial_y d'_y(\cos(\theta') + \sin(\theta'))$$
$$+ 2iD\alpha'^2 d'_\perp \cos(2\theta') \qquad (198)$$
$$+ [\epsilon + 2iD\alpha'^2(1 + \sin(2\theta'))]d'_{||} + h'f'_s,$$

$$\frac{i}{2}D\partial_y^2 d'_\perp = 2iD\alpha'\partial_y d'_y(\cos(\theta') - \sin(\theta'))$$
$$+ 2iD\alpha'^2 d'_{||}\cos(2\theta') \qquad (199)$$
$$+ [\epsilon + 2iD\alpha'^2(1 - \sin(2\theta'))]d'_\perp,$$

$$\frac{i}{2}D\partial_y^2 f'_s = \epsilon f'_s + h'd'_{||}. \qquad (200)$$

8.4   normal metal

We start by analyzing the simplest case, namely the case where all fields in the central nanowire are zero, hence having a normal metal here.

8.4.1   *Results*

Having a normal metal in the central nanowire, we expect the density of states to qualitatively reflect the giant triplet effect seen in the two parallel S/F/S-Josephson junctions, for lengths within the coherence length of singlet states in a normal metal. After all, having a normal metal, we have no SO-fields or exchange fields that can redefine or affect the Cooper-pairs. The magnitude may differ due to the assumption of weak proximity. Nevertheless, the density of states should reflect the qualitative behavior of the giant triplet effect. Plotting the density of states for a normal metal of length $L' = 15$ nm, we see from figure 17a that the density of states indeed reflects the giant triplet effect encountered in the two-parallel S/F/S-Josephson junctions. Remarkably, we also see that the magnitude of the peak in the density of states remains quite similar to what we find in the giant triplet effect. At first glance, this seems odd. After all, we assume weak proximity and therefore do not expect all triplet components to penetrate into the normal metal. However, the normal metal gets a contribution *both* from the S/F/S-Josephson junction to the left and a similar contribution (in the case of equal phase difference) from the S/F/S-Josephson junction to the right. Hence, even though the interfaces with the normal metal effectively lowers the amount of long-ranged triplet components we expect to see in the normal metal, the fact that we have two contributions raises the amount again. Therefore, it is reasonable to expect the peak in the density of states in the normal metal to be of the same magnitude as in the two parallel S/F/S-Josephson junctions.

Plotting the spatial dependency of the density of states for $\phi_1 = \phi_2 = \pi$, as shown in the top right corner of figure 17a, we see that the peak at zero energy also remains constant throughout the normal metal. This fits well with what we expect. Knowing that the LRTC d_z in the giant triplet effect is constant throughout the parallel S/F/S-junctions, there is no reason to expect the situation to become otherwise in the normal metal.

For other choices of ϕ_1 and ϕ_2, we might get a mixture of different components present, yet when these enter the normal metal, there are no fields present that can destroy the Cooper-pairs. Hence, we expect the components to be constant throughout the normal metal for other choices of ϕ_1 and ϕ_2 as well. For instance, plotting the spatial dependency of the components normalized to d'_z for $\phi_1 = \phi_2 = \pi/2$ in figure 17b we indeed see that the components remains constant, in stark contrast to what one finds in the two parallel S/F/S-Josephson junctions. Furthermore, even when choosing $\phi_1 = \phi_2 = \pi/2$, the d_z component dominates. This clearly shows that by having a normal metal in the central nanowire, we effectively have created a "vessel" where the Cooper-pairs can propagate unaffected when the normal metal has a length within the coherence length of singlet states.
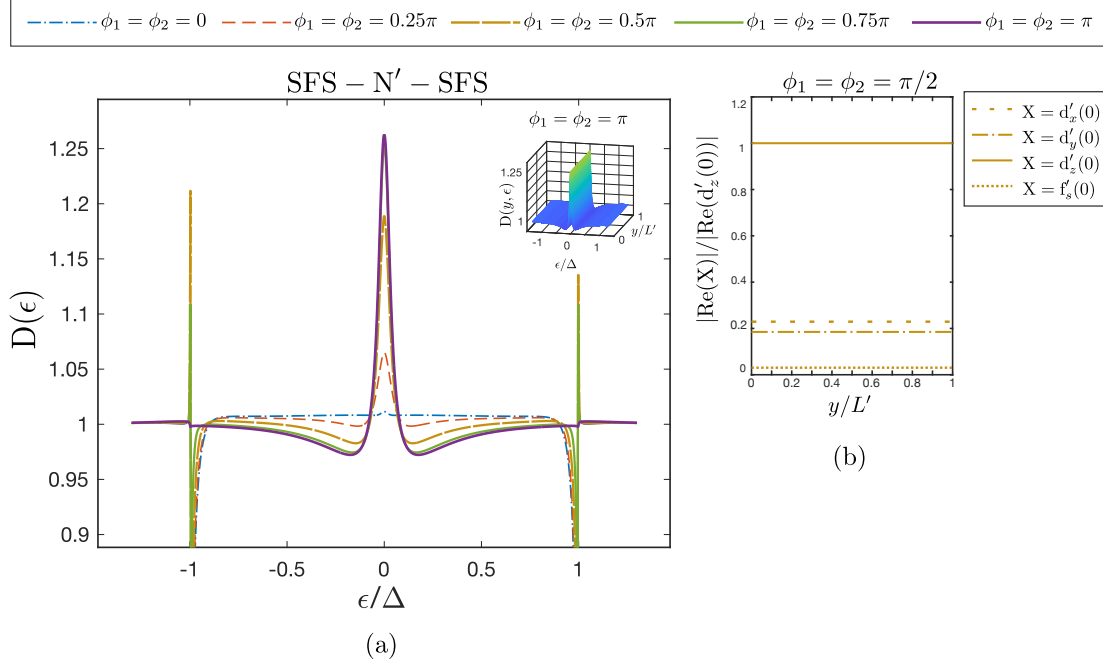
Figure 17: Figure (a) show the density of states $D(\epsilon)$ evaluated in the middle of the central nanowire N' with length $L' = 15$ nm, for a phase difference ϕ_1 and ϕ_2 in the S/F/S-Josephson junction to the left and right respectively. In addition, the spatial dependency for the density of states for the special case $\phi_1 = \phi_2 = \pi$ is shown in the top right corner. Figure (b) shows the ratios of the different components of the d-vector at $\phi_1 = \phi_2 = \pi/2$.

In the above discussion, we stressed that the length of the normal metal must be within the coherence length of singlet states in a normal metal. Even though there are no fields in the normal metal that can affect the Cooper-pairs, they surely cannot survive forever. Increasing the length, one would therefore expect the peak at zero energy in the density of states to decrease in magnitude, similar to what we saw in the one-dimensional S/F/S-Josephson junction in figure 15. In figure 18 we have plotted the the zero-energy density of states as a function of the length L' of the normal metal, while having $\phi_1 = \phi_2 = \pi$. Remarkably, we now find that the zero-energy density of states remains of the same magnitude for lengths up to $L' = 60$ nm. Furthermore, even at $L' = 240$ nm, the zero-energy density of states has not become featureless. Hence, by just connecting two parallel one-dimensional S/F/S-Josephson junctions, thereby creating an effective odd-frequency Josephson junction, the zero-energy peak in the density of states now can persist throughout the junction for several superconducting coherence lengths. In other words, the d_z' component can now survive for lengths far above the expected coherence length. This unexpected behavior has also been observed in other long Josephson junctions with odd-frequency triplet correlations [71, 72, 73].
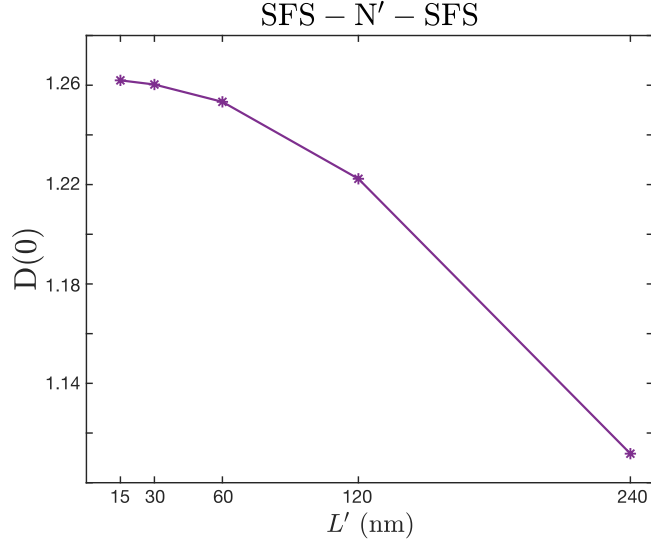
Figure 18: The zero-energy density of states D(0) as a function of the length L' of the central nanowire N'. Here phase differences are set to $\phi_1 = \phi_2 = \pi$, and the density of states is again evaluated in the middle of the nanowire.

It is worth mentioning that in figure 17a we only considered equal phase differences $\phi_1 = \phi_2$ in the two parallel S/F/S-Josephson junctions. One might question if the displayed behavior also should hold for unequal phase differences $\phi_1 \neq \phi_2$. Realizing that we indeed have the displayed behavior for *each* of the two parallel S/F/S-Josephson junctions, we surely would expect the same qualitative behavior in the normal metal if we choose unequal phase differences. The magnitude will differ because we do not get equal contributions from the two parallel S/F/S-Josephson junctions, yet the magnitude should be somewhere between the minimized value at $\phi_1 = \phi_2 = 0$ and the maximized value at $\phi_1 = \phi_2 = \pi$. Furthermore, we will again expect the same length dependency of the zero-energy density of states regardless of the phase differences, as encountered in figure 18. Checking for a selection of unequal phase differences we indeed see that this holds (plots not included). Finally, in the case of unequal phase differences, the spatial dependency will not remain constant throughout the normal metal, because we have two different inputs on each side. Even so, we see the same qualitative behavior as discussed above (plots not included).

8.5   FERROMAGNET WITHOUT SO-COUPLING

We now proceed by including an exchange field $\mathbf{h}'$ in the central nanowire according to figure 16, in which the central nanowire becomes a ferromagnet without SO-coupling. Including an exchange field in the central nanowire, the short-ranged and long-ranged triplet components here may be defined differently from those in the two parallel S/F/S-Josephson junctions. This may lead to different behavior than in the normal metal case. However, not including SO-coupling in the central ferromagnet, we would expect no generation of a LRTC' $d'_\perp$ from a potential SRTC' $d'_\parallel$ (or vice versa). In the following, we will discuss the limiting cases of an exchange field entirely along the x- y- and z-axes.

8.5.1 *Symmetries*

In the previous chapter, we saw that the different components of the d-vector in a one-dimensional S/F/S-Josephson junction with SO-coupling and phase difference ϕ, had specific symmetry properties for the two special cases $\phi = 0$ and $\phi = \pi$. Now that we have two parallel S/F/S-Josephson junctions with phase differences ϕ_1 and ϕ_2 respectively, the components of the d-vector in the central ferromagnet will get a contribution from the left-hand side and right-hand side. In other words, for the special cases where $\phi_{1/2} = 0$ and $\phi_{1/2} = \pi$, the initial symmetries of the components of the d-vector in the central ferromagnet are known. However, when entering the central ferromagnet, the definition of the SRTC' and LRTC' in terms of the d-vector may change. It is therefore useful to relate the definitions of the new SRTC' and LRTC' in the central ferromagnet to the known symmetries at $\phi_{1/2} = 0$ and $\phi_{1/2} = \pi$ in the two parallel S/F/S-Josephson junctions.

First let us consider the case in which the exchange field points along the x-axis, i.e. $\mathbf{h}' = h'\mathbf{e}_x$. This would correspond to setting $\varphi' = 0$ in eq.191, and produces the following short-range and long-ranged triplet components

$$\left.\begin{array}{llll} \text{SRTC':} & d'_\parallel & \text{in} & \mathbf{e}_x \\ \text{LRTC':} & d'_\perp & \text{in} & \mathbf{e}_y \\ & d'_z & \text{in} & \mathbf{e}_z \end{array}\right\} \mathbf{h}' = h'\mathbf{e}_x. \tag{201}$$

Remembering that in the parallel S/F/S-Josephson junctions the SRTC and LRTC are defined by eq.186, we immediately notice that the LRTC $d_\perp$ in the two parallel S/F/S-Josephson junctions becomes the LRTC' d'_z in the central ferromagnet. Nevertheless, the d'_z component is still a long-ranged triplet component because it is perpendicular the exchange field. Thus, the initial symmetries for a phase difference of $\phi_{1/2} = 0$ and $\phi_{1/2} = \pi$ reads

$\mathbf{h}' = h'\mathbf{e}_x$	$\phi_{1/2} = 0$	$\phi_{1/2} = \pi$
$d'_\parallel$	symmetric	antisymmetric
$d'_\perp$	symmetric	antisymmetric
d'_z	antisymmetric	symmetric
f'_s	symmetric	antisymmetric

Table 1: Symmetry properties for the initial d-vector components when having an exchange field along the x-direction. In the case of equal phase differences, the two parallel S/F/S-Josephson junctions contribute with equal symmetry properties. For unequal phase differences, the symmetry properties will be a combination of the two, yet we can still say something about which components are present in the middle of the central ferromagnet.

We now move on to the case in which the exchange field points in the y-direction, $\mathbf{h}' = h'\mathbf{e}_y$. This would correspond to setting $\varphi' = \pi/2$ in eq.191, and produces the following short-ranged and long-ranged triplet components

$$\left.\begin{array}{llll} \text{SRTC':} & d'_\parallel & \text{in} & \mathbf{e}_y \\ \text{LRTC':} & d'_\perp & \text{in} & \mathbf{e}_x \\ & d'_z & \text{in} & \mathbf{e}_z \end{array}\right\} \mathbf{h}' = h'\mathbf{e}_y. \tag{202}$$

From the above, we immediately notice that in this particular case the SRTC' and LRTC' in the central ferromagnet are defined the same way as in our two parallel S/F/S-Josephson junctions, if we just interchange the role of $d'_\perp$ and d'_z. As both these components are LRTC', and just a matter of how we choose to isolate the two, this interchanging does not matter for the physics governing the system. Moreover, the initial symmetries when having an exchange field along the y-direction now become

$\mathbf{h}' = h'\mathbf{e}_y$	$\phi_{1/2} = 0$	$\phi_{1/2} = \pi$
$d'_\parallel$	symmetric	antisymmetric
$d'_\perp$	symmetric	antisymmetric
d'_z	antisymmetric	symmetric
f'_s	symmetric	antisymmetric

Table 2: Symmetry properties for the initial d-vector components when having an exchange field along the y-direction.

Finally, we consider the case where the exchange field points in the z-direction, $\mathbf{h}' = h'\mathbf{e}_z$. This would correspond to setting $\theta' = 0$ in eq.196, and produces the following short-ranged and long-ranged triplet components

$$\left.\begin{array}{llll} \text{SRTC':} & d'_\parallel & \text{in} & \mathbf{e}_z \\ \text{LRTC':} & d'_\perp & \text{in} & \mathbf{e}_x \\ & d'_y & \text{in} & \mathbf{e}_y \end{array}\right\} \mathbf{h}' = h'\mathbf{e}_z. \tag{203}$$

Looking at the above definitions, we notice that the LRTC $d_\perp$ in the parallel S/F/S-Josephson junctions become the SRTC' $d'_\parallel$ in the central ferromagnet. Furthermore, the d_x component becomes the $d'_\perp$ in the central ferromagnet, yet this is still defined as an LRTC'. Thus, we have the following initial symmetries

$\mathbf{h}' = h'\mathbf{e}_z$	$\phi_{1/2} = 0$	$\phi_{1/2} = \pi$
$d'_\parallel$	antisymmetric	symmetric
$d'_\perp$	symmetric	antisymmetric
d'_y	symmetric	antisymmetric
f'_s	symmetric	antisymmetric

Table 3: Symmetry properties for the initial d-vector components when having an exchange field along the y-direction.

Looking at the table above, we notice that the SRTC' does not have the same symmetry property as the singlet component for both $\phi_{1/2} = 0$ and $\phi_{1/2} = \pi$. This is in stark contrast to what we saw when having an exchange field in the x- and y-direction[1], where the SRTC' has the same symmetry property as the singlet component for both phase differences. Therefore, we may expect qualitatively different behavior when the field points along the z-direction.

---

[1] and any standard one-dimensional S/F/S-Josephson junction for that matter

8.5.2 *Results*

Exchange field along the x- and y-direction

Let us first consider the case in which $\phi_1 = \phi_2 = \pi$. From table 1 and table 2, we see that the only nonzero component present is d'_z. Therefore, we expect a peak in the density of states to appear, similar to the one seen in the normal metal case. As in the normal metal case, we do expect the peak to be of the same magnitude as in the two parallel S/F/S-Josephson junctions, due to two contributions. Decreasing the phase differences, yet choosing them equal to each other, we would expect a smaller amount of the LRTC $d_\perp$ to be generated in the two parallel S/F/S-Josephson junctions, thus expecting the peak in the density of states to decrease. Plotting the density of states, for instance, for a field along the x-direction in figure 19, we indeed see such behavior. The density of states for a field along the y-direction behaves qualitatively similar (plots not included).
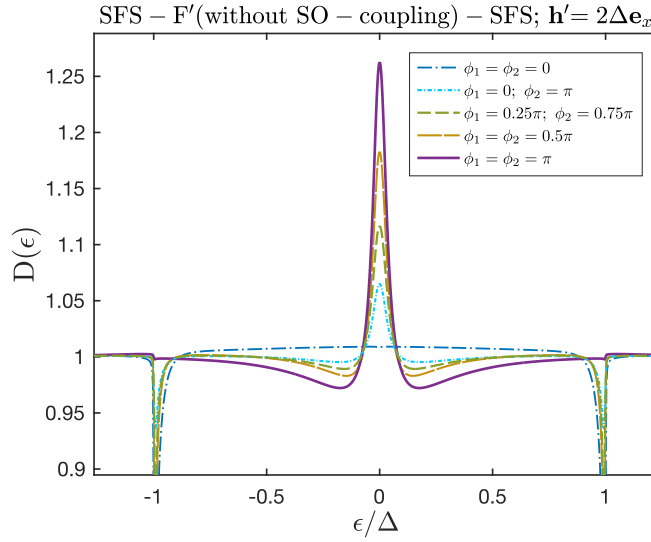

Figure 19: Density of states $D(\epsilon)$ evaluated in the middle of the central nanowire F', for a phase difference ϕ_1 and ϕ_2 in the S/F/S-Josephson junction to the left and right respectively. The central nanowire F' has an exchange field $\mathbf{h}' = 2\Delta\mathbf{e}_x$ and a length $L' = 15$ nm, and does not exhibits SO-coupling.

Looking at the figure above, it is worth noticing that our effective Josephson junction does display qualitatively different behavior from the one-dimensional S/F/S-Josephson junction. For instance, if we choose $\phi_1 = \phi_2 = \pi$ we do not get the same density of states as if we choose $\phi_1 = \phi_2 = 0$, due to the different initial symmetries. Although, the *effective* phase difference $\phi' \equiv \phi_1 - \phi_2$ in both cases is 0. This is qualitatively different from the one-dimensional S/F/S-Josephson junction.

From figure 19 it is also worth noticing that choosing $\phi_1 = \phi_2$ tends to maximize the density of states. For instance, suppose $\phi_1 = \phi_2 = \pi/2$. We can destroy this symmetric distribution by moving 0.25π of the phase difference from ϕ_1 to ϕ_2, giving $\phi_1 = 0.25\pi$ and $\phi_2 = 0.75\pi$. Looking at figure 19 we notice that the peak in the density of states decreases. We could also move the hole phase difference, giving $\phi_1 = 0$ and $\phi_2 = \pi$. Again, we see from the figure that the

density of states decreases even more. Hence, if we try to induce an *effective* phase difference in our system by choosing $\phi_1 \neq \phi_2$ (giving $\phi' = \phi_1 - \phi_2 \neq 0$), the density of states is suppressed. We again notice the qualitative different behavior from the one-dimensional S/F/S-Josephson junction.

Let us now discuss how changing the length of the central ferromagnet affects the density of states. For the special case $\phi_1 = \phi_2 = \pi$, we know that the only component present is d'_z. Thus increasing the length, we expect the zero-energy density of states to behave similarly to the normal metal case. However, one might wonder if this would also hold for other choices of ϕ_1 and ϕ_2. Having an exchange field entering the Usadel equation may cause the ratios between the different components of the d-vector to change. Thus, even though the density of states itself displays a behavior qualitatively similar to the normal metal case when the phase differences ϕ_1 and ϕ_2 are varied, the ratios between the different components may not. In contrast to the normal metal case, a change in the relative magnitudes of the components of the d-vector would be of importance when we have an exchange field present, due to different coherence lengths. One could also argue that the ratios between the different components should be different when having an exchange field in the x- and y-direction. Recall, when solving the linearized equations for the different components in eq.171 - eq.174, the exchange field enters the equations differently in the two cases.

However, we recall that even when choosing $\phi_1 = \phi_2 = \pi/2$ in the normal metal case, the singlet component is marginal. Since the exchange field only couples to the singlet component, we will not expect the exchange field to be of large importance for the ratios of the different components when comparing an exchange field along the x- and y-direction. Moreover, we would also still expect the same behavior of the ratios as we saw in the normal metal case, that is, a dominant d'_z component, by the same reasoning. Plotting the spatial dependence of the different components at zero-energy for $\phi_1 = \phi_2 = \pi/2$, while having a field in the x-direction, we see from figure 20a that the latter holds. As in the normal metal case, the component d'_z still dominates. Thus, we would still expect the zero-energy density of states to persist for several superconducting coherence lengths as in the normal metal case. Plotting the zero-energy density of states as a function of the length L' in figure 20b we indeed see that this holds. Checking the spatial dependency of the different components while having a field in the y-direction, the ratios become identical (plot not included) as expected. Hence, we indeed get the same behavior of the zero-energy density of states as seen in figure 20b.
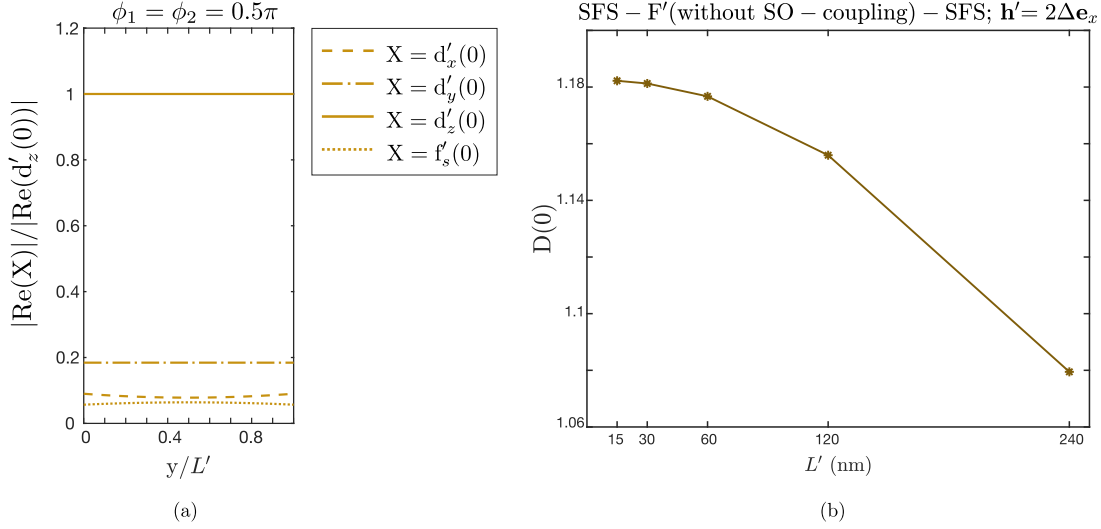
Figure 20: The different components of the d-vector evaluated at zero-energy in the case of $\phi_1 = \phi_2 = \pi/2$ for a ferromagnetic nanowire F' without SO-coupling (a). The ferromagnet has an exchange field $\mathbf{h}' = 2\Delta \mathbf{e}_x$ and a length $L' = 15$. All components are normalized to d'_z. Figure (b) shows the corresponding zero-energy density D(0) as a function of the length L'. In both cases, the quantities are evaluated in the middle of F'.

Exchange field along the z-direction

Let us first consider the special case when $\phi_1 = \phi_2 = \pi$. Due to the symmetries in table 3, the only nonzero component initially present in the central ferromagnet is the SRTC' $\mathrm{d}'_\parallel$. When we have an exchange field present, we know that a short-ranged triplet component can be generated from a singlet component due to singlet-triplet mixing. This effect also works the other way around, a singlet component can also be generated from a short-ranged triplet component when having an exchange field present. As the Cooper-pairs enter the central ferromagnet the exchange field starts to rotate these Cooper-pairs into singlet states. When the Cooper-pairs move further through the central ferromagnet, this effect decreases the amount of Cooper-pairs being SRTC' and increases the amount of Cooper-pairs being in the singlet state. Eventually, all Cooper-pairs are rotated into the singlet state[2]. Hence, for small lengths, we would expect the system to be dominated by the SRTC', while for larger lengths the singlet component is expected to dominate. Plotting the density of states for lengths between 5 nm and 60 nm in figure 21, we clearly see this trend. For small lengths, we see a peak in the density of states, while what resembles a minigap appears for larger lengths. The zero-energy suppression in the density of states is still so marginal that it hardly can be called a minigap, yet for simplicity, we will refer to such zero-energy suppression in the density of states as minigap. Hence, when we have an exchange field in the *z*-direction, we can switch between a peak and a minigap in the density of states just by increasing the length of the central ferromagnet. This is qualitatively

---

[2] This singlet state could in theory be rotated back to SRTC', yet in practice when the Cooper-pairs have propagated a distance closer and closer to the coherence length the fewer Cooper-pairs we have to rotate. Therefore, the coherence length eventually cancels out this oscillation between the two components

different behavior from what we have seen for an exchange field along the x- and y-direction, where the peak at zero-energy in the density of states can persist throughout the junction for several superconducting coherence lengths.

We also emphasize the difference in the length scale in which the variation in the density of states occurs. In stark contrast to the previous cases, having an exchange field along the z-direction, the density of states becomes featureless at a length of 60 nm, that is, twice the superconducting coherence length. This difference in the relevant length scale for the two cases surely originates from which components are present. For an exchange field in the x- and y-direction the peak originates from the LRTC' d'_z, yet having a field in the z-direction it is the SRTC' $d'_{||}$ and singlet component that governs the qualitative behaviour. As we know, the LRTC' surely has a larger coherence length than the SRTC' and singlet component.
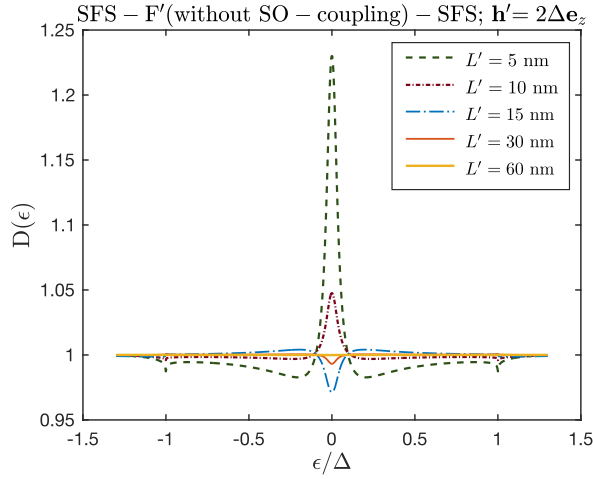

Figure 21: Density of states $D(\epsilon)$ at $\phi_1 = \phi_2 = \pi$ evaluated in the middle of the central nanowire F' with a length L'. The central nanowire F' has an exchange field $\mathbf{h}' = 2\Delta\mathbf{e}_z$, and does not exhibit SO-coupling.

Having seen that the density of states changes from having a peak at short lengths to a minigap at longer lengths, let us now discuss how varying the phase differences ϕ_1 and ϕ_2 affects the density of states for the lengths $L' = 5$ nm and $L' = 15$ nm, respectively. Starting with a length of $L' = 5$ nm, we know that the system is dominated by the SRTC' $d'_{||}$ at $\phi_1 = \phi_2 = \pi$, yet this is nothing but the d_z component in the two parallel S/F/S-systems. Thus, by decreasing the phase differences, we again expect this component to decrease, thereby expecting the same behavior as seen in the x- and y-case. After all, at such short lengths, whether we have SRTC' or LRTC' present does not matter for the density of states. From figure 22a we indeed see such a behavior. If we now increase the length to $L' = 15$ nm, we know that the exchange field rotates the SRTC' into singlet states. Although, when decreasing the phase differences, we know that the amount of $d'_{||}$ present initially also decreases. Having simply less $d'_{||}$ to rotate, we expect to see a reduction in the minigap. Looking at figure 22b we indeed see such a behavior.
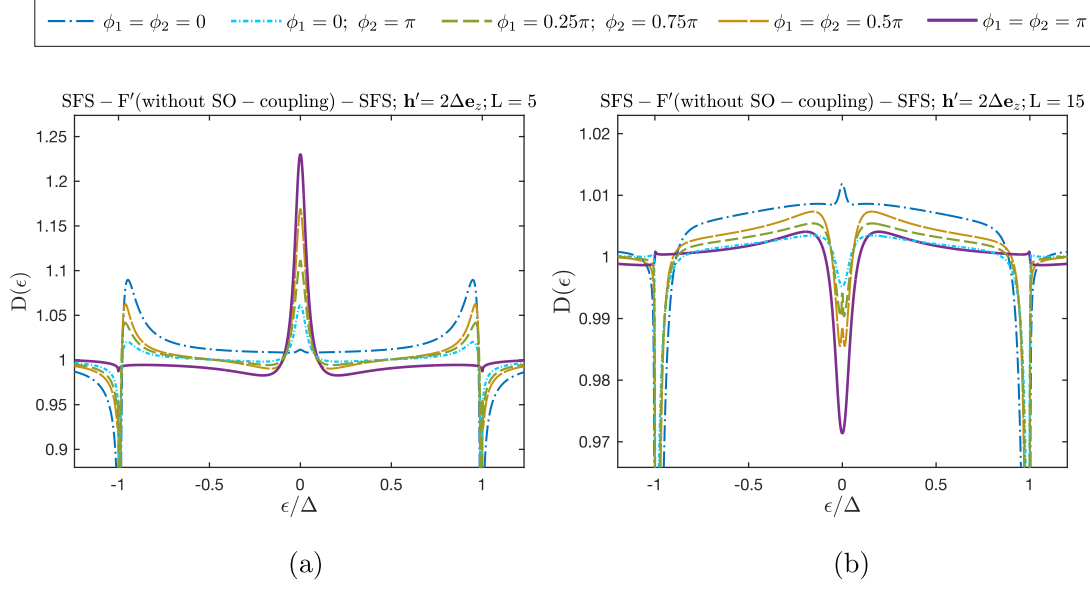
Figure 22: Density of states $D(\epsilon)$ evaluated in the middle of the central nanowire F', for a phase difference ϕ_1 and ϕ_2 in the S/F/S-Josephson junction to the left and right respectively. We have considered a nanowire of length $L' = 5$ nm (a) and $L' = 15$ (b). Furthermore, the nanowire has an exchange field $\mathbf{h}' = 2\Delta\mathbf{e}_z$, and does not exhibits SO-coupling.

Looking at the figures above, we again notice that the effective Josephson junction displays qualitatively different behavior from the one-dimensional S/F/S-Josephson junction. That is, choosing $\phi_1 = \phi_2 = 0$ does not result in the same density of states as $\phi_1 = \phi_2 = \pi$, although the *effective* phase difference $\phi' = \phi_1 - \phi_2$ in both cases is zero. Furthermore, we again notice that choosing $\phi_1 \neq \phi_2$, thus inducing an *effective* phase difference ϕ', tends to suppress the density of states.

We also notice that the minigap we see in figure 22b behaves qualitatively different from the minigap seen in the one-dimensional S/N/S-Josephson junction (see figure 13a). While the one-dimensional S/N/S-Josephson junction has a minigap appearing at $\phi = 0$ and disappearing at $\phi = \pi$, the minigap now appears at $\phi_1 = \phi_2 = \pi$ and disappears at $\phi_1 = \phi_2 = 0$. This may seem a bit odd at first glance. However, remember that in the one-dimensional S/N/S-Josephson junction, the singlet component originates from the superconductors themselves. In contrast, the singlet component present in our effective Josephson junction originates from the $d'_{\parallel}$ component. Therefore, the singlet component present in our effective Josephson junction has the same symmetry properties as $d'_{\parallel}$, which in the case of an exchange field along the z-direction is opposite to those originating from the superconductors.

8.6 FERROMAGNET WITH SO-COUPLING

In the above, we saw the effect of including an exchange field in the central nanowire. We now proceed by finally including a SO-field, thus allowing for a generation of LRTC' from an SRTC' and vice versa. As we saw previously, the density of states behaves identically for an exchange field in the x- and y-direction. Including a SO-field, we might get different behavior in these two cases, due to having a misalignment/alignment between the **h**-field and SO-field.

8.6.1 *Results*

Exchange field along the x- and y-direction

Let us start by considering an exchange field in the x-direction, i.e. $\mathbf{h}' = h' \mathbf{e}_x$. As we saw earlier, such a field produces the SRTC' and LRTC' as written in eq.201, whose relative proportions are determined by the equations

$$\frac{i}{2} D \partial_y^2 d_z' = 2iD\alpha' \partial_y d_\perp' + 2iD\alpha'^2 d_{||}' + [\epsilon + 2iD\alpha'^2] d_z', \tag{204}$$

$$\frac{i}{2} D \partial_y^2 d_{||}' = 2iD\alpha' \partial_y d_\perp' + 2iD\alpha'^2 d_z' + [\epsilon + 2iD\alpha'^2] d_{||}' + h' f_s', \tag{205}$$

$$\frac{i}{2} D \partial_y^2 d_\perp' = -2iD\alpha' \partial_y d_z' - 2iD\alpha' \partial_y d_{||}' + [\epsilon + 4iD\alpha'^2] d_\perp', \tag{206}$$

$$\frac{i}{2} D \partial_y^2 f_s' = \epsilon f_s' + h' d_{||}'. \tag{207}$$

We start by discussing the case in which $\phi_1 = \phi_2 = \pi$. For such a choice, we recall from table 1 that the only component present initially is d_z'. Without SO-coupling, this component cannot be rotated into other triplet states. However, if we now turn on SO-coupling, we see from eq.206 that a symmetric d_z' generates an antisymmetric $d_\perp'$. Furthermore, the component d_z' can also be rotated back to the SRTC' $d_{||}'$, which now must be symmetric according to eq.205. Thus, turning on SO-coupling we go from only having the d_z' component present, to also having the $d_\perp'$ and $d_{||}'$ components present. Yet, since the component $d_\perp'$ is antisymmetric, this surely must vanish in the middle of the junction. Hence, the only component that we actually see in the density of states is the SRTC' $d_{||}'$. At $\phi_1 = \phi_2 = \pi$ we therefore expect to see a reduction in the peak, simply because we "lose" some of the Cooper-pairs to the antisymmetric $d_\perp'$. Looking at figure 23 we surely see such a reduction of the peak in the density of states at $\phi_1 = \phi_2 = \pi$.

One might question if now having SO-coupling present in the system would result in qualitatively different behavior for other choices of ϕ_1 and ϕ_2. However, from our discussion of the ferromagnet without SO-coupling, we remember that the system was dominated by the LRTC' $d_{z'}'$ for other choices as well. Hence, even when varying the phase differences we do start with a $d_{z'}'$ component (and not an SRTC'), thus still expecting the peak to decrease when turning on SO-coupling. Checking for other other choices of ϕ_1 and ϕ_2, we indeed see such behavior (plots not included).
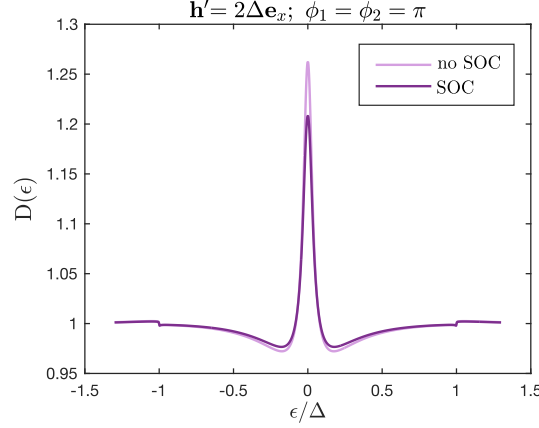
Figure 23: A comparison between the density of states $D(\epsilon)$ evaluated in the middle of a ferromagnetic nanowire F′ with an exchange field $\mathbf{h}' = 2\Delta\mathbf{e}_x$ and length $L' = 15$ nm, without and with SO-coupling (SOC). Phase differences are set to $\phi_1 = \phi_2 = \pi$.

Moving on to an exchange field in the y-direction, i.e. $\mathbf{h}' = h'\mathbf{e}_y$, the SRTC′ and LRTC′ are defined by eq.202. The relative proportions of these components are determined by the equations

$$\frac{i}{2}D\partial_y^2 d_z' = 2iD\alpha'\partial_y d_{||}' - 2iD\alpha'^2 d_\perp' + [\epsilon + 2iD\alpha'^2]d_x', \tag{208}$$

$$\frac{i}{2}D\partial_y^2 d_{||}' = 2iD\alpha'\partial_y d_\perp' - 2iD\alpha'\partial_y d_z' + [\epsilon + 4iD\alpha'^2]d_{||}' + h'f_s', \tag{209}$$

$$\frac{i}{2}D\partial_y^2 d_\perp' = -2iD\alpha'\partial_y d_{||}' - 2iD\alpha'^2 d_z' + [\epsilon + 2iD\alpha'^2]d_\perp', \tag{210}$$

$$\frac{i}{2}D\partial_y^2 f_s' = \epsilon f_s' + h'd_{||}'. \tag{211}$$

Let us again consider the case in which $\phi_1 = \phi_2 = \pi$. Having an exchange field along the y-direction, the component present initially still is d_z', due to the symmetries in table 2. If we turn on SO-coupling in the system, a symmetric d_z' generates a symmetric $d_\perp'$ and an antisymmetric $d_{||}'$ according to eq.210 and eq.209 respectively. Hence, as in the previous case, the latter component vanishes in the middle of the ferromagnet, resulting in a qualitative similar behavior as we saw in figure 23 (plot not included). For other choices of ϕ_1 and ϕ_2, we indeed find a similar behavior, that is, a reduction of the peak in the density of states (plots not included).

It is interesting to note that despite the misalignment/alignment of the exchange field and SO-field when having a $\mathbf{h}'$ field along the x/y-direction, the density of states displays the same behavior regardless of how we choose ϕ_1 and ϕ_2. This might be due to the relatively short length. Having a length of 15 nm, whether the triplet component is an SRTC′ or an LRTC′ does not matter for the density of states. Yet, if we increase the length, we may expect a different

behavior when having an exchange field along the x- and y-direction. Let us now discuss the zero-energy density of states at $\phi_1 = \phi_2 = \pi$ in the two cases.

Starting with an exchange field along the x-direction, the triplet components present in the middle of the central ferromagnet are the LRTC' d'_z and SRTC' $d'_{\parallel}$. Thus, the total triplet component vector becomes $\mathbf{d}'_{\text{tot}} = |\mathbf{d}'_z \times \tilde{\mathbf{d}}'_{\parallel}| \sim \mathbf{e}_y$. That is, the total triplet component $\mathbf{d}'_{\text{tot}}$ is perpendicular to the exchange field, thereby still being defined as a long-ranged. We would therefore expect to see the same behavior of the zero-energy density of states when increasing the length as seen without SO-coupling in figure 20b. Looking at figure 24 we indeed see such behavior.

Moving on to the case when the exchange field points along the y-direction, the components present becomes the LRTC' d'_z and LRTC' $d'_\perp$. Even so, these components still points in the z- and x-direction respectively, again resulting in a total triplet component vector $\mathbf{d}'_{\text{tot}} = |\mathbf{d}'_z \times \tilde{\mathbf{d}}'_\perp| \sim \mathbf{e}_y$. However, having a field along the y-direction, the total triplet component $\mathbf{d}'_{\text{tot}}$ is now defined as short-ranged. In contrast to the previous case, we would therefore expect the zero-energy density of states to fall more rapidly when increasing the length of central ferromagnet. Looking at figure 24 we clearly see such behavior.
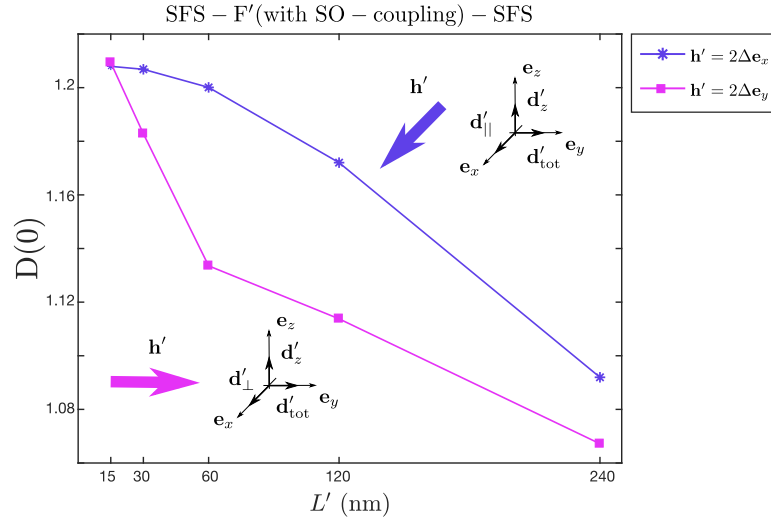

Figure 24: The zero-energy density of states D(0) as a function of the length L' of a ferromagnetic nanowire F' with SO-coupling. Here phase differences are set to $\phi_1 = \phi_2 = \pi$ and the density of states is again evaluated in the middle of the central nanowire F'. Purple shows the behavior for the case of an exchange filed $\mathbf{h}' = 2\Delta\mathbf{e}_x$, while pink shows the behavior for $\mathbf{h}' = 2\Delta\mathbf{e}_y$. In addition, a geometrical illustration of the different components in the two cases are shown.

An important key-point in the argumentation above is that we do consider the total triplet component vector and not just the generated triplet component. If we had just considered the generated triplet component, the opposite behavior would be expected. Recall that the generated component in the case of an exchange field along the x-direction is defined as an SRTC', whereas if the exchange field along the y-direction, the generated component is defined as an LRTC'. Thus, if we had just considered the triplet components separately, one would rather expect the zero-energy density of states to fall more rapidly for a field along the x-direction

than the y-direction. This demonstrates that we need to consider the interplay between the two components, and not just the separate components.

Exchange field along the z-direction

Thus far, we have seen that the effect of including a SO-field for an exchange field in the x- and y-direction, simply is to reduce the peak in the density of states. To conclude this section, we now discuss the case in which the exchange field lies along the z-direction, i.e. $\mathbf{h}' = \mathrm{h}'\mathbf{e}_z$. Then the SRTC′ and LRTC′ are defined by eq.203, whose relative proportions are determined by the equations

$$\frac{i}{2}D\partial_y^2 \mathrm{d}'_y = -2iD\alpha'\partial_y \mathrm{d}'_{||} - 2iD\alpha'\partial_y \mathrm{d}'_\perp + [\epsilon + 4iD\alpha'^2]\mathrm{d}'_y, \tag{212}$$

$$\frac{i}{2}D\partial_y^2 \mathrm{d}'_{||} = +2iD\alpha'\partial_y \mathrm{d}'_y + 2iD\alpha'^2 \mathrm{d}'_\perp + [\epsilon + 2iD\alpha'^2]\mathrm{d}'_{||} + h'\mathrm{f}'_s, \tag{213}$$

$$\frac{i}{2}D\partial_y^2 \mathrm{d}'_\perp = 2iD\alpha'\partial_y \mathrm{d}'_y + 2iD\alpha'^2 \mathrm{d}'_{||} + [\epsilon + 2iD\alpha'^2]\mathrm{d}'_\perp, \tag{214}$$

$$\frac{i}{2}D\partial_y^2 \mathrm{f}'_s = \epsilon \mathrm{f}'_s + h'\mathrm{d}'_{||}. \tag{215}$$

Let us first consider the case $\phi_1 = \phi_1 = \pi$, in which the only component present initially is the SRTC′ $\mathrm{d}'_{||}$. As in the previous cases, when including SO-coupling we see from the linearized equations above that the component $\mathrm{d}'_{||}$ is rotated both into a symmetric $\mathrm{d}'_\perp$ and a antisymmetric d'_y. For a length of $L' = 5$ nm, where we can neglect the rotation to singlet states, this will result in a decrease of the peak, similar to what we saw in the x- and y-case. In figure 25a we clearly see this behavior. However, for a length of $L' = 15$ nm, a reduction in the $\mathrm{d}'_{||}$ component also means fewer Cooper-pairs available to rotate to singlet states, thereby expecting the minigap to be reduced. Looking at figure 25b we clearly see such behavior. We expect this to hold for other phase differences as well. Remember, without SO-coupling, we saw in figure 22 that the density of states went from a peak to a minigap when increasing the length. The only component which can be rotated to a singlet state is the SRTC′ $\mathrm{d}'_{||}$, thus we know that we start with dominant $\mathrm{d}'_{||}$ regardless of how we choose ϕ_1 and ϕ_2. Therefore, we expect qualitatively similar behavior for other phase differences as well. We have found that this indeed holds (plots not included). There is one special case we have to be careful with though, namely, when having $\phi_1 = \phi_1 = 0$. We might question if including SO-coupling can amplify the marginal peak we saw when not having SO-coupling. However, we do not find this to be the case. Thus, even for a field in the z-direction, including SO-coupling results in a suppression of the characteristic behavior we saw without SO-coupling.
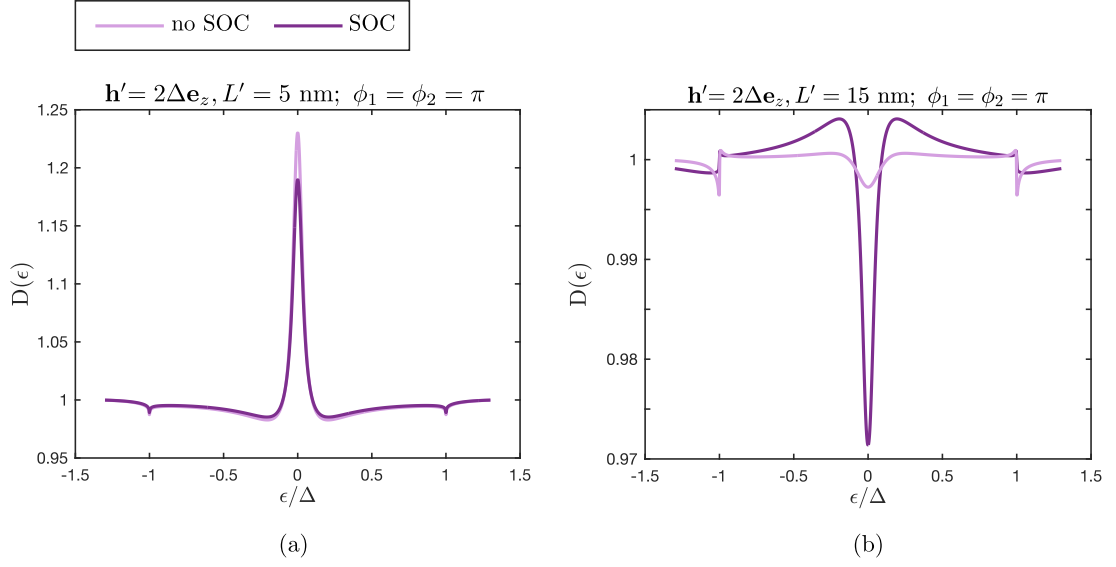
Figure 25: A comparison between the density of states $D(\epsilon)$ evaluated in the middle of a ferromagnetic nanowire with an exchange field $\mathbf{h}' = 2\Delta\mathbf{e}_z$, without and with SO-coupling (SOC). In (a) the nanowire has a length $L' = 5$ nm, while in (b) we have chosen a length of $L' = 15$ nm. Phase differences are set to $\phi_1 = \phi_2 = \pi$.

In the above, we only considered the limiting cases for an exchange field entirely along the x-, y- and z-direction. One might question if the density of states behaves differently if we rotate the field in the different planes. Remember, if we rotate the field we also redefine the SRTC' and LRTC', which now while having SO-coupling present may cause the density of states to behave differently. We also saw the linearized equations for the xz-plane become qualitatively different than what we found for the two other planes. Even so, in all cases, the density of states simply changed continuously between the two limiting cases. Therefore, we have chosen not to include these results in the thesis, as they do not lead to any qualitatively new behavior.

9

SUMMARY AND OUTLOOK

In this thesis, we have explored the proximity effect in an effective odd-frequency triplet Josephson junction. The effective Josephson junction is constructed by connecting two one-dimensional S/F/S-Josephson junctions with SO-coupling by a perpendicular nanowire. We have considered the cases where the nanowire is a normal metal and a ferromagnet with and without SO-coupling. In particular, we have focused on how the giant triplet effect seen in the two parallel one-dimensional S/F/S-Josephson junctions with SO-coupling manifests in the central nanowire. Our results showed that the effective Josephson junction behaves qualitatively different from the one-dimensional Josephson junction. The effective Josephson junction is now governed by the relationships between the initial symmetries at the midpoints of the parallel junctions. Notably, we saw that the component defined as the long-ranged triplet component in the two parallel Josephson junctions, dominates in the central nanowire even for other phase differences than the special case of $\phi_1 = \phi_2 = \pi$. Remarkably, when the nanowire was a normal metal, we also saw that the zero-energy density of states could persist throughout the normal metal for several superconducting coherence lengths. Notably, this also holds when including an exchange field along both the x- and y-direction, regardless of how we choose the phase differences. In particular, it is interesting to notice what this result entails for $\phi_1 = \phi_2 = \pi/2$, where the (charge) current is maximized in the two parallel systems. By simply connecting two parallel S/F/S-Josephson junctions, we can allow for much larger lengths in the central nanowire while still having the maximized current of the same magnitude. For an exchange field in the z-direction though, the interplay between the short-ranged triplet component and the singlet component manifests in the density of states as a transition from a peak to what resembles a minigap. Finally, we also discussed the effect of including SO-coupling in the system. Regardless of the orientation of the exchange field, including SO-coupling simply suppresses the characteristic behavior we saw without SO-coupling. However, including SO-coupling the zero-energy density of states now decays significantly faster when the field points along the y-direction than the x-direction, due to the orientation of the total triplet component in the two cases.

In conclusion, we have shown that simply by connecting two parallel S/F/S-Josephson junctions, thereby effectively creating an odd-frequency triplet Josephson junction, the system behaves qualitatively different from the one-dimensional Josephson junction. Furthermore, the zero-energy density of states now persists throughout the nanowire for several superconducting coherence lengths. Remarkably, the distinct feature between the proportions of the components seen at $\phi_{1/2} = \pi$ in the two parallel junctions now also holds for other phase differences as well.

The results presented in this thesis were obtained by assuming that the central nanowire affects the two parallel S/F/S-Josephson junctions minimally. Thus, we solved the two parallel S/F/S-Josephson junctions independently of the central nanowire, only taking into account the effect the two parallel S/F/S-Josephson junctions have on the central nanowire. Therefore, we used the standard Kupriyanov–Lukichev boundary conditions in the central nanowire as well, with the Green's functions in the center of the two parallel S/F/S-Josephson junctions as input for the boundary conditions. This assumption is assumed to be valid as long as the exchange field in the central nanowire is not too strong. However, it could be interesting to

generalize the method to take into account the effect the central nanowire has on the two parallel S/F/S-Josephson junctions, thus solving the system self-consistently at these interfaces. Solving the system self-consistently, we can also allow for stronger fields in the central nanowire than explored in this thesis.

To obtain a self-consistent solution, some issues need to be addressed, which we will now briefly discuss. The first obstacle originates from the mathematical description of the system, namely the boundary conditions. The standard Kupriyanov–Lukichev boundary conditions presented in this thesis are one-dimensional, and based on Andreev-reflection and continuity of the Green's functions at the interface. If we want to account for a third material, though, the Andreev-reflection taking place at the interface now becomes more complicated. To account for the interplay between three materials we could use the three-terminal boundary conditions derived by Titov [74], also explored by Karminskaya *et*. *al*. [75]. The boundary conditions derived by Titov hold for a three-terminal heterostructure,i.e. structures where we have three outer contact points, yet we can still use their mathematical form to describe how the three materials affect each other at such interfaces. In figure 26 we have sketched a general three-terminal junction. Here, we have a horizontal wire lying along the x-direction, represented by the blue wire, connected to a perpendicular wire at x_0, represented by the green wire. The Green's function in the blue wire is denoted $\hat{g}$, while $\hat{g}_c$ denotes the Green's function in the green wire. The tunnel barrier that separates the horizontal and perpendicular wires is represented by the gray region in figure 26. This barrier has a normal vector pointing along the y-direction, and a transparency described by the coefficient $\alpha = T_B/l_B$, where T_B is the barrier transmission probability per channel and l_B is the effective length of the barrier. The effective length of the barrier l_B is of the order of the mean free path in the horizontal material that lies along the x-direction.
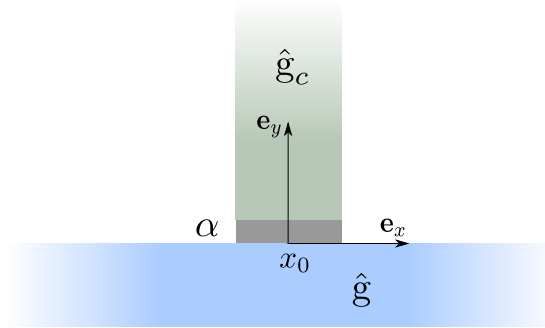
Figure 26: A sketch of a three-terminal junction. A wire along the x-direction (blue) is connected to a wire along the y-direction (green) at x_0. The Green's function in the blue wire is denoted $\hat{g}$, while $\hat{g}_c$ denotes the Green's function in the green wire. The barrier between the two wires is shown as a gray region, and the coefficient α describes the transparency of the barrier.

The fundamental idea behind the boundary conditions developed by Titov is current conservation at the three-terminal junction. Mathematically, this is accounted for by having a discontinuity in the derivative of the Green's function along the tunnel barrier. For the heterostructure sketched in figure 26 the discontinuity would be along the y-direction. Additionally, having a tunnel barrier placed *between* the two wires as shown in figure 26, the Green's function

itself also has to be continuous along the x-direction. Hence, the boundary conditions for the retarded Green's function describing such a three-terminal heterostructure reads[74]

$$\delta[\hat{I}]_{x_0} = (\hat{g}\tilde{\partial}_k\hat{g})_+ - (\hat{g}\tilde{\partial}_k\hat{g})_- = \frac{\alpha}{2}[\hat{g}_c, \hat{g}_-]_-, \tag{216}$$

$$\delta[\hat{g}]_{x_0} = \hat{g}_+ - \hat{g}_- = 0. \tag{217}$$

Here

$$\delta[f(x)]_{x_0} = \lim_{\delta\to 0}[f(x_0 + \delta) - f(x_0 - \delta)] = f_+ - f_-$$

refers to the change of the function f on an infinitesimal value δ in the x-direction. We denote the value of the function f at position $x_0 + \delta$ as $f(x_0 + \delta) = f_+$, while $f(x_0 - \delta) = f_-$ denotes the value of the function f at position $x_0 - \delta$.

Having found some new boundary conditions accounting for all three materials at the three-terminal junctions we have in our system, it remains to discuss a numerical method for solving this system self-consistently. This method must preserve both the discontinuity of the derivative in eq.216, and the continuity of the Green's function itself in eq.217, at the three-terminal junctions. Furthermore, the bvp6c-solver in matlab requires two and only two boundary conditions in each region. One way could simply be to split the ferromagnet in the parallel S/F/S-Josephson junction into two, thus solving an S/F/F/S-F-S/F/F/S system instead of an S/F/S-F-S/F/S, as sketched in figure 27. To preserve both the continuity of the Green's function and the discontinuity of the derivative at the three-terminal junction in c and d, the following procedure may be executed. For a given energy, we first solve in F_{21} and F_{22} with the standard Kupriyanov–Lukichev boundary condition at e and f respectively, and eq.216 as the boundary condition at c and d. Then we solve in F_{11} and F_{12}, still with Kupriyanov–Lukichev boundary condition at interface a and b, yet at c and d we now use eq.217 as the boundary condition. Finally, we solve for the central ferromagnet F, now with eq.216 as the boundary condition at both c and d. To acquire a self-consistent solution, we repeat the described procedure with the previous solution as the initial guess, until the maximum difference between the previous solution and the new calculated solution is below a chosen tolerance. When the solution meets the tolerance, we move on to the next energy. By doing so, we ensure that the solutions we find in the different regions all take into account the effect of each other. Hence, the described procedure solves the system self-consistently in the three-terminal junctions, thus also accounting for the effect the central nanowire has on the two parallel Josephson junctions. We do stress that in the described procedure we have not solved the system self-consistently with respect to the superconductors, i.e. we still assume the superconductor to have a bulk solution and do not take into account the effect the ferromagnet has on the superconductor. Yet, as we are interested in what happens in the central nanowire, the effects of solving the system also self-consistently at the interfaces with the superconductors are expected to be negligible.
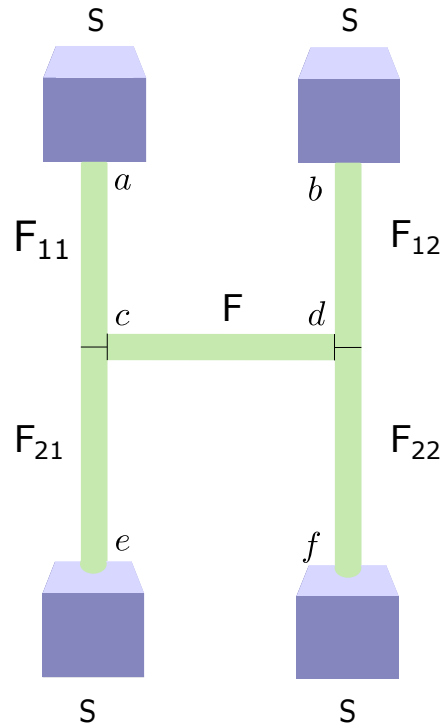
Figure 27: A sketch of the experimental set-up discussed in the suggested numerical procedure. The ferromagnets in two parallel S/F/S-Josephson junctions are divided in two, resulting in an S/F/F/S-Josephson junction. As previously these two parallel S/F/F/S-Josephson junctions are connected with a nanowire.

In the above, we have presented a suggested way to solve the system self-consistently. We have discussed a promising candidate for appropriate boundary conditions, as well as a suggested numerical procedure. For future work, we believe it would fruitful to solve the system also self-consistently, due to the exotic new phenomena multiterminal structures exhibit[63, 76, 77].

BIBLIOGRAPHY

[1] S.H. Jacobsen and J. Linder. Giant triplet proximity effect in π-biased Josephson junctions with spin-orbit coupling. *Physical Review B*, 92(2):024501, 2015.

[2] H. Kamerlingh Onnes. The superconductivity of mercury. *Comm. Phys. Lab. Univ. Leiden*, 122:122–124, 1911.

[3] H. Kamerlingh Onnes. The resistance of pure mercury at helium temperatures. *Commun. Phys. Lab. Univ. Leiden, b*, 120, 1911.

[4] W. Meissner and R. Ochsenfeld. Ein neuer effekt bei eintritt der supraleitfähigkeit. *Naturwissenschaften*, 21(44):787–788, 1933.

[5] J.A. Flores-Livas, L. Boeri, A. Sanna, G. Profeta, R. Arita, and M. Eremets. A perspective on conventional high-temperature superconductors at high pressure: Methods and materials. *Physics Reports*, 856:1–78, 2020.

[6] K.R. Chu. Room-temperature transitional transport in LaH_{10}. *Chemical Physics Letters*, 748: 137387, 2020.

[7] A.P. Drozdov, M.I. Eremets, I.A. Troyan, V. Ksenofontov, and S.I. Shylin. Conventional superconductivity at 203 kelvin at high pressures in the sulfur hydride system. *Nature*, 525 (7567):73–76, 2015.

[8] J. Bardeen, L.N. Cooper, and J.R. Schrieffer. Theory of superconductivity. *Phys. Rev.*, 108: 1175–1204, Dec 1957.

[9] F. London and H. London. The electromagnetic equations of the supraconductor. *Proceedings of the Royal Society of London. Series A-Mathematical and Physical Sciences*, 149(866):71–88, 1935.

[10] K. Fossheim and A. Sudbø. *Superconductivity: physics and applications*. John Wiley & Sons, 2004.

[11] M. Tinkham. *Introduction to superconductivity*. Dover Publications, New York, 2004.

[12] V.L. Ginzburg and L.D. Landau. On the theory of superconductivity. In *On Superconductivity and Superfluidity*, pages 113–137. Springer, 2009.

[13] A. Hirohata, K. Yamada, Y. Nakatani, L. Prejbeanu, B. Diény, P. Pirro, and B. Hillebrands. Review on spintronics: Principles and device applications. *Journal of Magnetism and Magnetic Materials*, 509:166711, 2020.

[14] G. Burkard, T.D. Ladd, J.M. Nichol, A. Pan, and J.R. Petta. Semiconductor spin qubits. *arXiv preprint arXiv:2112.08863*, 2021.

[15] D.C. Ralph and M.D. Stiles. Spin transfer torques. *Journal of Magnetism and Magnetic Materials*, 320(7):1190–1216, 2008.

[16] Y. Kajiwara, K. Harii, S. Takahashi, J. Ohe, K. Uchida, M. Mizuguchi, H. Umezawa, H. Kawai, K. Ando, K. Takanashi, et al. Transmission of electrical signals by spin-wave interconversion in a magnetic insulator. *Nature*, 464(7286):262–266, 2010.

[17] M.Z. Hasan and C.L. Kane. Colloquium: topological insulators. *Reviews of modern physics*, 82(4):3045, 2010.

[18] J. Linder and J.W.A. Robinson. Superconducting spintronics. *Nature Physics*, 11(4):307–315, 2015.

[19] M. Eschrig. Spin-polarized supercurrents for spintronics. *Phys. Today*, 64(1):43, 2011.

[20] A.I. Buzdin. Proximity effects in superconductor-ferromagnet heterostructures. *Reviews of modern physics*, 77(3):935, 2005.

[21] A.F. Volkov, F.S. Bergeret, and K.B. Efetov. Odd triplet superconductivity in superconductor-ferromagnet multilayered structures. *Physical review letters*, 90(11):117006, 2003.

[22] K. Halterman, P.H. Barsic, and O.T. Valls. Odd triplet pairing in clean superconductor/ferromagnet heterostructures. *Physical review letters*, 99(12):127002, 2007.

[23] T.S. Khaire, M.A. Khasawneh, W.P. Pratt Jr, and N.O. Birge. Observation of spin-triplet superconductivity in Co-based Josephson junctions. *Physical review letters*, 104(13):137002, 2010.

[24] F.S. Bergeret, A.F. Volkov, and K.B. Efetov. Long-range proximity effects in superconductor-ferromagnet structures. *Physical review letters*, 86(18):4096, 2001.

[25] A.F. Volkov and K.B. Efetov. Proximity effect and its enhancement by ferromagnetism in high-temperature superconductor-ferromagnet structures. *Physical review letters*, 102(7): 077002, 2009.

[26] M. Eschrig and T. Löfwander. Triplet supercurrents in clean and disordered half-metallic ferromagnets. *Nature Physics*, 4(2):138–143, 2008.

[27] M. Alidoust, J. Linder, G. Rashedi, T. Yokoyama, and A. Sudbø. Spin-polarized Josephson current in superconductor/ferromagnet/superconductor junctions with inhomogeneous magnetization. *Physical Review B*, 81(1):014512, 2010.

[28] F.S. Bergeret and I.V. Tokatly. Spin-orbit coupling as a source of long-range triplet proximity effect in superconductor-ferromagnet hybrid structures. *Physical Review B*, 89(13):134517, 2014.

[29] S.H. Jacobsen, J.A. Ouassou, and J. Linder. Critical temperature and tunneling spectroscopy of superconductor-ferromagnet hybrids with intrinsic Rashba-Dresselhaus spin-orbit coupling. *Physical Review B*, 92(2):024510, 2015.

[30] S.H. Jacobsen, I. Kulagina, and J. Linder. Controlling superconducting spin flow with spin-flip immunity using a single homogeneous ferromagnet. *Scientific reports*, 6(1):1–9, 2016.

[31] J. Arjoranta and T.T. Heikkilä. Intrinsic spin-orbit interaction in diffusive normal wire Josephson weak links: supercurrent and density of states. *Physical Review B*, 93(2):024522, 2016.

[32] S.H. Jacobsen and J. Linder. Quantum kinetic equations and anomalous nonequilibrium Cooper-pair spin accumulation in Rashba wires with Zeeman splitting. *Physical Review B*, 96(13):134513, 2017.

[33] K.V. Samokhin. Spin–orbit coupling and semiclassical electron dynamics in noncentrosymmetric metals. *Annals of Physics*, 324(11):2385–2407, 2009.

[34] J.A. Ouassou. *Manipulating superconductivity in magnetic nanostructures in and out of equilibrium*. PhD thesis, Norwegian University of Science and Technology, 2019.

[35] F.S. Bergeret and I.V. Tokatly. Singlet-triplet conversion and the long-range proximity effect in superconductor-ferromagnet structures with generic spin dependent fields. *Physical review letters*, 110(11):117003, 2013.

[36] Y.A. Bychkov and E.I. Rashba. Oscillatory effects and the magnetic susceptibility of carriers in inversion layers. *Journal of physics C: Solid state physics*, 17(33):6039, 1984.

[37] S.D. Ganichev and L.E. Golub. Interplay of Rashba/Dresselhaus spin splittings probed by photogalvanic spectroscopy–A review. *physica status solidi (b)*, 251(9):1801–1823, 2014.

[38] A. Manchon, H.C. Koo, J. Nitta, S.M. Frolov, and R.A. Duine. New perspectives for Rashba spin–orbit coupling. *Nature materials*, 14(9):871–882, 2015.

[39] G. Dresselhaus. Spin-orbit coupling effects in zinc blende structures. *Physical Review*, 100 (2):580, 1955.

[40] J.D. Koralek, C.P. Weber, J. Orenstein, B.A. Bernevig, S.C. Zhang, S. Mack, and D.D. Awschalom. Emergence of the persistent spin helix in semiconductor quantum wells. *Nature*, 458(7238):610–613, 2009.

[41] J. Fu and J.C Egues. Spin-orbit interaction in GaAs wells: From one to two subbands. *Physical Review B*, 91(7):075408, 2015.

[42] W. Desrat, D.K. Maude, Z.R. Wasilewski, R. Airey, and G. Hill. Dresselhaus spin-orbit coupling in a symmetric (100) GaAs quantum well. *Physical Review B*, 74(19):193317, 2006.

[43] A. Bringer, S. Heedt, and T. Schäpers. Dresselhaus spin-orbit coupling in [111]-oriented semiconductor nanowires. *Physical Review B*, 99(8):085437, 2019.

[44] A.F. Andreev. The thermal conductivity of the intermediate state in superconductors. *Soviet Physics-JETP*, 19(5):1228–1231, 1964.

[45] I. Kulagina. *Magnetization Dynamics and Spinsupercurrents in Superconductingand Multiferroic Systems*. PhD thesis, Norwegian University of Science and Technology, 2016.

[46] J.A. Ouassou. Density of states and critical temperature in superconductor/ferromagnet structures with spin-orbit coupling. Master's thesis, Norwegian University of Science and Technology, 2015.

[47] B.D. Josephson. Possible new effects in superconductive tunnelling. *Physics letters*, 1(7): 251–253, 1962.

[48] A.A. Golubov, M.Y. Kupriyanov, and E. Il'Ichev. The current-phase relation in Josephson junctions. *Reviews of modern physics*, 76(2):411, 2004.

[49] A.V. Samokhvalov. Current-phase relation in a Josephson junction coupled with a magnetic dot. *Physical Review B*, 80(13):134513, 2009.

[50] F.S. Bergeret and I.V. Tokatly. Theory of diffusive φ_0 Josephson junctions in the presence of spin-orbit coupling. *EPL (Europhysics Letters)*, 110(5):57005, 2015.

[51] Y. Fuseya, H. Kohno, and K. Miyake. Realization of odd-frequency p-wave spin–singlet superconductivity coexisting with antiferromagnetic order near quantum critical point. *Journal of the Physical Society of Japan*, 72(11):2914–2923, 2003.

[52] Y. Dalichaouch, M.C. De Andrade, D.A. Gajewski, R. Chau, P. Visani, and M.B. Maple. Impurity scattering and triplet superconductivity in UPt_3. *Physical review letters*, 75(21): 3938, 1995.

[53] S. Onari and H. Kontani. Violation of Anderson's theorem for the sign-reversing s-wave state of iron-pnictide superconductors. *Physical review letters*, 103(17):177001, 2009.

[54] Y. Wang, A. Kreisel, P.J. Hirschfeld, and V. Mishra. Using controlled disorder to distinguish s±and s++ gap structure in Fe-based superconductors. *Physical Review B*, 87(9):094504, 2013.

[55] A.P. Mackenzie, R.K.W. Haselwimmer, A.W. Tyler, G.G. Lonzarich, Y. Mori, S. Nishizaki, and Y. Maeno. Extremely strong dependence of superconductivity on disorder in Sr_2RuO_4. *Physical review letters*, 80(1):161, 1998.

[56] M. Eschrig. Spin-polarized supercurrents for spintronics: a review of current progress. *Reports on Progress in Physics*, 78(10):104501, 2015.

[57] T. Matsubara. A new approach to quantum-statistical mechanics. *Progress of theoretical physics*, 14(4):351–378, 1955.

[58] L.V. Keldysh. Diagram technique for nonequilibrium processes. *Sov. Phys. JETP*, 20(4): 1018–1026, 1965.

[59] V. Chandrasekhar. Proximity-coupled systems: Quasiclassical theory of superconductivity. In *Superconductivity*, pages 279–313. Springer, 2008.

[60] W. Belzig, F.K. Wilhelm, C. Bruder, G. Schön, and A.D. Zaikin. Quasiclassical Green's function approach to mesoscopic superconductivity. *Superlattices and microstructures*, 25 (5-6):1251–1288, 1999.

[61] J.P. Morten. Spin and charge transport in dirty superconductors. Master's thesis, Norwegian University of Science and Technology, 2005.

[62] J.A. Ouassou and J. Linder. Full proximity effect in spin-textured superconductor | ferromagnet bilayers. *Norwegian University of Science and Technology*, 2015.

[63] M. Amundsen. *Proximity effects in superconducting hybrid structures with spin-dependent interactions*. PhD thesis, Norwegian University of Science and Technology, 2020.

[64] M.Y. Kuprianov and V.F. Lukichev. Influence of boundary transparency on the critical current of dirty SS'S structures. *Zh. Eksp. Teor. Fiz*, 94:149, 1988.

[65] N. Schopohl. Transformation of the Eilenberger equations of superconductivity to a scalar Riccati equation. *arXiv preprint cond-mat/9804064*, 1998.

[66] A.P. Mackenzie and Y. Maeno. The superconductivity of Sr_2RuO_4 and the physics of spin-triplet pairing. *Reviews of Modern Physics*, 75(2):657, 2003.

[67] R. Fazio and C. Lucheroni. Local density of states in superconductor-ferromagnetic hybrid systems. *EPL (Europhysics Letters)*, 45(6):707, 1999.

[68] Y.V. Nazarov. Novel circuit theory of Andreev reflection. *Superlattices and microstructures*, 25(5-6):1221–1231, 1999.

[69] N. Hale and D.R. Moore. A sixth-order extension to the MATLAB package bvp4c of J.Kierzenka and L.Shampine, 2008. Technical Report (Oxford University Computing Laboratory).

[70] J. Bass and W.P. Pratt. Spin-diffusion lengths in metals and alloys, and spin-flipping at metal/metal interfaces: an experimentalist's critical review. *Journal of Physics: Condensed Matter*, 19(18):183201, 2007.

[71] R.S. Keizer, S.T.B Gönnenwein, T.M. Klapwijk, G. Miao, G. Xiao, and A. Gupta. A spin triplet supercurrent through the half-metallic ferromagnet CrO_2. *Nature*, 439(7078):825–827, 2006.

[72] M.S. Anwar, F. Czeschka, M. Hesselberth, M. Porcu, and J. Aarts. Long-range supercurrents through half-metallic ferromagnetic CrO_2. *Physical review B*, 82(10):100501, 2010.

[73] I. Sosnin, H. Cho, V.T. Petrashov, and A.F. Volkov. Superconducting phase coherent electron transport in proximity conical ferromagnets. *Physical review letters*, 96(15):157002, 2006.

[74] M. Titov. Thermopower oscillations in mesoscopic Andreev interferometers. *Physical Review B*, 78(22):224521, 2008.

[75] T.Y. Karminskaya, M.Y. Kupriyanov, S.L. Prischepa, and A.A. Golubov. Conductance spectroscopy in ferromagnet–superconductor hybrids. *Superconductor science and technology*, 27(7):075008, 2014.

[76] E. Strambini, S. D'Ambrosio, F. Vischi, F.S. Bergeret, Y.V. Nazarov, and F. Giazotto. The ω-SQUIPT as a tool to phase-engineer Josephson topological materials. *Nature Nanotechnology*, 11(12):1055–1059, 2016.

[77] M. Alidoust, G. Sewell, and J. Linder. Superconducting phase transistor in diffusive four-terminal ferromagnetic Josephson junctions. *Physical Review B*, 85(14):144520, 2012.

A

LINEARIZED KUPRIYANOV–LUKICHEV BOUNDARY CONDITIONS WITH D-VECTOR FORMALISM

Close to the critical temperature and while having $\Delta << \epsilon$, we can also linearize the Kupriyanov–Lukichev boundary conditions. Using the general definition of weak proximity effect as stated in eq. 167 the boundary conditions at the material-interface in eq.125 and eq.126, simply reduces to:

$$\partial_k \underline{\gamma}_1 = \Omega_1(\underline{\gamma}_2 - \underline{\gamma}_1) + i\underline{\gamma}_1 \underline{\mathcal{A}}_k^* + i\underline{\mathcal{A}}_k \underline{\gamma}_1 \tag{218}$$

$$\partial_k \underline{\gamma}_2 = \Omega_2(\underline{\gamma}_2 - \underline{\gamma}_1) + i\underline{\gamma}_2 \underline{\mathcal{A}}_k^* + i\underline{\mathcal{A}}_k \underline{\gamma}_2 \tag{219}$$

If we now insert the d-vector formalism, the first equation transforms to:

$$\partial_z d_{x,1} = \Omega_1(d_{x,2} - d_{x,1}) + 2\alpha d_{z,1} \tag{220}$$

$$\partial_z d_{y,1} = \Omega_1(d_{y,2} - d_{y,1}) + 2\alpha d_{z,1} \tag{221}$$

$$\partial_z d_{z,1} = \Omega_1(d_{z,2} - d_{z,1}) - 2\alpha(d_{x,1} + d_{y,1}) \tag{222}$$

$$\partial_z f_{s,1} = \Omega_1(f_{s,2} - f_{s,1}) \tag{223}$$

While the second equation transforms to:

$$\partial_z d_{x,2} = \Omega_2(d_{x,2} - d_{x,1}) + 2\alpha d_{z,2} \tag{224}$$

$$\partial_z d_{y,2} = \Omega_2(d_{y,2} - d_{y,1}) + 2\alpha d_{y,2} \tag{225}$$

$$\partial_z d_{z,2} = \Omega_2(d_{z,2} - d_{z,1}) - 2\alpha(d_{y,2} + d_{x,2}) \tag{226}$$

$$\partial_z f_{s,2} = \Omega_2(f_{s,2} - f_{s,1}) \tag{227}$$

B

SOLUTION OF THE SINGLET AND SHORT-RANGED TRIPLET COMPONENT FOR FERROMAGNET IN THE WEAK PROXIMITY LIMIT

Having a ferromagnet without SO-coupling and a exchange field $\mathbf{h} = h\mathbf{e}_z$ along the z-direction, the linearized Usadel equations reduces to

$$\frac{i}{2}D\partial_z^2 \mathbf{d}_{||} = \epsilon \mathbf{d}_{||} + h\mathbf{f}_s, \tag{228}$$

$$\frac{i}{2}D\partial_z^2 \mathbf{f}_s = \epsilon \mathbf{f}_s + h\mathbf{d}_{||}. \tag{229}$$

Looking at the above equations we notice that we can combine them by doing the following

$$\frac{i}{2}D\partial_z^2(\mathbf{d}_{||} \pm \mathbf{f}_s) = \epsilon(\mathbf{d}_{||} \pm \mathbf{f}_s) + h(\mathbf{d}_{||} \pm \mathbf{f}_s)$$
$$= \epsilon(\mathbf{d}_{||} \pm \mathbf{f}_s) \pm h(\mathbf{d}_{||} \pm \mathbf{f}_s) \tag{230}$$

Defining $\mathbf{f}_\pm \equiv \mathbf{d}_{||} \pm \mathbf{f}_s$ and $\epsilon_\pm \equiv \epsilon \pm h$, the above equation reads

$$D\partial_z^2 \mathbf{f}_\pm + 2i\epsilon_\pm \mathbf{f}_\pm = 0. \tag{231}$$

Assuming we are close to the critical temperature and as well as having $\Delta << \epsilon$, we can also use linearized the Kupriyanov–Lukichev boundary conditions. For $z = 0$ these boundary conditions reads

$$\xi L \partial_z \mathbf{f}_s = \mathbf{f}_s - \mathbf{f}_{\text{BCS}} e^{i\phi_L}, \tag{232}$$

$$\xi L \partial_z \mathbf{d}_{||} = \mathbf{d}_{||}. \tag{233}$$

While for $z = L$ the boundary conditions becomes

$$\xi L \partial_z \mathbf{f}_s = \mathbf{f}_{\text{BCS}} e^{i\phi_R} - \mathbf{f}_s, \tag{234}$$

$$\xi L \partial_z \mathbf{d}_{||} = -\mathbf{d}_{||}. \tag{235}$$

where $\mathbf{f}_{\text{BCS}}$ is the magnitude of the BCS-bulk solution:Furthermore, ϕ_L and ϕ_R denotes the phase of the left and right superconductor respectively.

Again, using the definition of $\mathbf{f}_\pm = \mathbf{d}_{||} \pm \mathbf{f}_s$, as well as assuming $\mathbf{f}_\pm \ll \mathbf{f}_{\text{BCS}}$, the boundary conditions reduces to

$$\xi L \partial_z \mathbf{f}_\pm \big|_{z=0} = \mp \mathbf{f}_{\text{BCS}} e^{i\phi_L}, \tag{236}$$

$$\xi L \partial_z \mathbf{f}_\pm \big|_{z=L} = \pm \mathbf{f}_{\text{BCS}} e^{i\phi_R}. \tag{237}$$

Looking at eq.231 we can write a general solution to this equation as

$$f_{\pm} = Ae^{\sqrt{2i\epsilon_{\pm}/D}zi} + Be^{-\sqrt{2i\epsilon_{\pm}/D}zi}$$

$$= Ae^{k_{\pm}zi} + Be^{-k_{\pm}zi} \tag{238}$$

Inserting the above form of $f_{\pm}$ into the boundary conditions in eq.236 and 237 yields

$$A - B = \frac{\mp f_{\text{BCS}}}{i\xi Lk_{\pm}} e^{i\phi_L}, \tag{239}$$

$$Ae^{k_{\pm}Li} + Be^{-k_{\pm}Li} = \frac{\mp f_{\text{BCS}}}{i\xi Lk_{\pm}} (-e^{i\phi_R}) \tag{240}$$

To isolate the coefficient A we multiply eq.239 with $e^{-k_{\pm}Li}$ and subtract the resulting equation from eq.240. Similarly, to isolate the coefficient B we multiply eq.239 with $e^{k_{\pm}Li}$ and subtract the resulting equation from eq.240. Doing so, we obtain the following expressions for the coefficient A and B

$$A = \frac{\pm f_{\text{BCS}}}{i\xi Lk_{\pm}2i\sin(k_{\pm}L)} \left(e^{i\phi_R} + e^{i\phi_L}e^{-k_{\pm}Li}\right), \tag{241}$$

$$B = \frac{\pm f_{\text{BCS}}}{i\xi Lk_{\pm}2i\sin(k_{\pm}L)} \left(e^{i\phi_R} + e^{i\phi_L}e^{k_{\pm}Li}\right). \tag{242}$$

Having determined the coefficients A and B we have now found the solution of $f_{\pm}$ in our system. In particular, choosing $z = L/2$, the solution in the middle of the ferromagnet simplifies to

$$f_{\pm} = \frac{\pm f_{\text{BCS}}}{-\xi Lk_{\pm}\sin(k_{\pm}L)} \cos(k_{\pm}L/2)\left(e^{i\phi_R} + e^{i\phi_L}\right). \tag{243}$$

MATLAB-CODE FOR SOLVING A ONE-DIMENSIONAL TRILAYERD HETEROSTRUCTURE

```matlab
%main-file for solving a superconductor/material/superconductor structure along
    the z-direction.

clear global

%Thouless energy
global Eth

global epsilon
global NumbersE
global ii

%interface parameters for the left and right interfaces  (=Rn/RB)
global ratioL
global ratioR

%lengths
global L_vec
global L

%magnitudes and phases for the superconductors
global Delta_L
global phi_L

global Delta_R
global phi_R

%SO-strength
global Alpha

%SO- and exchange field
global Ax
global Ay
global Az
global hx
global hy
global hz

%define global matrices
global sigmax
```

```matlab
40   global sigmay
41   global sigmaz
42
43   % bulk solution in superconductor to the left
44   global g1sL
45   global g2sL
46   global g3sL
47   global g4sL
48   global gt1sL
49   global gt2sL
50   global gt3sL
51   global gt4sL
52
53   % bulk solution in superconductor to the right
54   global g1sR
55   global g2sR
56   global g3sR
57   global g4sR
58   global gt1sR
59   global gt2sR
60   global gt3sR
61   global gt4sR
62
63   %matrix-elements of: gamma (g), partial derivative of gamma (dg), gamma tilde (gt)
         and partial derivative of gamma tilde (dgt)
64   global g1
65   global g2
66   global g3
67   global g4
68   global dg1
69   global dg2
70   global dg3
71   global dg4
72   global gt1
73   global gt2
74   global gt3
75   global gt4
76   global dgt1
77   global dgt2
78   global dgt3
79   global dgt4
80
81   %elements of initial guess
82   global g1_init
83   global g2_init
84   global g3_init
85   global g4_init
```

```matlab
86   global dg1_init
87   global dg2_init
88   global dg3_init
89   global dg4_init
90   global gt1_init
91   global gt2_init
92   global gt3_init
93   global gt4_init
94   global dgt1_init
95   global dgt2_init
96   global dgt3_init
97   global dgt4_init
98
99   %density of states and d-vector components
100  global DoS
101  global dx
102  global dy
103  global dz
104  global fs
105
106  %predefine gamma-elements (100 positions used always):
107  g1 = zeros(NumbersE, 100);
108  g2 = zeros(NumbersE, 100);
109  g3 = zeros(NumbersE, 100);
110  g4 = zeros(NumbersE, 100);
111  dg1 = zeros(NumbersE, 100);
112  dg2 = zeros(NumbersE, 100);
113  dg3 = zeros(NumbersE, 100);
114  dg4 = zeros(NumbersE, 100);
115  gt1 = zeros(NumbersE, 100);
116  gt2 = zeros(NumbersE, 100);
117  gt3 = zeros(NumbersE, 100);
118  gt4 = zeros(NumbersE, 100);
119  dgt1 = zeros(NumbersE, 100);
120  dgt2 = zeros(NumbersE, 100);
121  dgt3 = zeros(NumbersE, 100);
122  dgt4 = zeros(NumbersE, 100);
123
124  %predefine initial guesses:
125  g1_init = zeros(NumbersE, 100);
126  g2_init = zeros(NumbersE, 100);
127  g3_init = zeros(NumbersE, 100);
128  g4_init = zeros(NumbersE, 100);
129  dg1_init = zeros(NumbersE, 100);
130  dg2_init = zeros(NumbersE, 100);
131  dg3_init = zeros(NumbersE, 100);
132  dg4_init = zeros(NumbersE, 100);
```

```matlab
133  gt1_init = zeros(NumbersE, 100);
134  gt2_init = zeros(NumbersE, 100);
135  gt3_init = zeros(NumbersE, 100);
136  gt4_init = zeros(NumbersE, 100);
137  dgt1_init = zeros(NumbersE, 100);
138  dgt2_init = zeros(NumbersE, 100);
139  dgt3_init = zeros(NumbersE, 100);
140  dgt4_init = zeros(NumbersE, 100);
141
142  %predefine DoS and d-vector components
143  DoS = zeros(NumbersE, 100);
144  dx = zeros(NumbersE, 100);
145  dy = zeros(NumbersE, 100);
146  dz = zeros(NumbersE, 100);
147  fs = zeros(NumbersE, 100);
148
149  %system parameters
150  ratioL = 1/3;
151  ratioR = ratioL;
152
153  Delta_L = 1;
154  Delta_R = 1;
155
156  phi_L = 0;
157  phi_R_vec = [-0.25*pi];
158
159  Alpha = 0.4;
160  xi = 30;
161
162  hx = 0;
163  hy = 10*Delta_L;
164  hz = 0;
165
166  %define length, position and energy vectors
167  L_vec = [15];
168  position = linspace(0,1,100);
169  DoS_as_func_of_lenght = [];
170
171  NumbersE = 300;
172  inelastic = 1*1e-03;
173  Emin = 2*inelastic;
174  Emax = 1.3*Delta_L;
175
176  %a small imaginary part is added to the energy for numerical stability
177  e1 = linspace(Emin, Emin + 0.25, 125) + inelastic*1i;
178  e2 = linspace(Emin + 0.2505, 0.9, 50) + inelastic*1i;
179  e3 = linspace(0.905, Emax, 125) + inelastic*1i;
```

```matlab
epsilon_vec = [e1, e2, e3];

%define matrices
sigmax = [0, 1; 1, 0];
sigmay = [0, -1i; 1i, 0];
sigmaz = [1, 0; 0, -1];


for m = 1:length(L_vec)
    L = L_vec(m);
    display(L)
    Eth = (xi/L)^2;
    Ax = 0;
    Ay = 0;
    Az = Alpha*sigmax/L  - Alpha*sigmay/L;

    if Az == 0
        Az_hat = 0;
    else
        Az_hat = blkdiag(Az,-conj(Az));
    end

    for n = 1:length(phi_R_vec)
        phi_R = phi_R_vec(n);
        display(phi_R)
        %start with largest energy for a more efficient code
        for i = NumbersE:-1:1
            epsilon = epsilon_vec(i);
            display(epsilon)
            ii = i;

            theta_s = atanh(1/epsilon);
            s = sinh(theta_s);
            c = cosh(theta_s);

            %solution bulk in superconductors:
            g1sL = 0;
            g2sL = s*exp(1i*phi_L)/(1+c);
            g3sL = -s*exp(1i*phi_L)/(1+c);
            g4sL = 0;
            gt1sL = 0;
            gt2sL = -s*exp(-1i*phi_L)/(1+c);
            gt3sL = s*exp(-1i*phi_L)/(1+c);
            gt4sL = 0;

            g1sR = 0;
```

```matlab
            g2sR = s*exp(1i*(phi_R))/(1+c);
            g3sR = -s*exp(1i*(phi_R))/(1+c);
            g4sR = 0;
            gt1sR = 0;
            gt2sR = -s*exp(-1i*(phi_R))/(1+c);
            gt3sR = s*exp(-1i*(phi_R))/(1+c);
            gt4sR = 0;

            %initial guess for first energy for the two parallel junctons
            %to help the matlab-solver to start near the correct solution we use
                all gammas's set to zero as in a normal metal
            if i == NumbersE && n==1
                g1_init(i, :) = 0*g1sL;
                g2_init(i, :) = 0*g2sL;
                g3_init(i, :) = 0*g3sL;
                g4_init(i, :) = 0*g4sL;
                dg1_init(i, :) = 0;
                dg2_init(i, :) = 0;
                dg3_init(i, :) = 0;
                dg4_init(i, :) = 0;
                gt1_init(i, :) = 0*gt1sL;
                gt2_init(i, :) = 0*gt2sL;
                gt3_init(i, :) = 0*gt3sL;
                gt4_init(i, :) = 0*gt4sL;
                dgt1_init(i, :) = 0;
                dgt2_init(i, :) = 0;
                dgt3_init(i, :) = 0;
                dgt4_init(i, :) = 0;
            else
                0;
            end

            %solve for gamma
            [g1(i, :), g2(i, :), g3(i, :), g4(i, :), dg1(i, :), dg2(i, :), dg3(i,
                :), dg4(i, :), gt1(i, :), gt2(i, :), gt3(i, :), gt4(i, :), dgt1(i,
                 :), dgt2(i, :), dgt3(i, :), dgt4(i, :)] =
                solve_usadel_gamma_trilayer();

            %use previous solution as initial guess for next energy in central
                nanowire guess
            if i~= 1
                g1_init(i - 1, :) = g1(i, :);
                g2_init(i - 1, :) = g2(i, :);
                g3_init(i - 1, :) = g3(i, :);
                g4_init(i - 1, :) = g4(i, :);
                dg1_init(i - 1, :) = dg1(i, :);
                dg2_init(i - 1, :) = dg2(i, :);
```

```matlab
                dg3_init(i - 1, :) = dg3(i, :);
                dg4_init(i - 1, :) = dg4(i, :);
                gt1_init(i - 1, :) = gt1(i, :);
                gt2_init(i - 1, :) = gt2(i, :);
                gt3_init(i - 1, :) = gt3(i, :);
                gt4_init(i - 1, :) = gt4(i, :);
                dgt1_init(i - 1, :) = dgt1(i, :);
                dgt2_init(i - 1, :) = dgt2(i, :);
                dgt3_init(i - 1, :) = dgt3(i, :);
                dgt4_init(i - 1, :) = dgt4(i, :);
            end

            %iterate thorough positions
            for j=1:length(position);
                %gamma matrix
                g = [g1(i,j), g2(i,j); g3(i,j), g4(i,j)];
                %derivative gamma
                dg = [dg1(i,j), dg2(i,j); dg3(i,j), dg4(i,j)];
                %gamma tilde matrix
                gt = [gt1(i,j), gt2(i,j); gt3(i,j), gt4(i,j)];
                %derivative gamma tilde
                dgt = [dgt1(i,j), dgt2(i,j); dgt3(i,j), dgt4(i,j)];

                %normalization matrices
                N = inv(eye(2) - g*gt);
                Nt = inv(eye(2) - gt*g);
                retarded = N*(eye(2) + g*gt);
                %square = retarded*retarded
                DoS(i,j) = (1/2)*real(trace(retarded));

                %decompose the compoenents
                ggf = 2*N*g; %green f= N*gamma matrix
                dx(i,j) = (ggf(2,2) - ggf(1,1))/2;
                dy(i,j) = (ggf(2,2) + ggf(1,1))/2i;
                dz(i,j) = (ggf(1,2) + ggf(2,1))/2;
                fs(i,j) = (ggf(1,2) - ggf(2,1))/2;
            end
        end

    %before moving on to the next phase, we update the initial guess for all
        energies and positions
    if n~= length(phi_R_vec)
            g1_init(:, :) = g1(:, :);
            g2_init(:, :) = g2(:, :);
            g3_init(:, :) = g3(:, :);
            g4_init(:, :) = g4(:, :);
            dg1_init(:, :) = dg1(:, :);
```

```matlab
                dg2_init(:, :) = dg2(:, :);
                dg3_init(:, :) = dg3(:, :);
                dg4_init(:, :) = dg4(:, :);
                gt1_init(:, :) = gt1(:, :);
                gt2_init(:, :) = gt2(:, :);
                gt3_init(:, :) = gt3(:, :);
                gt4_init(:, :) = gt4(:, :);
                dgt1_init(:, :) = dgt1(:, :);
                dgt2_init(:, :) = dgt2(:, :);
                dgt3_init(:, :) = dgt3(:, :);
                dgt4_init(:, :) = dgt4(:, :);

        end
        %the zero-energy denisty of states evaluated in the middle of the junction
             for a given lenght L
        DoS_as_func_of_lenght(end+1) = DoS(1,50);
    end
    save main_trilayer
end
save main_trilayer
```